Synthesis of Colloidal Zinc Chalcogenide Nanoplatelets: Structural and Optical Properties and Their Change upon Doping and Shell Formation

A thesis submitted to attain the degree of

Doctor of Natural Sciences of the University of Hamburg

(*Dr. rer. nat.*)

presented by

Liwei Dai

born on 05.07.1991 in Zhejiang, China

Hamburg 2021

Ideal is the beacon.
Without ideal, there is no secure
direction.
Without direction, there is no life.

———————————————

Lev Tolstoy

The present work was carried out in the Institute of Physical Chemistry, University of Hamburg in the groups of *Prof. Dr. Christian Klinke* (from October 2017 to July 2019) and *Prof. Dr. Alf Mews* (from August 2019 to September 2021), respectively.

Following reviewers recommend the adoption of the dissertation:
1. Reviewer: *Prof. Dr. Christian Klinke*
2. Reviewer: *Prof. Dr. Gabriel Bester*

Date of oral defense: 22-11-2021

The release for the publication of the dissertation was granted on 22-11-2021.

CONTENTS

CONTENTS

CONTENTS

CONTENTS

Acknowledgements

ACKNOWLEDGEMENTS

Hamburg, September 2021

ABSTRACT

Abstract

Heavy-metal-free ZnS nanocrystals (NCs) are "green" low-toxic materials compared to Cd-based and Pb-based NCs. They exhibit a large direct band gap of approximately 3.7−3.8 eV and a small exciton Bohr radius of 2.5 nm, which attracts numerous research interests with applications in photocatalysis, light-emitting diodes, and energy conversion. It is well-known that the physical and chemical properties of semiconductor NCs strongly depend on their shape. Thus, synthetic control over the shape of the NCs is significant. Many efforts have been made to synthesize colloidal ZnS NCs with different shapes including quantum dots (QDs), nanorods (NRs), and nanowires (NWs). However, reports on the synthesis of two-dimensional (2D) ZnS NCs are scarce. The main reason is that growing ZnS NCs laterally is challenging because ZnS has a non-layered structure. The thermodynamically preferential nanostructure of ZnS is zero-dimensional (0D). This deficiency promotes us to explore the synthesis of colloidal 2D ZnS NCs.

In the literature, it is noted that many syntheses of 2D semiconductor NCs such as CdSe, CuS, and PbS were based on amine solvents. The principle is assembly of "small magic clusters" into 2D structures with assist of lamellar soft templates. This method is suitable for layered and non-layered materials. In the first part of the thesis, the soft-template-based method was extended to prepare 2D ZnS NCs. After optimization of experimental parameters (such as the volume ratio of amine solvents, amount of precursors, temperature, and reaction time), colloidal quasi-2D ZnS nanoplatelets (NPLs) were synthesized. The resulting ZnS NPLs show a set of distinct absorption transitions at room temperature, which is rarely observed in 0D and one-dimensional (1D) ZnS NCs. It is proved that the observed features in the absorption spectrum coincide well with the genuine quasi-2D nature of ZnS NPLs deduced from *ab initio* calculations. Additionally, the shape/phase control in ZnS NCs was realized by tuning the amount of sulfur, which endows the NCs with tunable optoelectronic properties.

The as-synthesized ZnS NPLs exhibit not only evident excitonic features, but also superiority as matrix for transition-metal ions due to their flat structure and extremely uniform thickness. Introducing impurity ions into NCs can generate new properties and improve the original ones. In the second part of the thesis, Mn^{2+} ions were incorporated into the ZnS NPLs through an adapted synthesis protocol of ZnS NPLs. It was found that the shape and crystal structure of the doped NPLs remain unaltered compared to the undoped ones. Mn^{2+}-doped ZnS

ABSTRACT

(ZnS:Mn) NPLs exhibit dual emission in the UV and visible range. By changing the Mn^{2+} concentration, the intensity ratio of the dual emission can be easily tuned. The energy-transfer between the host and dopants was explored in detail, which reveals the photophysical processes in ZnS:Mn NPLs. Additionally, it is found that the surface of the NPLs is a critical and limiting factor for the effective energy conversion. The photoluminescence quantum yield (PLQY) of ZnS:Mn NPLs can be improved by passivating the surface of the NPLs with an appropriate zinc-containing solution.

Although ligand passivation can minimize the surface trap states, the synthesized ZnS:Mn NPLs still show a relatively low PLQY compared to the reported Mn^{2+}-doped dots and rods. Besides, it is discovered that many Mn^{2+} ions accumulate on the surface of NPLs due to the "self-purification" effect, resulting in reduced optical properties of ZnS:Mn NPLs (*e.g.* low PLQY, inhomogeneous PL decay, and shortened PL lifetime). To address these issues, the preparation of type-I ZnSe:Mn/ZnS core/shell NPLs was taken into account. The ZnS shell can not only passivate the surface trap states to improve the PLQY, but also ensure that Mn^{2+} ions stay away from the surface. First, ZnSe:Mn core NPLs were synthesized using the same strategy as ZnS:Mn NPLs since both materials have similar structural characteristics. Considering the low thermal stability of NPLs, a low temperature method, called colloidal atomic layer deposition (c-ALD), was used to grow ZnS shells on the ZnSe cores. The formation of the ZnS shells was evidenced by a combination of transmission electron microscopy (TEM) and atomic force microscopy (AFM) measurements. It is found that the decay lifetime of Mn^{2+} emission significantly increases from 27 μs to 200 μs and the decay behavior becomes more mono-exponential upon deposition of the ZnS shell, which indicates a homogeneous distribution of Mn^{2+} ions.

In summary, a simple and effective synthesis protocol was developed to grow non-layered materials (ZnS and ZnSe) laterally. The obtained quasi-2D NPLs exhibit shape-dependent optical properties, which differs from the 0D and 1D NCs. Subsequently, such Zn chalcogenide NPLs were doped with Mn^{2+} ions to achieve tunable dual emission. To improve the optical properties of ZnSe:Mn NPLs, ZnS shells were successfully coated on the NPLs via the c-ALD method. The above work opens a path for the synthesis and optical performance tunability of quasi-2D semiconductor NPLs.

ZUSAMMENFASSUNG

Zusammenfassung

Schwermetallfreie ZnS Nanokristalle sind im Vergleich zu Cd- und Pb-basierten Nanokristallen "grüne" Materialien mit geringer Toxizität. Sie weisen eine große direkte Bandlücke von etwa 3,7–3,8 eV und einen kleinen Exziton-Bohr-Radius von 2,5 nm auf, wodurch zahlreiche Forschungfragen mit Anwendungen in der Photokatalyse, Leuchtdioden und Energieumwandlung in Betracht kommem. Es ist bekannt, dass die physikalischen und chemischen Eigenschaften von Halbleiter-Nanokristallen stark von ihrer Form abhängen. Somit ist die synthetische Kontrolle über die Form der Nanokristalle signifikant. Es wurden viele Anstrengungen unternommen, um kolloidale ZnS-Nanokristalle mit unterschiedlichen Formen, z.B. Quantenpunkte, Nanostäbchen und Nanodrähte, zu synthetisieren. Berichte über die Synthese zweidimensionaler (2D) ZnS-Nanokristalle sind jedoch rar. Der Hauptgrund ist, dass ZnS keine geschichtete Kristallstruktur besitzt und bevorzugt nulldimensional (0D) statt zweidimensional wächst. Es stellt also eine gewisse Herausforderung dar, kolloidale zweidimensionale ZnS-Nanokristalle herzustellen.

In der Literatur sind viele Synthesen von 2D-Halbleiternanokristallen wie CdSe, CuS und PbS bekannt, die auf dem Einsatz von amin-basierten Lösungsmitteln beruhen. Das Prinzip ist der Zusammenbau von "kleinen magischen Clustern" zu 2D-Strukturen mit Hilfe lamellarer Schablonen, engl. *soft templates*. Dieses Verfahren ist für geschichtete und nicht-geschichtete Materialien geeignet. Im ersten Teil der Arbeit wurde die soft-template-basierte Methode zur Herstellung von zweidimensionalen ZnS-Nanokristallen erweitert. Nach Optimierung experimenteller Parameter (Volumenverhältnis der Amin-Lösungsmittel, Menge der Vorläufer, Temperatur und Reaktionszeit) wurden kolloidale Quasi-2D ZnS-Nanoplättchen synthetisiert. Diese Strukturen zeigen bei Raumtemperatur eine Reihe ausgeprägter Absorptionsübergänge, die in 0D- und eindimensionalen (1D) ZnS-Nanokristallen selten beobachtet werden. Es wurde bewiesen, dass die beobachteten Merkmale im Absorptionsspektrum gut mit der echten Quasi-2D-Natur von ZnS-Nanoplättchen übereinstimmen, die aus *ab-initio*-Rechnungen abgeleitet wurde. Darüber hinaus wurde die Form-/Phasensteuerung in ZnS-Nanokristallen durch Einstellen der Schwefelmenge realisiert, die den Nanokristallen einstellbare optoelektronische Eigenschaften verleiht.

ZUSAMMENFASSUNG

Die so synthetisierten ZnS-Nanoplättchen zeigen nicht nur offensichtliche exzitonische Eigenschaften, sondern aufgrund ihrer flachen Struktur und extrem gleichmäßigen Dicke auch eine perfekte Matrix für Übergangsmetallionen. Das Einbringen von Fremdionen in Nanokristalle kann neue Eigenschaften erzeugen und die ursprünglichen verbessern. Im zweiten Teil der Arbeit wurden Mn^{2+}-Ionen durch ein angepasstes Syntheseprotokoll von ZnS-Nanoplättchen in die ZnS-Nanoplättchen eingebaut. Es wurde festgestellt, dass Form und Kristallstruktur der dotierten Nanoplättchen im Vergleich zu den undotierten unverändert bleiben. Mn^{2+}-dotierte ZnS (ZnS:Mn)-Nanoplättchen zeigen eine duale Emission im UV- und sichtbaren Bereich. Durch Ändern der Mn^{2+}-Konzentration kann das Intensitätsverhältnis der dualen Emission leicht abgestimmt werden. Der Energietransfer zwischen dem dotierten Material und dem Dotierstoff wurde im Detail untersucht, wodurch die photophysikalischen Prozesse in ZnS:Mn-Nanoplättchen aufgedeckt werden konnten. Außerdem zeigte sich, dass die Oberfläche der Nanoplättchen ein kritischer und limitierender Faktor für die effektive Energieumwandlung ist. Die Photolumineszenz-quantenausbeute von ZnS:Mn-NPLs kann verbessert werden, indem die Oberfläche der Nanoplättchen mit einer geeigneten zinkhaltigen Lösung passiviert wird.

Obwohl die Passivierung durch die Liganden die Oberflächen-Fallenzustände, engl. *trap states*, minimieren kann, zeigen die synthetisierten ZnS:Mn-Nanoplättchen immer noch eine relativ niedrige Photolumineszenz-quantenausbeute im Vergleich zu den literaturbekannten Mn^{2+}-dotierten Nanopunkten und Nanostäbchen. Außerdem wurde entdeckt, dass sich viele Mn^{2+}-Ionen aufgrund des "Selbstreinigungseffekts" auf der Oberfläche von Nanoplättchen ansammeln, was zu verschlechterten optischen Eigenschaften von ZnS:Mn-Nanoplättchen führt (z.B. geringe Photolumineszenz-quantenausbeute, inhomogener Photolumineszenz-zerfall und verkürzte Photolumineszenz-lebensdauer). Um diese Probleme anzugehen, wurde die Herstellung von typ-I-artigen ZnSe:Mn/ZnS Kern/Schale Nanoplättchen in Betracht gezogen. Die ZnS-Schale kann nicht nur die Oberflächen-Fallenzustände passivieren, um die Photolumineszenz-quantenausbeute zu verbessern, sondern auch dafür sorgen, dass Mn^{2+}-Ionen weit von der Oberfläche entfernt bleiben. Zuerst wurden ZnSe:Mn-Nanoplättchen mit der gleichen Strategie wie ZnS:Mn-Nanoplättchen synthetisiert, da beide Materialien ähnliche strukturelle Eigenschaften aufweisen. In Anbetracht der geringen thermischen Stabilität von Nanoplättchen wurde eine Niedertemperaturmethode, die sogenannte kolloidale Atomlagenabscheidung, verwendet, um ZnS-Schalen auf den ZnSe-Kernen zu wachsen. Die

ZUSAMMENFASSUNG

Bildung der ZnS-Schalen wurde durch eine Kombination von Transmissionselektronenmikroskopie und Rasterkraftmikroskopie nachgewiesen. Es zeigt sich, dass die Zerfallslebensdauer der Mn^{2+}-Emission von 27 µs auf 200 µs signifikant ansteigt und das Zerfallsverhalten bei Abscheidung der ZnS-Schale einen stärkeren monoexponentiellen Anteil zeigt, was eine homogene Verteilung der Mn^{2+}-Ionen anzeigt.

Zusammenfassend wurde ein einfaches und effektives Syntheseprotokoll entwickelt, um nicht-geschichtete Materialien (ZnS und ZnSe) lateral wachsen zu lassen. Die erhaltenen Quasi-2D Nanoplättchen weisen formabhängige optische Eigenschaften auf, die sich von den 0D und 1D Nanokristallen unterscheiden. Anschließend wurden solche Zinkchalkogenid-Nanoplättchen mit Mn^{2+}-Ionen dotiert, um eine einstellbare duale Emission zu erreichen. Um die optischen Eigenschaften von ZnSe:Mn-Nanoplättchen zu verbessern, wurden die Nanoplättchen erfolgreich mit ZnS-Schalen über das kolloidale Atomlagenabscheidungsverfahren beschichtet. Die Arbeit eröffnet einen Weg für die Synthese und die Nutzung der optischen Leistungsfähigkeit von quasi-2D Halbleiter-Nanoplättchen.

ZUSAMMENFASSUNG

List of Abbreviations

NC	Nanocrystal
NP	Nanoparticle
QD	Quantum Dot
NPL	Nanoplatelet
NR	Nanorod
NW	Nanowire
NS	Nanosheet
0D	Zero Dimensional
1D	One Dimensional
2D	Two Dimensional
3D	Three Dimensional
WZ	Wurtzite
ZB	Zinc Blende
ML	Monolayer
c-ALD	Colloidal Atomic Layer Deposition
FWHM	Full-Width at Half-Maximum
HH	Heavy-Hole
LH	Light-Hole
BE	Band Edge
CBM	Conduction Band Minimum
VBM	Valence Band Maximum
AEP	Atomic Effective Pseudopotential
DFT	Density Functional Theory
LDA	Local Density Approximation
TEM	Transmission Electron Microscopy
HRTEM	High-Resolution Transmission Electron Microscopy
FFT	Fast Fourier Transformation
SAED	Selected Area Electron Diffraction
EDXS	Energy Dispersive X-ray Spectroscopy
XRD	X-ray Diffraction
XPS	X-ray Photoelectron Spectroscopy
UV−vis	Ultraviolet−visible Spectroscopy
ICP-OES	Inductively Coupled Plasma Optical Emission Spectroscopy
EPR	Electron Paramagnetic Resonance
NMR	Nuclear Magnetic Resonance
PL	Photoluminecence
PLE	Photoluminescence Excitation
PLQY	Photoluminecence Qauntum Yield

LIST OF ABBREVIATIONS

OAm	Oleylamine
OTA	Octylamine
ODE	1-Octadecene
TOP	Trioctylphosphine
CDCl$_3$	Chloroform-d
TMS	Tetramethylsilane
DMF	N, N-Dimethylformamide
EN	Ethylenediamine

List of Figures

Chapter 1

Chapter 2

LIST OF FIGURES

Chapter 3

LIST OF FIGURES

Chapter 4

List of Tables

Chapter 3

Chapter 4

LIST OF TABLES

CHAPTER 1

Theoretical Background

1.1 Properties of Semiconductor Nanocrystals

Semiconductors with properties between those of conductors and insulators have witnessed a rapid development in practical applications. One of the appealing characteristics of semiconductors is that upon excitation they can generate an electron-hole pair (called exciton). The subsequent relaxation of excitons has the ability to emit photons. For a given bulk semiconductor, it usually emits light with fixed wavelengths since the energy bands consisting of continuous energy levels (see Figure 1-1) are independent of the bulk size and shape. When the size shrinks to approach the exciton Bohr radius, the previously fixed properties of semiconductors become size-dependent.
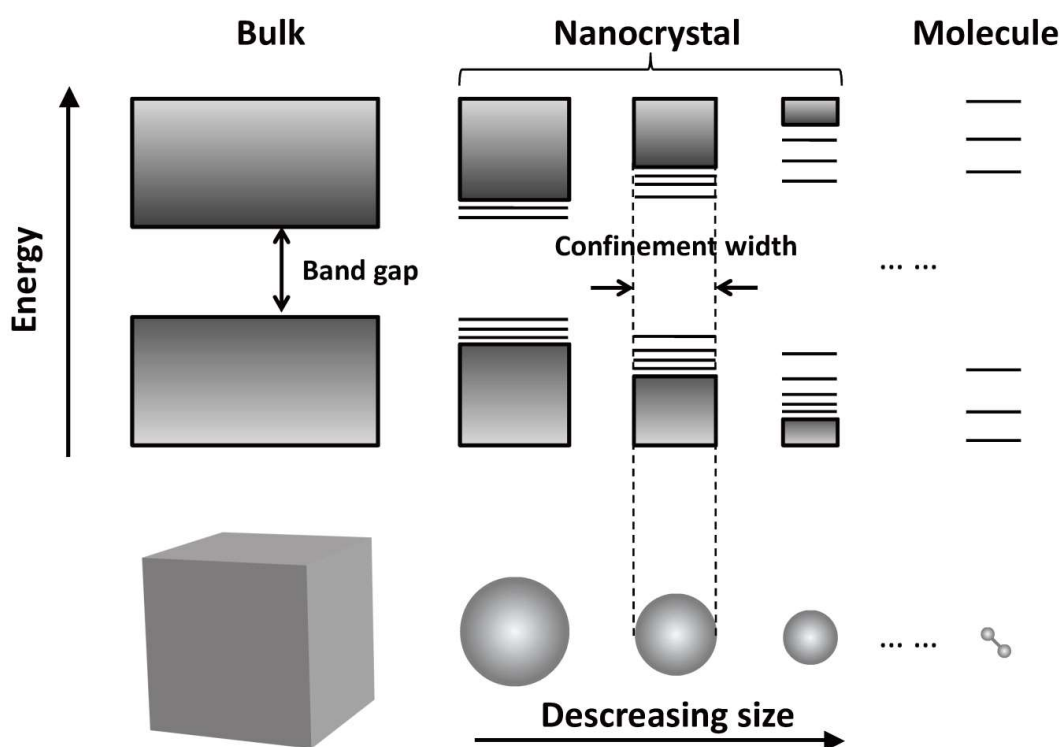
Figure 1-1. Schematic illustration of the quantum-confinement effect. For a bulk semiconductor, the electron energy levels in the valence band and conduction band are continuous. For semiconductor NCs, the levels are discrete with energies that are defined by the radius of the NCs. For a single molecule, the electron is confined in space, which allows only discrete electron energy levels. Adapted from Akkerman[2].

1.1 Properties of Semiconductor Nanocrystals

With such a small size, the wave functions of electrons and holes are spatially confined, leading to a quantization of the energy levels (see Figure 1-1). With decreasing size, the energy (band gap) required to create electron-hole pairs increases, which is known as the "quantum confinement effect".[1]

A representative illustrative example for the quantum-confinement effect is the tunability of the absorption and emission wavelength for nanocrystals (NCs) with different sizes. Quantum dots (QDs) are described as artificial atoms, and their size can be well controlled in the synthesis, thereby displaying size-dependent spectral features. As shown in Figure 1-2, the full visible emission spectrum can be achieved by changing the size of CdSe QDs.[3-4] Due to the high toxicity, however, Cd-based NCs are restricted in the practical applications, especially in areas related to food safety. Recently, nontoxic (or less toxic) and earth-abundant materials such as zinc-containing NCs[5] have attracted extensive research interest with potentials in optoelectronic and energy conversion applications.
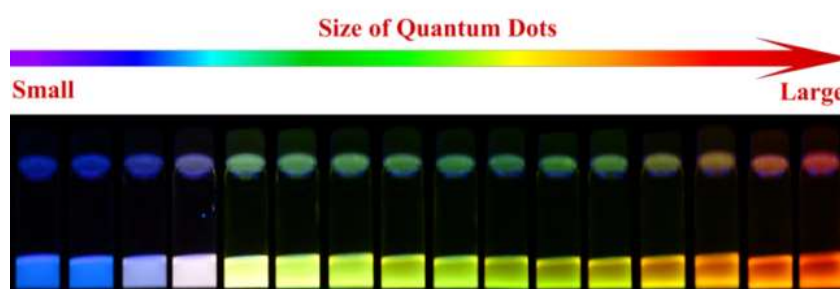
Figure 1-2. Emission colors from blue to red for CdSe QD dispersions excited by a near-ultraviolet lamp. Reproduced with permission.[3]

Apart from the size, the shape of NCs significantly influences their spectral features via selective quantum confinement in certain directions.[6] Figure 1-3 schematically shows the variation of density of states (DOS) for charge carriers as a function of energy in semiconductors with different shapes. In a three-dimensional (3D) macroscopic crystal, there is no restriction to the migration of charge carriers and the DOS based on an energy-dependent square root function is quasi-continuous. In a two-dimensional (2D) NC, the charge carriers experience a restriction along the thickness direction, resulting in

a step-like DOS. For a one-dimensional (1D) NC, a sawtooth-like DOS occurs where the charge carriers are restricted in two spatial directions. In the case of a zero-dimensional (0D) NC, the charge carriers are restricted in all three spatial directions, leading to a discrete DOS.
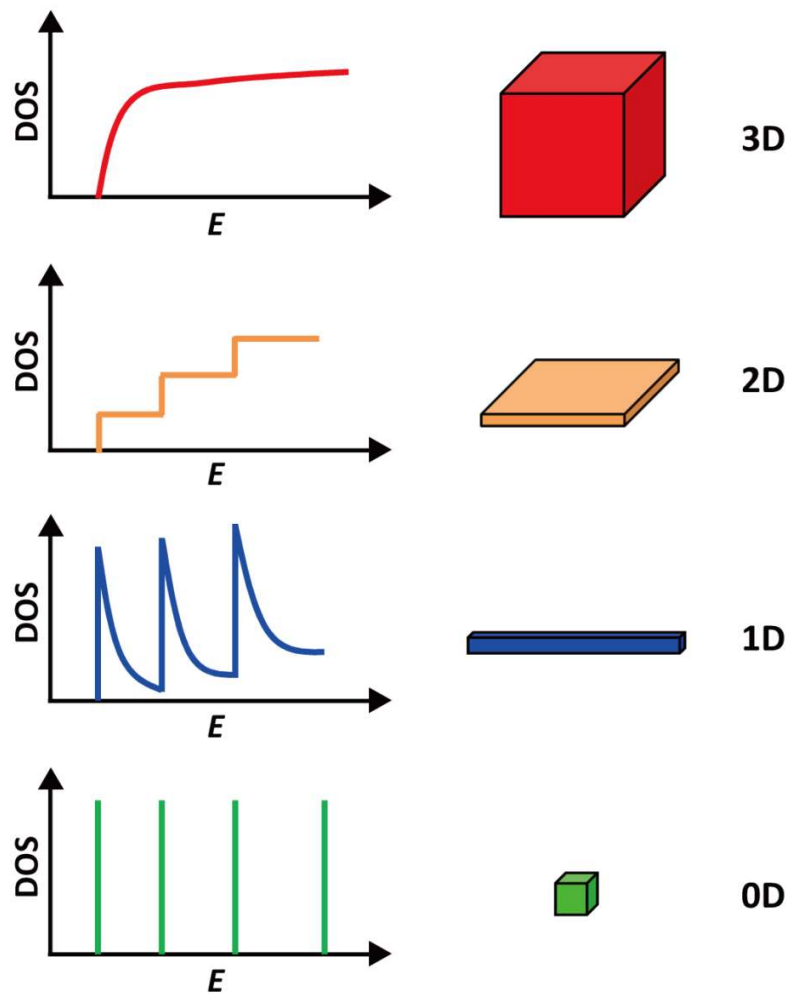
Figure 1-3. Schematic illustration of the DOS for charge carriers in 3D, 2D, 1D, and 0D semiconductors, respectively. The reduction in dimensionality changes the restriction of the charge carriers, leading to a change in the DOS. 3D (no restriction): quasi-continuous DOS; 2D (restriction in thickness): step-like DOS; 1D (restriction in diameter): sawtooth-like DOS; 0D (complete restriction): DOS with δ-function.

1.2 Synthesis of Semiconductor Nanocrystals

1.2.1 Wet-Chemical Synthesis

In the past decades, numerous synthetic methods have been developed for the fabrication of semiconductor nanomaterials. Generally, the synthetic routes can be classified as top-down and bottom-up approaches. In the top-down approach, a large piece of material is broken into desired nanomaterials. So far many top-down approaches such as ion-intercalation and exfoliation,[7] the "Scotch-tape method",[8] and sonication[9] have been developed. In the bottom-up approach, atoms or molecules are integrated to form nanostructures. This can achieve precise control over the thickness, shape, and crystal structure of the products. On the other hand, the bottom-up approach presents some advantages of being relatively low cost, modular, and scalable, and therefore it is widely applied in the synthesis of organic and inorganic namomaterials.

Wet-chemical methods (*e.g.* heating-up[10] and hot-injection[4]), as an important part of the bottom-up approaches, have achieved great success in control over the sizes, shapes, and compositions of nanomaterials by tuning thermodynamic and kinetic parameters. In a typical wet-chemical synthesis, the three key factors precursors, ligands, and solvents have to be considered with respect to the formation and growth of nanostructures. The role of precursors is to provide atoms for the growth of nanostructures. The sizes and shapes of the products highly depend on the precursor reactivity. Ligands are mainly used for colloidal stability as well as control over the morphologies of the products. As the medium for the reaction, solvents are responsible for the dissolution of the precursors and ligands and the dispersion of the final products. In some cases, solvents can also act as co-ligands.[11]

1.2.2 Classical Theory of Nucleation and Growth

The formation of nanostructures in wet-chemical synthesis can be generally described as follows: First, precursors are converted into monomers and form nuclei during the nucleation step. The obtained nuclei then further grow to form larger crystals in different manners (*e.g.* continuous deposition of monomers on the existing nuclei, attachment of nuclei, and Ostwald ripening). The spontaneous formation of nuclei is a typical

6

homogeneous nucleation process, which can be well explained by the Gibbs free energy model. The basic idea is that a thermodynamic system tends to minimize its total Gibbs free energy. For a spherical cluster, the total Gibbs free energy (ΔG) can be expressed as

$$\Delta G = 4\pi r^2 \gamma + \frac{4}{3}\pi r^3 \Delta G_v, \qquad (1\text{-}1)$$

where r is the radius of a sphere, γ is the surface energy per unit area, and ΔG_v is the difference in Gibbs free energy per unit volume. ΔG_v is defined as

$$\Delta G_v = \frac{-k_{\mathrm{B}} T \mathrm{l} \ (S)}{v}, \qquad (1\text{-}2)$$

with the Boltzmann's constant k_{B}, the temperature T, the supersaturation of the solution S, and the molar volume v. Eq. (1-1) indicates that the total Gibbs free energy consists of two terms. The positive term ($4\pi r^2\gamma$) expresses the energy of an unfavorable bonding between monomers and nuclei, which leads to an increase in the surface energy.
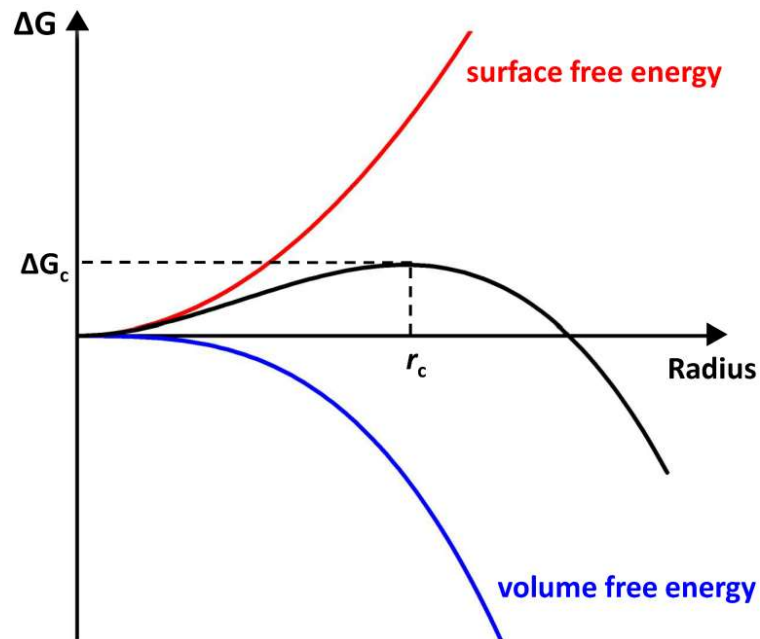
Figure 1-4. The evolution of the Gibbs free energy of a cluster as a function of radius (black curve). The changes of the surface free energy (red curve) and volume free energy (blue curve) versus radius are also shown. Adapted from Polte[12].

1.2 Synthesis of Semiconductor Nanocrystals

The negative term $(4/3\,\pi r^3 \Delta G_v)$ expresses a decrease of the Gibbs volume free energy after the bonding of monomers. Thus, this is a favorable event. Due to the competition between the increase of the surface energy and the decrease of the volume energy, it is possible to find a critical point where ΔG reaches a maximum energy value ΔG_c (named activation energy). The corresponding radius is called the critical radius r_c, which can be easily determined to be $-2\gamma/\Delta G_v$ by solving eq. (1-1) for $\mathrm{d}\Delta G/\mathrm{d}r = 0$. Figure 1-4 shows the evolution of the Gibbs free energy of a cluster as a function of the radius. For clusters smaller than r_c, growth is unfavorable due to the dominance of the positive surface energy, pushing the particles toward dissolution. For clusters with a radius larger than r_c, growth is favored because the negative term is dominant.

According to the classical growth model,[13] the growth of a NC consists of two processes. In the first process, monomers are transported from the solution to the surface of the nuclei by diffusion. In the second process, the monomers on the surface are incorporated into the crystal lattice of the nuclei by reaction. These two processes are presented in Figure 1-5.
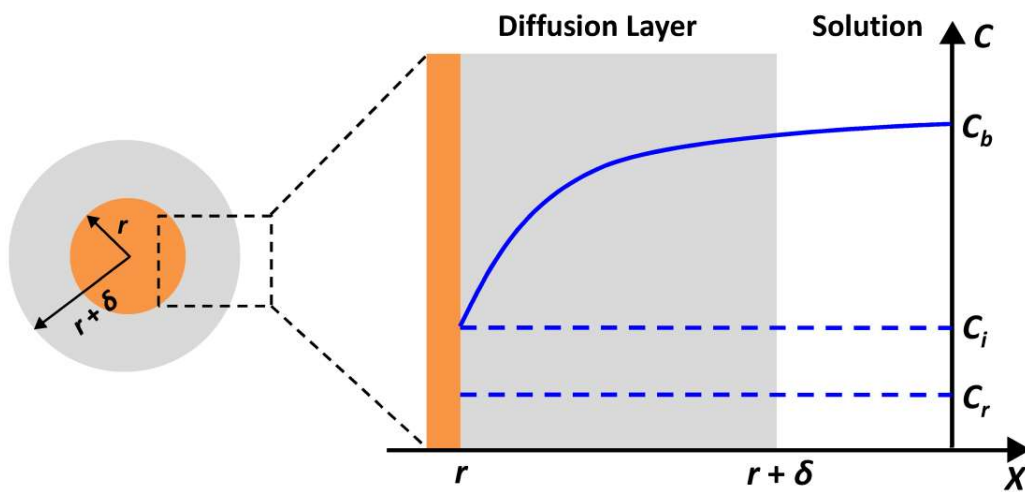
Figure 1-5. Left: Schematic illustration of the diffusion layer structure near the surface of a NC. The NC (orange) is surrounded by a diffusion layer (gray) in solution; Right: Plot of the monomer concentration as a function of distance x. Adapted from Hyeon et al.[15].

To describe the growth processes, Fick's first law of diffusion was applied:

$$J = 4\pi x^2 D \frac{\mathrm{d}c}{\mathrm{d}x}, \qquad (1\text{-}3)$$

where J is the total flux of monomers passing through a spherical plane with a radius of x, D is the diffusion coefficient, and C is the concentration of monomers at the distance x. It is assumed that a spherical NC with a radius of r is surrounded by a diffusion layer with a thickness of δ in a homogeneous bulk solution. The concentrations of monomers are C_b in the bulk solution and C_i at the solid/liquid interface, respectively. Within the diffusion layer, the concentration of monomers increases gradually in the direction away from the surface of the NCs. In this case, eq. (1-3) can be rewritten as:

$$J = \frac{4\pi D \ (r+\delta)}{\delta}(C_b - C_i), \qquad (1\text{-}4)$$

Based on the stable diffusion of monomers (J is independent of x),[14] eq. (1-4) can be simplified by integrating $C(x)$ from $(r + \delta)$ to r:

$$J = 4\pi D r(C_b - C_i). \qquad (1\text{-}5)$$

Similarly, for the surface reaction, eq. (1-4) can be simplified as:

$$J = 4\pi r^2 k(C_i - C_r), \qquad (1\text{-}6)$$

where the rate of the surface reaction (k) is assumed to be irrelevant to the size of the NCs and C_r is the solubility of the NC. Eq. (1-5) and eq. (1-6) indicate that the growth of a NC is controlled via three modes: diffusion-controlled growth, surface reaction-controlled growth, and a combination of the two modes. According to the growth mode, different equations of the growth rate can be obtained, which describes the change in the size of a NC over time.[13] For the diffusion-controlled growth and surface reaction-controlled growth, the equations of the growth rate can be written as:

$$\frac{dr}{dt} = \frac{DV_m}{r}(C_b - C_r), \qquad (1\text{-}7)$$

and

$$\frac{dr}{dt} = kV_m(C_b - C_r), \qquad (1\text{-}8)$$

respectively. t is the time and V_m is the molar volume of the solution. When the growth belongs to the third one, the growth rate can expressed as:

$$\frac{\mathrm{d}r}{\mathrm{d}t} = \frac{DV_\mathrm{m}(C_\mathrm{b}-C_\mathrm{r})}{r+D/k}. \qquad\qquad (1\text{-}9)$$

Eq. (1-9) indicates that the growth rate is determined by D and k. If $D \ll kr$ the reaction is diffusion-controlled, while if $D \gg kr$ the surface reaction is predominant.

1.2.3 LaMer and Dinegar Theory

Unlike homogeneous nucleation, heterogeneous nucleation occurs at structural inhomogeneities of the present nuclei (*e.g.* grain boundaries, impurities, and dislocations), where the surface energy needed for nucleation is very low. This results in a decrease in the energy barrier, making subsequent nucleation more preferential on the present nuclei. Thus, heterogeneous nucleation takes place much easier than homogeneous nucleation. Nevertheless, it is worth noting that both types of nucleation might occur simultaneously in an actual nanoparticle (NP) synthesis, which leads to a wide size distribution of the final products. In the preparation of monodisperse colloids, Victor LaMer et al.[16] introduced the concept of burst nucleation that separates the nucleation and growth into two stages. In the burst nucleation theory, the nucleation occurring spontaneously can be considered as the homogeneous nucleation and the later growth is a heterogeneous process. The separation of the two processes is summarized in Figure 1-6. In Phase I, the precursors are converted into monomers. As a consequence, the concentration of the monomers continually increases and reaches a critical supersaturation level (C_S) where no nucleation forms yet.[12] The concentration of monomers keeps increasing with time. In Phase II, the concentration of monomers exceeds a second level (C_n) at which the activation energy (energy barrier) for nucleation is overcome and a rapid nucleation (named "burst nucleation") initiates. Due to the burst nucleation, a huge amount of monomers are consumed shortly. As a result, the concentration of monomers drops rapidly. In Phase III, the concentration of monomers reduces below C_min ending the nucleation period. The remaining monomer will only participate in the growth of clusters via attachment to the previously formed nuclei.
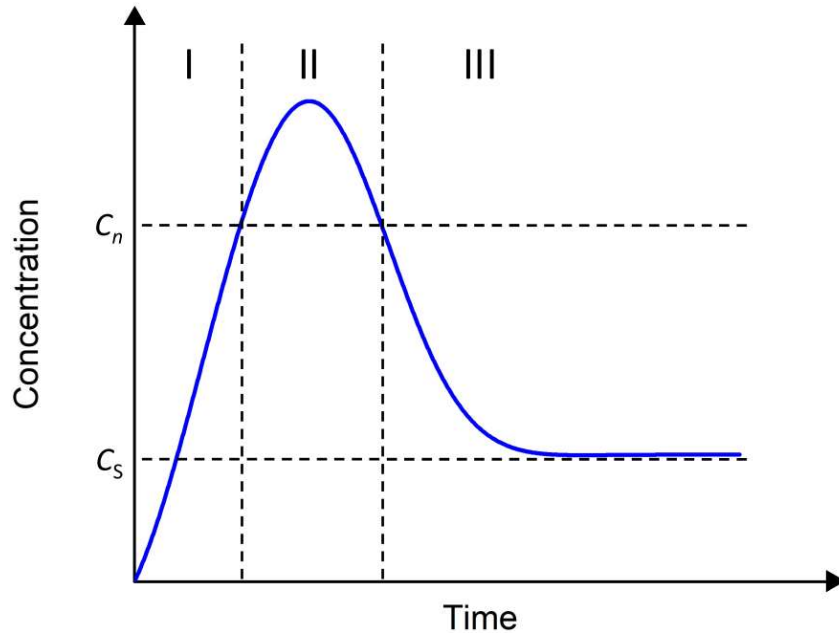
Figure 1-6. Evolution of the monomer concentration over time according to the LaMer's theory of burst nucleation. Adapted from LaMer et al.[16].

Once the growth in Phase III stops, the whole system theoretically reaches an equilibrium state where the concentration of monomers corresponds to the NC solubility (S_r).[15, 17] According to the Gibbs–Thomson equation, the value of S_r (equal to the equilibrium concentration of monomers in solution) can be approximated as:

$$S_r = S_b \exp\left(\frac{2\gamma v}{r k_B T}\right), \qquad (1\text{-}10)$$

with the solubility of the bulk material S_b. Eq. (1-10) indicates that the NC solubility is size-dependent and decreases with increasing NC radius. In an actual synthesis, the NC size distribution is usually polydisperse. Therefore, the concentration of monomers is above the solubility of large NCs, but below the solubility of small ones when the synthesis reaches an "equilibrium" system. As a consequence, the small NCs are unstable in solution and tend to re-dissolve, while the large ones continue to grow (see Figure 1-7), which leads to a broadening of the NC size distribution. This phenomenon is called "Ostwald ripening" described by Wilhelm Ostwald.[18-19]
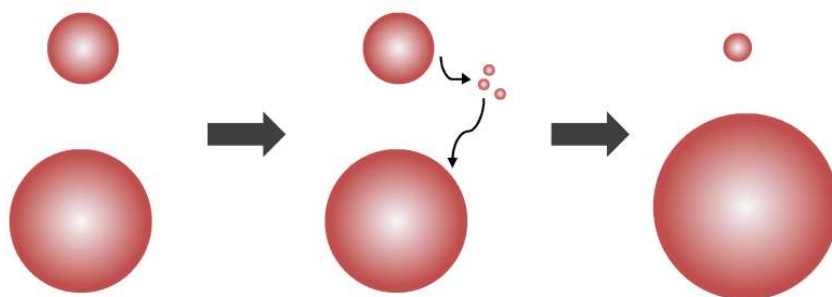
Figure 1-7. Schematic illustration of the "Ostwald ripening" process as time proceeds. Due to the high solubility (above the concentration of monomers), small NCs re-dissolve, which in turn allows large NCs to grow further. Adapted from Voorhees et al.[18, 20].

1.2.4 Other Theories

The aggregative mechanism, described as a nonclassical nucleation and growth process, is less considered compared to the LaMer mechanism and Ostwald ripening, because it does not occur very often in actual syntheses.[21-22] An aggregative process generally takes place between the classical nucleation/growth stage and Ostwald ripening stage, which is shown in Figure 1-8.
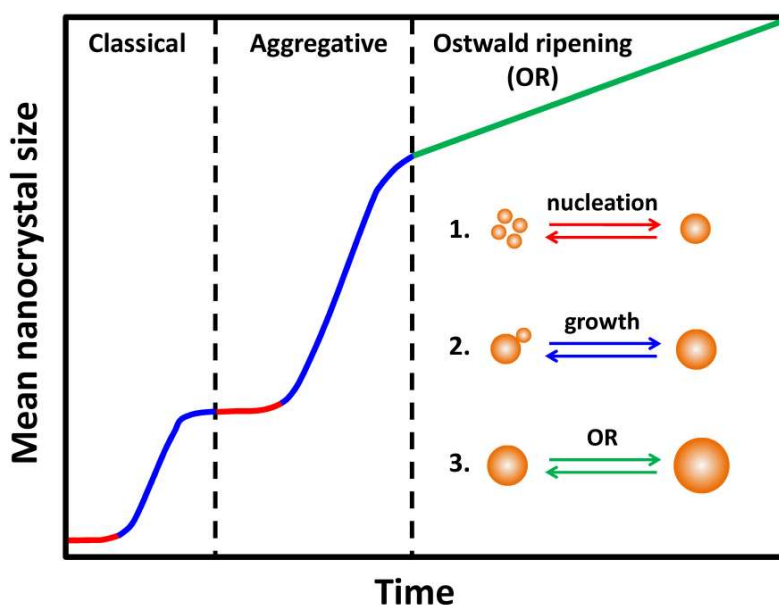
Figure 1-8. Schematic illustration of the NC growth including the classical nucleation and growth, aggregative nucleation and growth, and Ostwald ripening. Adapted from Buhro et al.[24]

1.2 Synthesis of Semiconductor Nanocrystals

In the first step, small clusters in the diameter range of 1−3 nm are generated via the classical nucleation and growth process. The clusters then aggregate and coalesce to form viable NCs that have the capability to further grow through aggregation and coalescence of subsequent clusters. This process is called aggregative mechanism. The aggregative stage may temporally overlap with the other two stages. It is worth noting that second nucleation may be present during the period of the aggregative process.[23] Additionally, NCs formed via the aggregative process exhibit a multiply twinned structure or polycrystal structure, which differs from the ones formed via Ostwald ripening.[24]

The oriented attachment can be classified as an aggregative mechanism,[24] and its growth process involves several steps presented in Figure 1-9. First of all, it is required that NCs should be free to move so that they can get close to each other. The requirement of free-moving NCs explains why the oriented attachment occurs in wet-chemical syntheses. When the NCs meet, they rotate to align with its neighbor, which can decrease the grain−grain boundary energy. Afterwards, the surfaces of the adjacent NCs merge by sharing the common crystallographic orientation. The mergence decreases the total surface energy (the number of unpassivated surface bonds is decreased), which is a main driving force for the attachment of NCs. Finally, the complete coalescence of NCs yields a new larger crystal. This phenomenon of oriented attachment has been experimentally observed in previous studies.[25-27] In particular, Yoreo's group directly observed the whole oriented attachment process of iron oxyhydroxide in real time using high resolution transmission electron microscopy (HRTEM).[28]
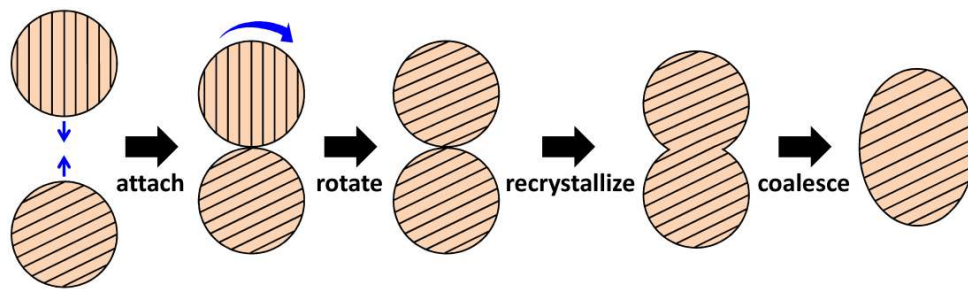
Figure 1-9. Schematic illustration of the oriented attachment mechanism. After attachment, rotation, and recrystallization, small crystals coalesce into larger crystals. Adapted from Zhang et al.[29].

1.2 Synthesis of Semiconductor Nanocrystals

In the Finke-Watzky two-step mechanism, the nucleation and growth processes take place simultaneously.[30-31] This mechanism was firstly discovered in the preparation of iridium (Ir) NPs, which is schematically shown in Figure 1-10. A slow consecutive nucleation of Ir happens via the reduction of Ir ions by hydrogen (see Figure 1-10a), followed by an autocatalytic surface growth (see Figure 1-10b). The entire process was studied by the reduction of cyclohexene. It was found that the Ir nanoclusters act as "living-metal polymers", which allows synthesizing a sequential series of increasing size nanoclusters by design. Here, four sequential series of Ir clusters, specifically Ir(0)$_{\sim150}$, Ir(0)$_{\sim300}$, Ir(0)$_{\sim560}$, and Ir(0)$_{\sim900}$ were achieved by Finke and co-workers.[30]
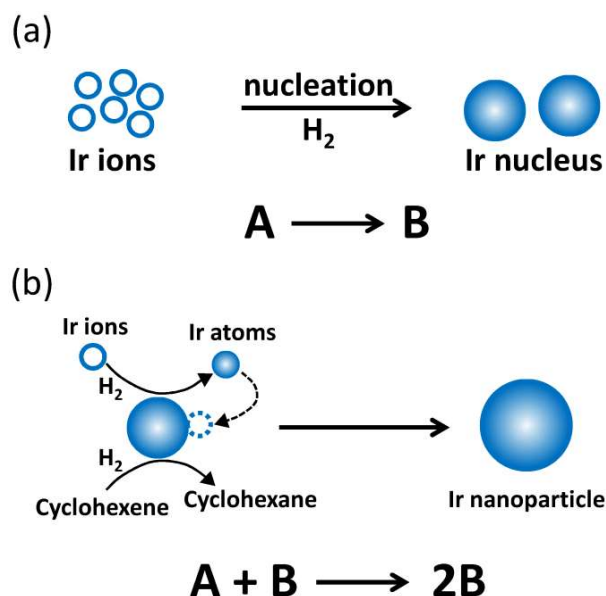
Figure 1-10. Schematic illustration of the Finke-Watzky two-step mechanism. Adapted from Perala et al.[32].

The intraparticle ripening was proposed by Peng and co-workers in studies of CdSe NCs,[33-34] which differs from the normal Ostwald ripening: it involves different crystal facets of a NC without interparticle ripening. In general, the intraparticle ripening takes places under specific conditions where the energy of monomers within the solution is lower than that of the crystal facets of NCs. In this case, there is no deposition of monomers on the surface of the NCs. Due to the presence of an energy difference between the crystal facets, the NCs are unstable, and they

tend to reshape to form a more stable structure by dissolution of higher energy facets and growth of lower energy facets, which is known as an intraparticle ripening process.

1.2.5 Shape Control: Thermodynamic and Kinetic Consideration

Thermodynamically, a NC with a fixed volume attempts to minimize its total surface free energy instead of total surface area.[35] Therefore, the final shape is dominated by the crystalline facets with low surface energies. In 1901, Wulff[36] developed a construction method (called Wulff construction) that allows one to determine the equilibrium shape of a NC. According to the Wulff construction theory, for a certain crystal facet (*hkl*), the energy (γ_{hkl}) required to create a surface of unit area on it along the direction of the vector [*hkl*] is roughly proportional to the distance of the facet to the crystal center. Hence, when the energy of all facets is known, then the equilibrium shape of a crystal can be easily plotted in a set of axes. A typical example is shown in Figure 1-11.
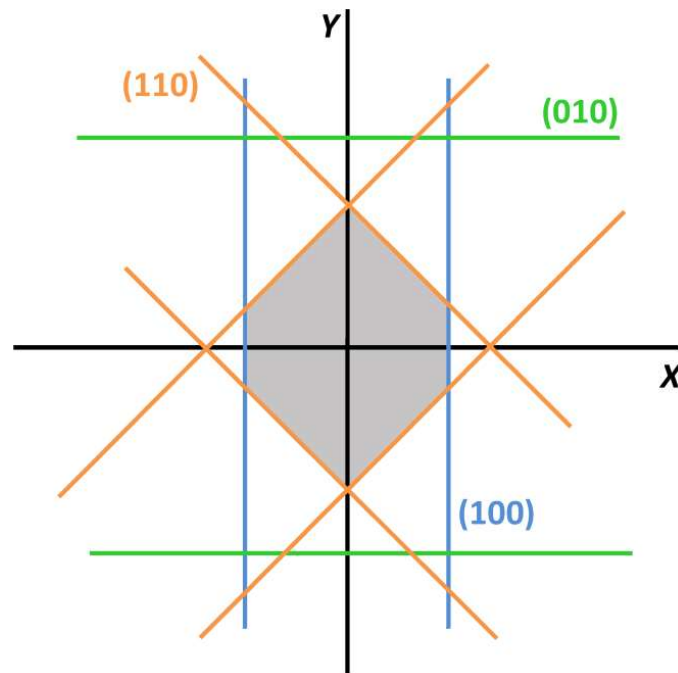
Figure 1-11. Schematic illustration of an orthorhombic structure according to the Wulff construction. The equilibrium shape (gray region) is comprised in the lines corresponding to the low energy facets. Adapted from Barmparis et al.[38].

15

1.2 Synthesis of Semiconductor Nanocrystals

The presented crystal has an orthorhombic structure with $\gamma_{100} = \gamma_{110} = 1/2\,\gamma_{010}$. In a set of *XY* axes, the (100), (110), and (010) facets can be plotted at a distance $a \cdot \gamma_{hkl}$ (where *a* is a constant) of the origin of the axes. The inner envelop (gray region) enclosed by all plotted lines corresponds to the equilibrium shape. Such a prism-like equilibrium shape has been observed experimentally for orthorhombic $CaCO_3$.[37]

Apart from the thermodynamic factors, the kinetic ones also play an important role in shape-control of NCs. As pointed out by the LaMer's theory (see Figure 1-6), the growth of a NC takes place in Phase III where the system is not in a thermodynamic equilibrium state. In this case, kinetic effects have to be taken into account. During the growth stage, the difference in growth rate on different crystal facets will dominate the shape of a NC. With a small difference, the NCs will extend in an isotropic growth mode, thereby forming spherical particles. In contrast, the NCs prefer to grow in an anisotropic mode when the difference is large and their final shape is therefore rod-like or sheet-like (platelet-like). The growth rate difference is hugely influenced by experimental parameters such as ligands, reaction temperatures, and monomer concentrations.

Ligands can selectively passivate specific facets. As a result, the growth rate on the passivated facets is slowed down. Tuning the growth rate difference via the ligand passivation is an effective way to control the shape of a NC. A typical example was reported by Weller et al.[26] in the synthesis of PbS NCs. Without 1,2-dichloroethane as ligand, cubic PbS NPs were synthesized. When 1,2-dichloroethane was added, other facets were passivated while the (110) facets remained exposed, resulting in a large growth rate difference between (110) and other facets. The fast growth on the active (110) facets finally forms PbS nanosheets (NSs). Temperature also plays a crucial role in adjusting the growth rate difference on different facets. In general, a low temperature will increase the slight energy difference between the facets and subsequently enhance the corresponding growth rate difference.[39] Once the difference is large enough, the crystal will grow anisotropically. In addition to ligands and temperature, the growth rate difference can be also tuned by changing the monomer concentration. At a low monomer concentration, growth is faster on the high energy facets due to the preferential deposition of atoms, which results in a large growth rate difference between low and high energy facets. When the monomer concentration is high, the reaction will proceed so fast that

there is not enough time for atoms to selectively deposit on the high energy facets. In this case, the atoms do not favor any facets, and the growth rate difference is small. For example, Peng's group achieved the shape control of CdSe NCs by tuning the monomer concentration.[40-41]

1.3 Metal Chalcogenide Semiconductor Nanoplatelets

1.3.1 Advantages of Semiconductor Nanoplatelets

Quasi-two-dimensional (quasi-2D) semiconductor nanoplatelets (NPLs) with lateral dimensions in ranges of tens to hundreds nanometers, but ultrathin thicknesses, typically a few monolayers (MLs) thick, have emerged as a novel class of nanomaterials.[42-44] This special 2D structure endows semiconductor NPLs some unique optoelectronic properties including high exciton binding energy, large absorption cross sections, and giant oscillator strength, which makes them promising for applications in lasing, catalysis, energy conversion and storage, and sensors.[45-47] Additionally, the flat NPLs have extremely uniform thickness that can be precisely controlled at the atomic scale, which leads to narrower spectral line widths in absorption and emission compared to 1D nanorods (NRs) and nanowires (NWs).[48] The uniformity contains two aspects: external uniformity and internal uniformity. In one batch, the synthesized NPLs usually possess monodisperse thickness (one population), which is called external uniformity. For one single NPL, the height in each area is constant, which leads to atomically flat structures (internal uniformity). These presented advantages have prompted researchers to explore the synthesis of semiconductor NPLs.

1.3.2 Synthetic Strategies for Metal Chalcogenide Nanoplatelets

The syntheses of metal chalcogenide NPLs can be classified into three categories, which is summarized in Figure 1-12. In the first approach, metal acetate or halide precursors are dissolved in long-chain amine solvents at a relatively low temperature (below 150 ℃). At the early stage of the reaction, the metal precursors and amines can form metastable lamellar structures via van der Waals attractions, which has been confirmed experimentally.[44, 49-50] With the addition of anionic precursors, small clusters

(called "magic sized clusters") form and then assemble into 2D platelets within these lamellar structures (path 1, see Figure 1-12). In 2006, Heyon's group first synthesized colloidal CdSe nanoribbons with a thickness of 1.4 nm using the template-mediated assembly method.[51] Shortly afterwards, other 2D metal chalcogenide nanostructures such as CdS[52] and CdTe[53] NPLs were synthesized using similar strategies.

In the second approach, the long-chain metal carboxylate precursors (or a mixture of metal acetate and long-chain carboxylic acids) are mixed with anionic precursors. The reaction usually takes place at a higher temperature compared to the first approach.[54] The possible formation mechanism of the NPLs is described as path 2 (see Figure 1-12). The growth of NPLs starts with small clusters that can extend laterally through monomer addition with continuous reaction of precursors. The formed NPLs can be further extended to large sheets by second injection of precursors.[55] Apart from the lateral dimension control, the thickness of the NPLs also can be tuned. Starting from 4.5 ML NPLs as seeds, Moreels's group synthesized a series of CdSe NPLs with thicknesses between 5.5 and 8.5 ML.[56]

It is interesting to note that the metal chalcogenide NPLs synthesized from the amine solvent (path 1) have a wurtzite (WZ) structure, while the ones obtained from the carboxylate (path 2) exhibit a zinc blende (ZB) structure. In 2010, Weller and co-workers[26] synthesized colloidal PbS NPLs with a rock salt crystal structure that is not found in path 1 and path 2. The formation of PbS NPLs can be assigned to 2D oriented attachment mechanisms. As shown in path 3 (see Figure 1-12), the well-defined nanoclusters attach laterally and form small patch-like structures. As the reaction proceeds, the unstable patches will coalesce into larger flat NSs via a surface reconstruction process. Some small holes can be found occasionally in the nanostructures synthesized through path 3.
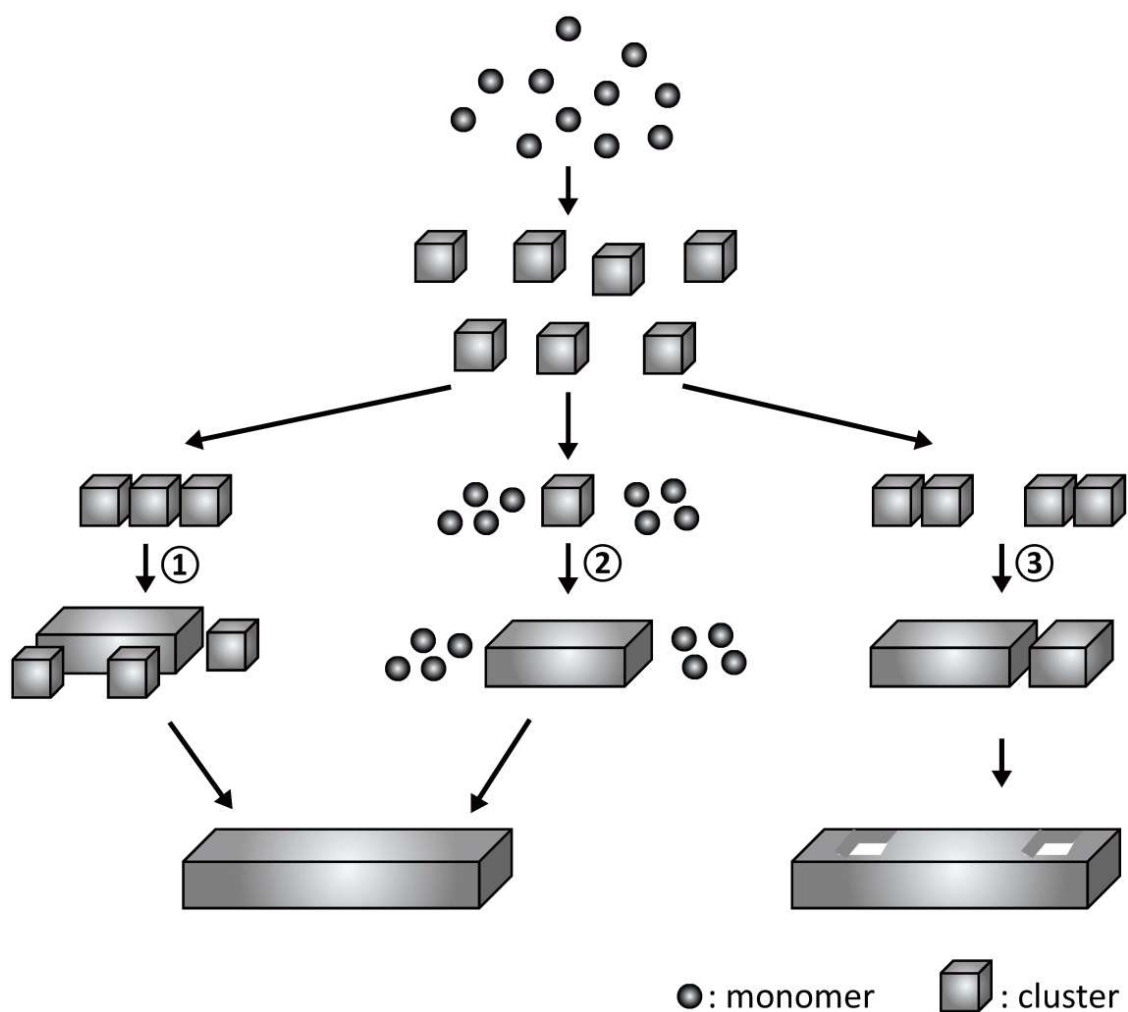
Figure 1-12. Schematic illustration of different growth paths for metal chalcogenide NPLs. Path 1: Lamellar structures guided assembly of magic sized clusters. Path 2: Lateral extension of small clusters with continuous addition of monomers. Path 3: Oriented attachment of small clusters. Adapted from Dubertret et al.[57].

1.3.3 Design of Core/Shell Nanoplatelets

Core/shell NPLs exhibit a higher photoluminescence quantum yield (PLQY), reduced PL emission blinking, larger emitting spectral range, and enhanced stability in comparison to only-core NPLs, which has attracted the attention of researchers.[54] In particular, the enhanced properties of core/shell NPLs lead to increasing interest in applications in lasers, light-emitting diodes, and biological imaging.[58-59]

1.3 Metal Chalcogenide Semiconductor Nanoplatelets

The mostly reported core/shell NPLs can be divide into three types namely type-I, type-II, and quasi-type-II. In the case of type-I (see Figure 1-13a), the band gap of the shell material is larger than that of the core material, so that both electrons and holes are confined in the core. The main role of the shell is to passivate the surface defects of the core, and thus the PLQY of the core/shell NPLs is improved. For example, the growth of a ZnS shell on CdSe NPLs boosts the PLQY by up to 60%.[60] Type-II core/shell NPLs displays staggered band alignments (see Figire 1-13b): either the valence band edge (BE) or the conduction BE of the shell material is located within the band gap of the core material. As a result, one of the charge carriers is confined in the core, while the other is in the shell. This distinct band alignment makes it possible to shift the optical features below the band gap of each material by tuning the shell thickness. In quasi-type-II core/shell NPLs (see Figure 1-13c), one of the charge carriers is confined in the core, whereas the other is delocalized throughout the whole core and shell.
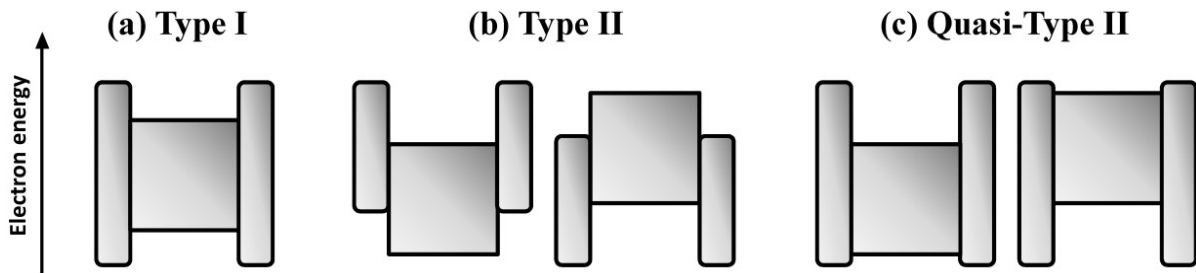
Figure 1-13. Schematic illustration of band alignments of core/shell semiconductor materials. The upper and lower edges of the rectangles correspond to the positions of the conduction and valence BEs of the core and shell materials, respectively. Adapted from Reiss et al.[61].

Inspired by syntheses of core/shell 0D QDs, high-temperature approaches such as heat-up[60] and hot-injection[62-63] have been employed to obtain core/shell NPLs. In such high-temperature approaches, the thermal stability of NPLs has to be taken into account, which can hugely affect the quality of the product. The Gibbs–Thomson equation (eq. 1-10) for spherical particles can be transferred to squared m MLs thick NPLs with a lateral size L[64] and then the solubility $S_m(L)$ can be approximated as follows:

$$S_m(L) = S_b \exp[\frac{2\gamma v}{k_B T}(\frac{1}{mh} + \frac{1}{L})], \qquad (1\text{-}11)$$

where h is the height of a ML. Eq. 1-11 indicates that the solubility of a NPL is influenced by the thickness and the lateral size. Nevertheless, the thickness is much smaller than the lateral size. Hence the solubility of a NPL is dictated mainly by the thickness. Thanks to the ultrathin thickness (typically < Bohr radius), the NPLs has much lower thermal solubility compared to that of spherical particles, which makes it difficult to grow a shell on NPLs using the high-temperature approaches.

Recently, low-temperature methods have been developed. A typical one is the colloidal atomic layer deposition (c-ALD) method that is applied firstly in the preparation of CdSe/CdS core/shell NPLs.[65] Fabrication of a binary compound shell AB commonly consists of four steps: (i) deposition of the A layer; (ii) purge to remove excess unreacted A precursors; (iii) deposition of the B layer that reacts with the A layer on the surface; and (iv) purge to remove excess unreacted B precursors. One of the advantages of this method is that the procedure can be repeated until the desired number of layers is obtained. Thus, the shell thickness can be controlled precisely at the atomic scale, which still remains challenging in the high-temperature approaches. Additionally, the reaction between A and B takes place at room temperature, which avoids the poor thermal stability issue. This promising shell growth method has been extended to syntheses of other compound core/shell NPLs including CdSe/ZnS,[60] CdSe/CdMnS,[66] and CdSe/CdS/CdZnS[67].

1.3.4 Doping

Doping, as a powerful strategy to tune the band gap of semiconductor NCs via creating electronic energy levels, has attracted much attention in the past decades. With a tiny amount of dopants introduced into the NCs, they can exhibit not only new optical, electronic, and magnetic phenomena, but also improved photo and thermal stability.[68-70] One of the goals for doped semiconductor NCs is to manipulate the PL performance. Generally, the dopant emission is red-shifted with respect to the band gap energy of the host. Therefore, the dopant emission is not absorbed by the host material, which minimizes the self-absorption issue. According to different types of dopants incorporated

into NCs, there are two scenarios for the generation of the dopant emission. The first case only involves the dopant d–d states.[71-73] Upon excitation of the host, the energy of excitons is transferred to the dopant levels, and then electrons and holes recombine within the dopant site, followed by emitting light. In this case, the dopant emission is independent of the host band gap. In the second case, only one type of charge carriers (electron or hole) is transferred to the dopant site and the other is at the host site. The recombination of electron-hole involves the host and dopant energy states,[74-75] and hence the dopant emission highly depends on the band gap of the host.

Among the doped semiconductor NCs, transition metal ions, typically Mn^{2+}, Cu^+, and Ag^+ ions, are mostly employed as dopants. Mn^{2+}-doped NCs emit a typical orange light originating from the ${}^4T_1-{}^6A_1$ d–d transitions of Mn^{2+} states,[76-77] which belongs to the first scenario mentioned above. Although the Mn^{2+}-related dopant emission is theoretically fixed, by changing the Mn^{2+} location, the type of ligands, and the Mn^{2+} concentration, the emission could also be tuned. In contrast, the dopant emission of Cu^+- and Ag^+- doped NCs can be tuned easily by changing the size of the host materials.[78]

Till now, a number of synthetic routes including nucleation/growth doping, partial cation exchange, and diffusion-controlled doping have been developed for the fabrication of doped semiconductor NCs. However, some shortcomings are still present in many doped systems. First, it still remains difficult to disperse dopants homogeneously in the host matrix. The inhomogeneous distribution of dopant ions can result in reduced optical properties such as low PLQY and impure emission. Second, it has been experimentally observed that dopant ions in ultra-small hosts tend to be expelled and easily diffuse to the surface, which is called "self-purification" effect.[71, 79] This is also detrimental to the optoelectronic properties of NCs. Third, controllable doping for achieving desired features is challenging. To solve these issues, many researchers have made great efforts. Peng's group prepared Mn^{2+}-doped ZnSe/ZnS core/shell QDs with nearly monodisperse electronic environment of Mn^{2+} ions using hot-injection method.[80] It is found that a certain amount of fatty amine is necessary to disperse Mn^{2+} ions homogeneously. They also found that the "self-purification" effect can be suppressed largely during a fast reaction (within ~5 min). In addition, the authors grew an additional shell on the QDs to ensure that all Mn^{2+} ions were far away from the surface. Pradhan et al. successfully

obtained pure dopant emission in ZnSe NCs through decoupling doping from nucleation and/or growth.[81] Cao and co-workers developed a three-step synthesis to achieve precise control of the Mn^{2+} ion radial position and doping level in core/shell dots.[82] By tuning the dopant position, the PLQY was increased up to ~60%. In a recent report, Feng et al. realized atomically precise doping of supertetrahedral nanoclusters with Mn^{2+} ions.[83] The dopant ions can be dispersed orderly to avoid the formation of clusters.

CHAPTER 2

Soft-template Mediated Synthesis of ZnS Nanoplatelets

2.1 Introduction

2.1.1 Background

Ultrathin 2D semiconductor NCs with thicknesses below their exciton Bohr radius have attracted intensive research interests since the discovery of graphene.[84-85] As briefly mentioned in Section 1.3.1 compared to 0D and 1D semiconductor NCs, 2D semiconductor NCs have highly anisotropic morphologies, leading to distinct features such as giant oscillator strength, strong quantum confinement effects, and reduced auger recombination rates.[48, 86] To date, a wide variety of 2D nanomaterials with various compositions and crystal structures have been synthesized. According to their structures, these 2D nanomaterials can be roughly divided into two categories: layered and non-layered materials. For a layered nanostructure, atoms are covalently bound within a layer but the atomic layers are connected by weak van der Waals forces. A typical example is graphite that consists of weakly stacked graphene sheets. In contrast, the non-layered materials form atomic bonding in all three spatial directions, thus 3D structures are favorable. Many metal chalcogenides (*e.g.* ZnSe, ZnS, and PbS) belong to non-layered structures.

Among 2D nanomaterials, quasi-2D semiconductor NPLs with atomically precise thicknesses are attractive, because they show superior thickness-dependent optoelectronic properties and emerge as a new class of nanomaterials. To date, many efforts have been made to prepare semiconductor NPLs. The mostly studied ones are CdSe NPLs.[48, 87-88] However, the reports on ZnS NPLs are still scarce. In 2011, Pradhan' group first obtained hexagonal ZnS NPLs by using the hot-injection method.[89] In 2014, starting from CdS NPLs, Dubertret et al. prepared rectangular ZnS NPLs via a cation exchange approach.[90] Later on, the same group reported on direct synthesis of ZnS NPLs using a one-pot method.[91] Nevertheless, no excitonic PL was reported for the mentioned structures. To the best of our knowledge, the synthesis of robust well-defined ZnS with high-quality is still a challenge.

To obtain high-quality semiconductor nanostructures, shape control have to be taken into account because of shape-dependent optical and electrical characteristics.[6, 34, 92] With the assist of a shape control strategy, semiconductor nanostructures can be tailored to

gain optimized properties. Several works have been made to achieve shape control in ZnS nanostructures. Wang et al. presented a one-pot solvothermal preparation of ZnS nanostructures from 0D NPs and 1D NWs to branched nanotetrapods in the presence of ethylenediamine (EN) as a soft template.[93] Acharya et al. showed controllable synthesis of various ZnS nanostructures including nanodots (NDs), NRs, and NWs by varying the precursor concentration, capping ligands, and annealing temperatures.[94] In addition to the shape control, the phase transition also plays a vital role in the manipulation of optoelectronic properties. It is known that ZnS exhibits polymorphism having two types of structure: the cubic ZB and the hexagonal WZ structure.[95] Thanks to differences in the atomic arrangement, the ZB-ZnS and WZ-ZnS have quite different properties. For example, the WZ-ZnS was shown to produce a spontaneous polarization and internal electric field, leading to better charge carrier separation and transfer compared to the ZB-ZnS.[96] This makes WZ-ZnS attractive for more efficient photocatalytic processes and energy conversion. Besides, Cheng et al. found that the ZB-ZnS and WZ-ZnS exhibit obvious differences in chemical activities due to the different atom-terminated surfaces.[97] In general, ZB-ZnS is a low-temperature phase,[98] while WZ-ZnS corresponding to the high-temperature polymorph forms at high temperatures (around 1023 °C).[99] Thus, it is difficult to achieve the phase transition between ZB and WZ, even if the temperature for the fabrication of WZ-ZnS has been reduced to 150 °C.[100] Recently, Pradhan et al. achieved reversible ZB/WZ phase changes in ZnS nanostructures at 300 °C by insertion/ejection of Mn^{2+} ions.[89] However, the obtained ZB-ZnS nanostructures were not pure, and the used temperature is still relatively high.

2.1.2 Motivation

In the past decade, colloidal Cd-based NPLs such as CdSe and CdS have exhibited superior optical and electronic properties based on their controlled thickness at the atomic scale, which attracts extensive attention. However, Cd-based NPLs are toxic. In comparison to CdSe and CdS, ZnS exhibits relatively low toxicity and has a large direct band gap of approximately 3.7−3.8 eV at room temperature. The small Bohr radius of 2.5 nm and the large exciton binding energy of 40 meV make ZnS a promising candidate for electroluminescence, sensor, laser technology, and photocatalysis.[101-102] Based on these

advantages, one goal is to develop a simple and effective colloidal method to synthesize high-quality ZnS NPLs. As motioned above, semiconductor NCs show shape and phase dependent properties. Hence, the second goal is to tune the shape and phase of ZnS NCs by tuning the experimental parameters.

2.2 Results and Discussion

2.2.1 Synthesis of ZnS Nanoplatelets

Soft-template approaches have been applied for syntheses of 2D CdSe, CdS, and CdTe plates,[51-53] which show potential for the fabrication of 2D NCs. The formed metastable lamellar structures in soft-template-based syntheses can guide the growth of NCs into a 2D mode. Based on this, this promising approach was applied into the synthesis of ZnS NPLs. Here, octylamine (OTA) and oleylamine (OAm) were chosen as the soft-template for two purposes. First, it has been experimentally proven that OTA exhibits appropriate reactivity for the synthesis of lamellar-structured semiconductor NSs.[44] Second, the long OAm molecular chain can serve to enhance the steric repulsion between organic layers, resulting in weakened interactions between NCs.[44, 103] In a typical synthesis, zinc chloride ($ZnCl_2$) and sulfur powder with a nominal Zn:S molar ratio of 1:3 were dissolved in a mixture of OAm and OTA, followed by purging with nitrogen at 100 °C for half an hour. Afterwards, the reaction solution was heated to 150 °C for 6 h under nitrogen atmosphere. After cooling down, the resulting NCs were purified by precipitation with acetone/isopropanol and re-dispersion in toluene or hexane for further characterization. A TEM image (see Figure 2-1a) clearly shows that the resulting NCs have a platelet-like shape with lateral dimension of 7.1 ± 0.8 and 19.4 ± 2.2 nm (see Figure 2-1b). X-ray diffraction (XRD) was performed to determine the crystal structure of the NPLs. The XRD pattern (see Figure 2-1c) indicates that the synthesized NPLs possess a hexagonal WZ phase of ZnS (ICPDS 00−080−0007).
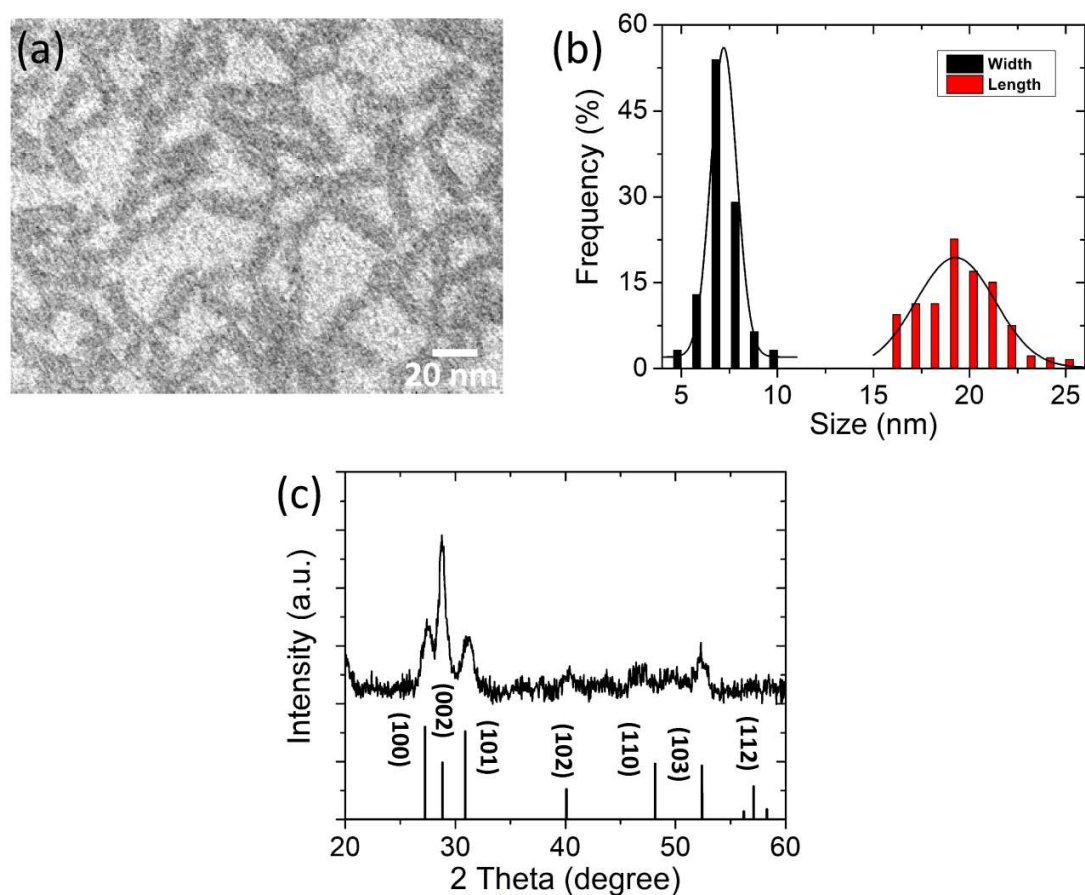
Figure 2-1. Shape and phase characterization of ZnS NPLs. (a) TEM image of ZnS NPLs synthesized with a Zn:S molar ratio of 1:3 in the synthesis. The corresponding (b) size distribution histograms and (c) XRD pattern. At the bottom, the diffractogram of the bulk ZnS (wurtzite, ICPDS 00−080−0007) is shown.

The finding of the WZ structure for the ZnS NPLs was confirmed by the selected area electron diffraction (SAED) analysis (see Figure 2-2a). A HRTEM image (see Figure 2-2b) of an individual NPL exhibits well-resolved lattice fringe patterns, illustrating that the NPL is well crystallized. The observed lattice spacings were calculated to be 3.09 and 3.27 Å, matching that of the (0001) and (10-10) planes of WZ-ZnS structure, respectively. The corresponding fast Fourier transform (FFT) (see Figure 2-2c) indicates that the [0001] and [10-10] directions span the basal plane of the NPL. Figure 2-2d exhibits the atomistic models for the WZ-ZnS NPLs, revealing that side (0001) facets are either Zn-rich (gray)

or S-rich (yellow), whereas the lateral (1-210) facets and side (10-10) facets exhibit a mixed composition of Zn and S.
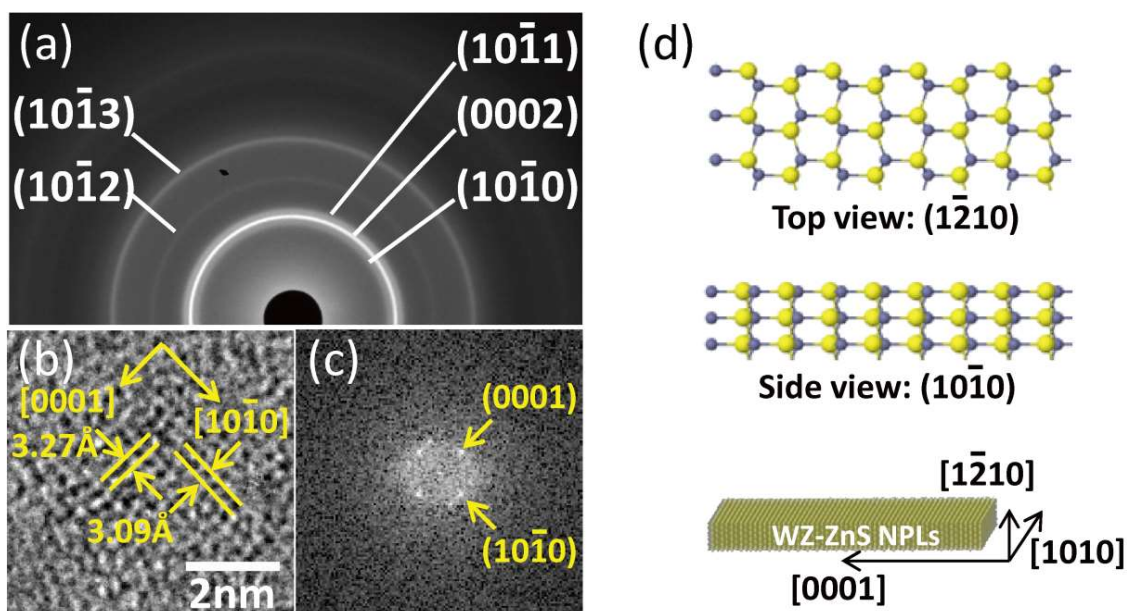
Figure 2-2. Structural characterization of ZnS NPLs. (a) SAED pattern, (b) HRTEM image, and (c) FFT pattern of ZnS NPLs synthesized with a Zn:S molar ratio of 1:3 in the synthesis. (d) Schematic illustration of the crystallographic nature of the ZnS NPLs. Gray: Zn atoms; yellow: S atoms.

The thickness of the NPLs is 1.8 ± 0.2 nm, directly measured from TEM images of stacked NPLs that stand vertically on the TEM grid (see Figure 2-3a). According to the structural parameters of WZ-ZnS (see Figure 2-3b), the NPLs were estimated to have 5 MLs along the thickness direction (1 ML corresponds to one crystal unit of WZ-ZnS).
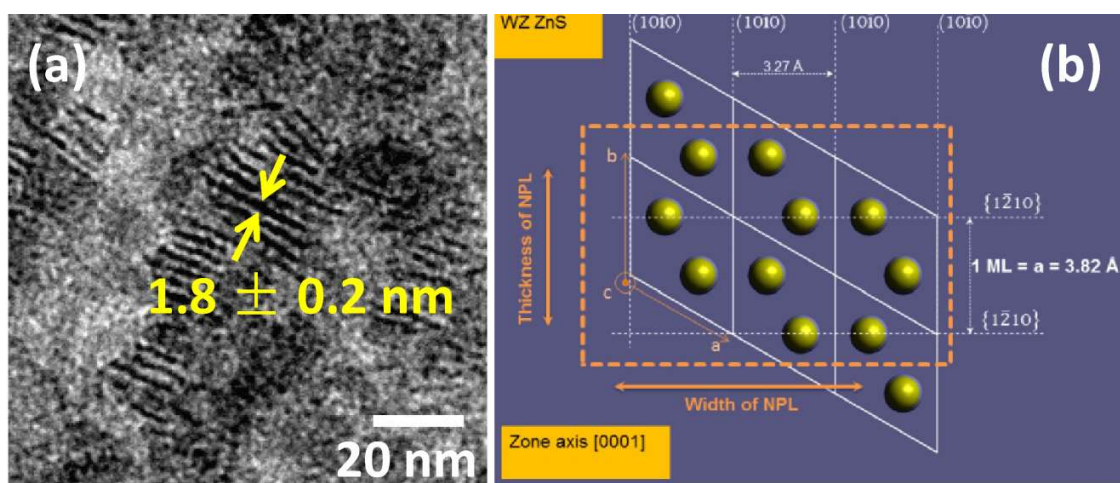
Figure 2-3. Thickness characterization of ZnS NPLs. (a) TEM image shows that ZnS NPLs synthesized with a Zn:S molar ratio of 1:3 in the synthesis vertically stand on the TEM grid. (b) Scheme for the atomic arrangement of the WZ-ZnS NPLs. Gray: Zn atoms; yellow: S atoms.

2.2.2 Optical Properties of ZnS Nanoplatelets

The optical properties of ZnS NPLs were characterized by steady-state UV−vis absorbance and PL spectroscopy. A strong and narrow peak at λ = 283 nm (4.38 eV) in the absorption spectrum was observed (see Figure 2-4a), which can be attributed to an excitonic transition substantially enhanced by the Coulombic attraction between electrons and holes. The sharpness of the absorption peak suggests that the NPLs are homogeneous in thickness (one population). The PL spectrum exhibits a distinct emission band centered at 292 nm (4.25 eV) with a full width at half-maximum (FWHM) of 105 meV, revealing a Stokes shift of 9 nm (130 meV). In addition to the excitonic peak (4.38 eV), less pronounced peaks at 4.8 and 5.62 eV with a shoulder at 5.78 eV were shown in the absorbance spectrum (see Figure 2-4b). The appearance of several absorption features in the spectra of colloidal CdSe NPLs has been reported, which is attributed to electronic transitions from h_0 (heavy-hole (hh) in ZB or A-band in WZ), h_1 (light-hole (lh) in ZB or B-band in WZ), and h_2 (spin−orbit (so) in ZB or C-band in WZ) valence bands to the e_0 (first conduction band or conduction band minimum (CBM)),[48] as well as interband transitions from lower valence to higher conduction bands.[104] Particularly, the main absorption peak of CdSe NPLs was shown to originate from hh−e_0 and lh−e_0 transitions,[48]

separated by ca. 180 meV for the ZB[43] and 220 meV for the WZ NPLs.[87] However, the splitting of the absorption bands based on the level structure of the top of the valence band was shown to be smaller for bulk ZnS films[105] because of lighter atoms and hence weaker spin−orbit coupling. Pronounced hydrogenic 1s, 2s lines were observable even at room temperature, and the so−e_0 transition smeared out after heating over 200 K.
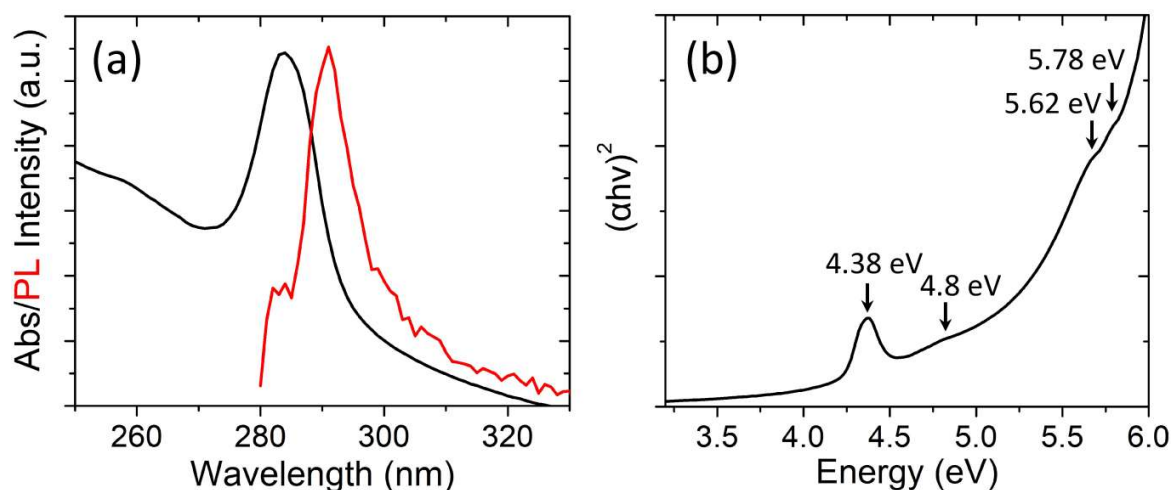
Figure 2-4. Optical characterization of ZnS NPLs. (a) UV−vis absorbance (black) and PL (red) spectra of ZnS NPLs synthesized with a Zn:S molar ratio of 1:3 in the synthesis. (b) $(\alpha h \nu)^2$ vs photon energy representation of the absorbance spectra for ZnS NPLs.

To figure out the origin of the absorption features in the spectrum of ZnS NPLs, *ab initio* calculations using atomic effective pseudopotentials (AEPs)[106-108] were performed in the framework of cooperation with the group of *Prof. Gabriel Bester* with contributions from *Dr. Anastasia Karpulevich* and *Dr. Abderrezak Torche*. A WZ-ZnS slab with a growth direction of [11-20] and a thickness (5 MLs) of 1.91 nm was used as the calculation model. From the theoretical simulation of the dipole transitions using Γ-point wave functions, it can be concluded that the first absorption peak corresponds to a sum of three transitions, namely, from the h_0, h_1, and h_2 nodeless states derived from the A-, B-, and C-bulk valence (WZ) bands to the e_0 nodeless state CBM. The experimental absorption spectrum and the calculated dipole allowed transitions along with the eigenvalues and eigenfunctions are presented in Figure 2-5.
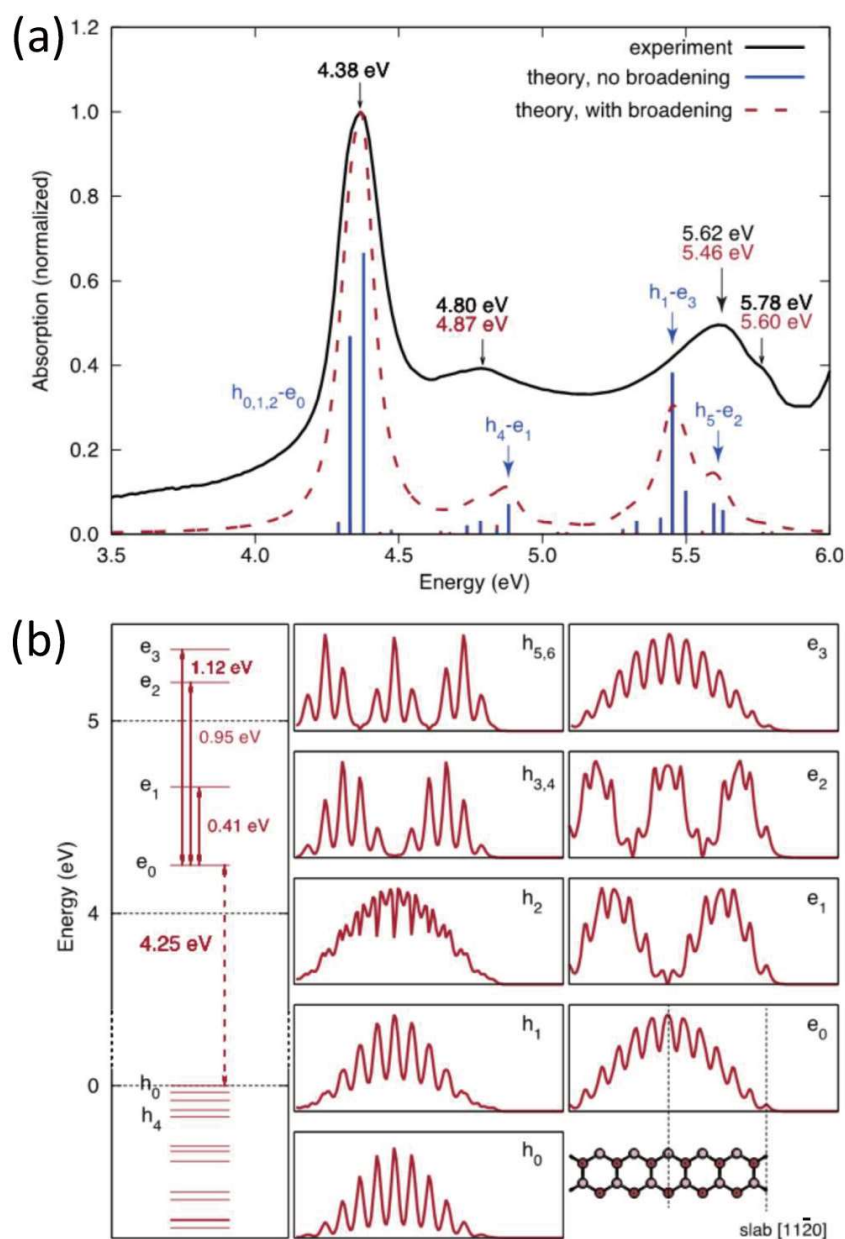
Figure 2-5. *ab initio* simulations of absorption features for the WZ-ZnS NPLs. (a) Normalized absorbance spectrum (black solid) of WZ-ZnS NPLs after subtraction of a scattering background along with calculated dipole transitions (red dashed). The first exciton energy was fitted to the experimental value and a temperature broadening was applied to the results. (b) Single particle eigenvalues at Γ-point (left) and 1d atomistic wave functions (right) of the relevant near-band gap states (see experimental section). Atomic structure of the ZnS slab used in the simulations (bottom right).

2.2 Results and Discussion

It appears that the observed first absorption peak is dominated by the third valence band state (h_2), which has an offset from the valence band maximum (VBM or h_0) less than 100 meV. Obviously, the dominant h_2 state in the absorption peak contributes to the observed considerable Stokes shift. The calculations show that crystal field and spin−orbit splitting between hh, lh and so states in the valence band for the 2D ZnS NPLs with experimental thickness (1.82 nm) are in the range of tens of meV and hence not large enough to produce experimentally distinct absorption peaks. The latter two peaks (4.8 and 5.62 eV) and the weak shoulder (5.78 eV) correspond to h_4−e_1 transition, h_1−e_3 transition, and h_5−e_2 transition, respectively.

The agreement between the calculations and the experimental results is qualitatively good with some quantitative differences. It can be seen that the second simulated peak (4.87 eV) slightly shifts to higher energy and the third simulated peak (5.62 eV) and shoulder (5.6 eV) slightly shift to lower energy compared to the experimental peaks. Note that the band gap of the single NPL in simulations is 4.25 eV, which is over 100 meV below the experimental result. The differences are attributed to the lack of correlation effects in the calculations and possibly the presence of out-of-plane strain, which would explain our underestimated band gap. Indeed, owing to surface reconstruction, the interatomic distances may be altered leading to the appearance of strain and to a shift of bands.[109] Analyzing the XRD data (see Figure 2-1c), it is noted that the (002) reflex corresponding to the lateral direction exactly coincides with the reference. However, the (10-10) and (10-11), which contains information from directions piercing the flat basal plane of NPLs at an angle different from zero, shift to higher angles. This might be attributed to the presence of compressive strain in the thickness direction. In any case, the large blue shift (ca. 0.6 eV) of the excitonic absorption peak relative to the bulk WZ-ZnS band gap (3.77 eV)[110-111] indicates the existence of a very strong 1D quantum confinement effect,[112] which is mainly attributed to the ultrathin thickness of the NPLs. The present results explain the relatively large broadening of the first absorption band in comparison with the PL and absorption broadening of CdSe NPLs since it consists of unresolved hh-, lh-, and so-valence band contributions ($h_{0,1,2}$−e_0 transitions) in the case of the WZ-ZnS NPL.

2.2 Results and Discussion

2.2.3 Formation Mechanism of ZnS Nanoplatelets

The formation of the ultrathin ZnS NPLs is ascribed to the soft-template-guided growth mechanism. It has been reported that the alkylamines and inorganic metal halides can form a lamellar structure via van der Waals attractions between hydrocarbon side chains of the alkylamine.[44, 49-50] Such a lamellar structure can direct the lateral growth of NCs to form 2D NSs and NPLs.

To verify the presence of the [$ZnCl_2$ (OTA, OAm)$_x$] lamellar structure (x represents the total number of N atoms in OTA and OAm molecules coordinated with Zn atoms), the following control experiments were conducted. A certain amount of $ZnCl_2$ dissolved in a mixture of OTA and OAm was degassed at 100 °C for half an hour. After cooldown, the precipitate was collected by addition of acetone to the reaction solution, centrifugation, and removal of the supernatant. A representative solution ^{1}H nuclear magnetic resonance (NMR) spectrum of the purified product is shown in Figure 2-6a. From this spectrum (see Figure 2-6a, blue), the characteristic resonances of OTA and OAm at 2.6 and 5.3 ppm can be observed, indicating that the product is composed of OTA and OAm. The formation of the [$ZnCl_2$ (OTA, OAm)$_x$] complex was confirmed by a TEM image (see Figure 2-6b) of the product (Inset: white solid dissolved in hexane) collected upon precipitation. From the TEM image, irregular bundled strands with weak contrast can be clearly seen, suggesting that they mainly consist of organic species. The XRD pattern (see Figure 2-6c) shows that the complex possesses a lamellar structure. The series of XRD peaks can be assigned to "00l" (l = 1, 2, 3, 4, ...) with a layer spacing (d) of ~4.56 nm that approximately equal to the double length (4.88 nm) of the OAm molecule chain. The length of the OAm molecule chain is calculated to be 2.44 nm according to the formula, L (nm) = 0.15 + 0.127n,[113] where n is the number of carbon atoms in the alkyl chain. The slight difference (ca. 0.32 nm) could be ascribed to two reasons. First, it is important to note that the calculated value (2.44 nm) for the case where the alkyl chain of OAm is fully expanded,[113-114] whereas the actual value of the OAm length should be smaller than 2.44 nm due to the bending of the molecule chain in the reaction solvent. Second, the interpenetration (η) of the OAm molecule chains leads to a decrease in the interlay distance. Similar interpenetration structures of the OAm bilayer has been reported in the synthesis of CdSe nanobelts.[115]
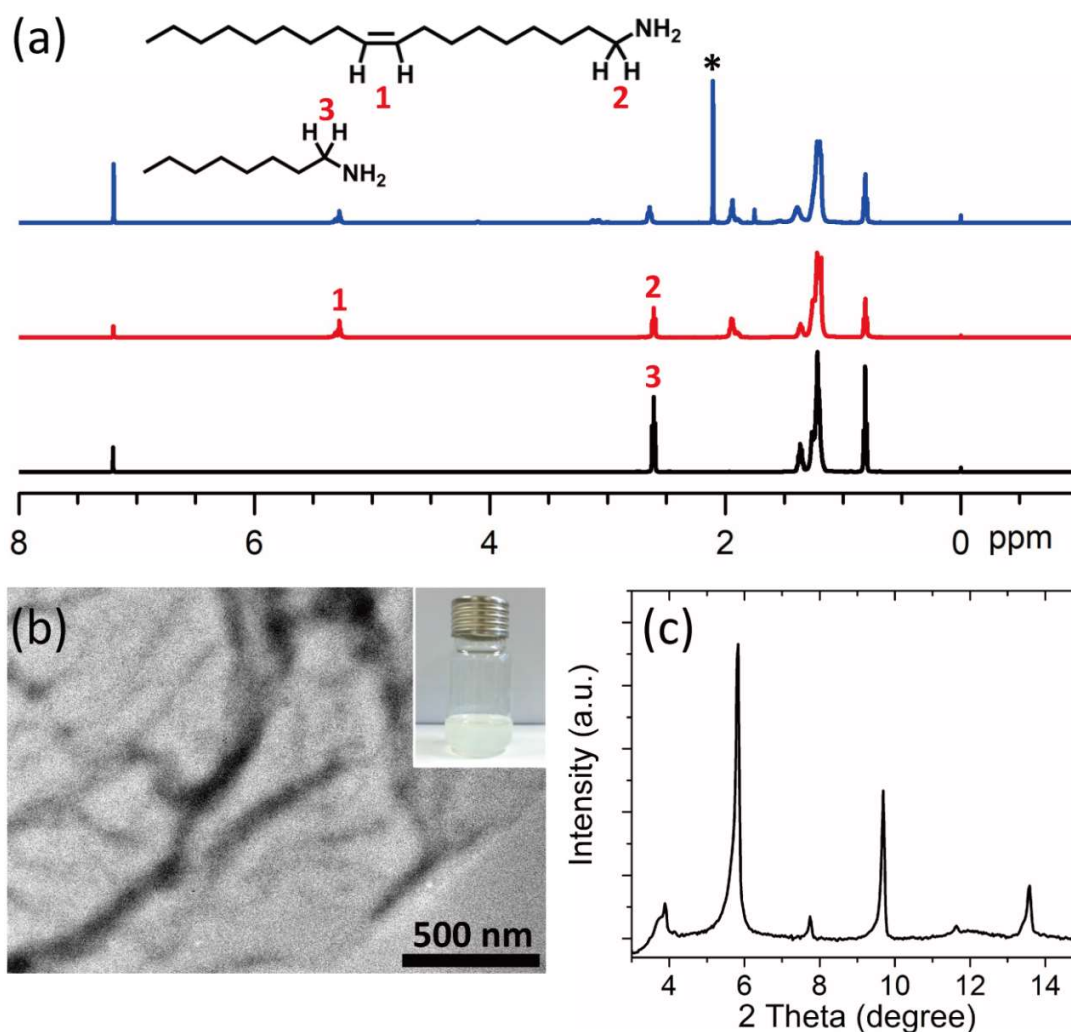
Figure 2-6. Characterization of the soft templates. (a) ^{1}H NMR of [ZnCl$_2$ (OTA, OAm)$_x$] complex in CDCl$_3$. The peaks are indexed as indicated in the spectrum. OTA (black), OAm (red), [ZnCl$_2$ (OTA, OAm)$_x$] complex (blue), and acetone (solvent) marked with an asterisk. (b) TEM image and photograph (inset) of the [ZnCl$_2$ (OTA, OAm)$_x$] strands formed from OTA, OAm, and ZnCl$_2$. (c) XRD pattern for the polymer strands.

Based on the above experimental results, the estimated overall synthetic procedure for the ZnS NPLs can be described with the schematics in Figure 2-7. At the initial stage of the reaction, ZnCl$_2$, OTA, and OAm assemble into the [ZnCl$_2$ (OTA, OAm)$_x$] lamellar structure at 100 °C. The newly formed [ZnCl$_2$ (OTA, OAm)$_x$] complex is employed as a

soft template to guide 2D growth of ZnS NCs. With further increase of the temperature, ZnS NPLs capped with OTA/OAm are obtained.
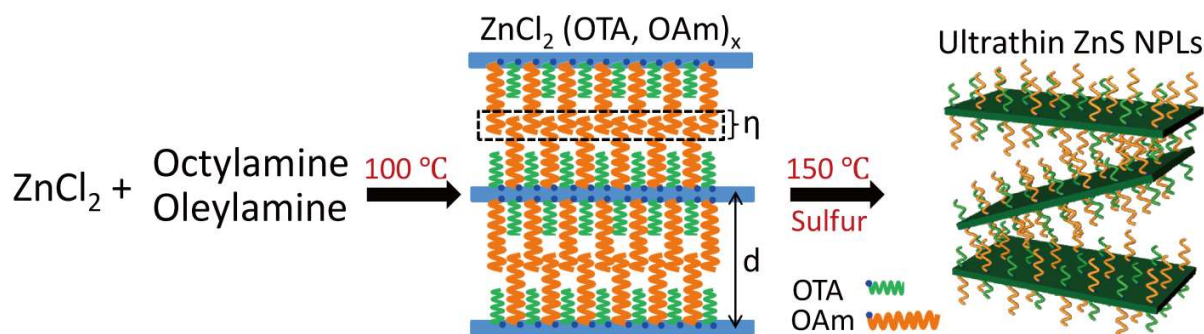
Figure 2-7. Schematic illustration of the formation of the ultrathin WZ-ZnS NPLs.

2.2.4 Influence of Oleylamine/Octylamine as Ligands

In the template-guided synthesis, the soft templates apparently play an important role in affecting the morphology of the final products. Here, the volume ratio between OAm and OTA ($R = V_{OAm} / V_{OTA}$) was tuned and other parameters were fixed. A series of TEM images (see Figure 2-8, a−g) show the morphology evolution of ZnS NCs upon varying R. When only OAm was added, small ZnS NPs with irregular shapes were synthesized (see Figure 2-8a). A similar result was seen (see Figure 2-8b) as R was set to 8/1. This is not surprising, because the OAm volume is still dominant. R then was decreased to 2/1 and rectangular ZnS NPLs with uniform size were prepared (see Figure 2-8c). This observation indicates that a proper amount of OTA is essential for the formation of NPLs. With further decreasing R to 1/1, irregular NPs formed in addition to the ZnS platelets (see Figure 2-8d). When the OTA volume fully exceeded the OAm volume ($R < 1/1$), aggregated ZnS NSs with different contrast were observed (see Figure 2-8, e−g). The aggregation of NSs is probably due to the lack of long-chain ligands on the particle surface. Apart from the morphology evolution, it is also found that the size of the product increased dramatically with decreasing R, which could be related to the reaction activity of the mixed solvent. The crystal structure of the products obtained at different R was determined by XRD. It turns out that all the products have a WZ structure of ZnS (ICPDS 00−080−0007) (see Figure 2-9).
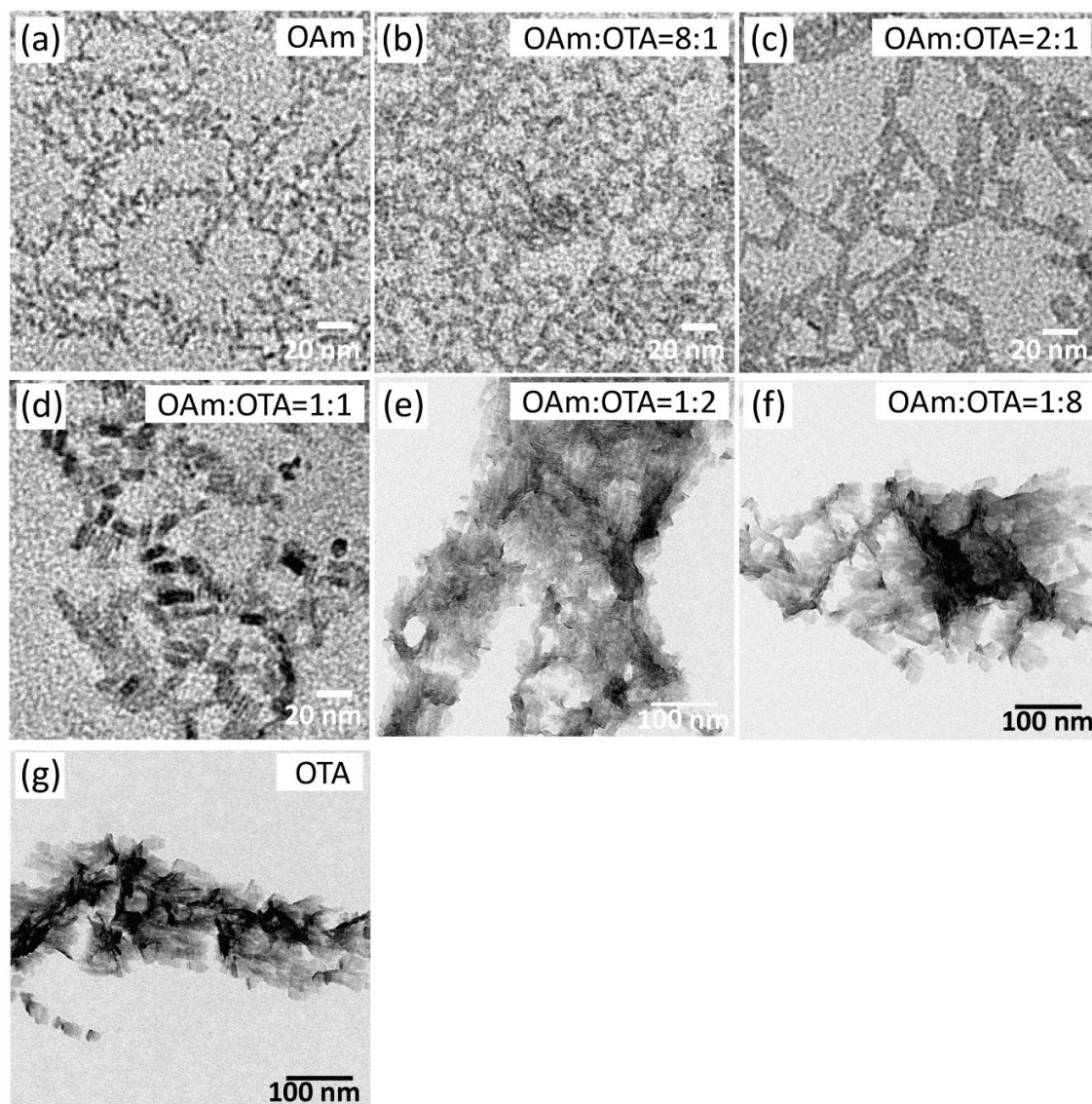
Figure 2-8. Influence of the volume ratio between OAm and OTA on the shape of ZnS NCs. TEM images of (a, b) small ZnS NPs (pure OAm, R = 8/1), (c) ZnS NPLs (R = 2/1), (d) a mixture of ZnS NPLs and NPs (R = 1/1), and (e−g) ZnS NSs with irregular shapes (R = 1/2, 1/8, and pure OTA).

The R-dependent experiments demonstrate that both OTA and OAm take part in the assembly of the soft template needed for the formation of the ZnS NPLs with uniform thickness, indirectly confirming that the bilayer structure is responsible for the 2D formation of ZnS. However, the phase choice (WZ) was not dependent on R.
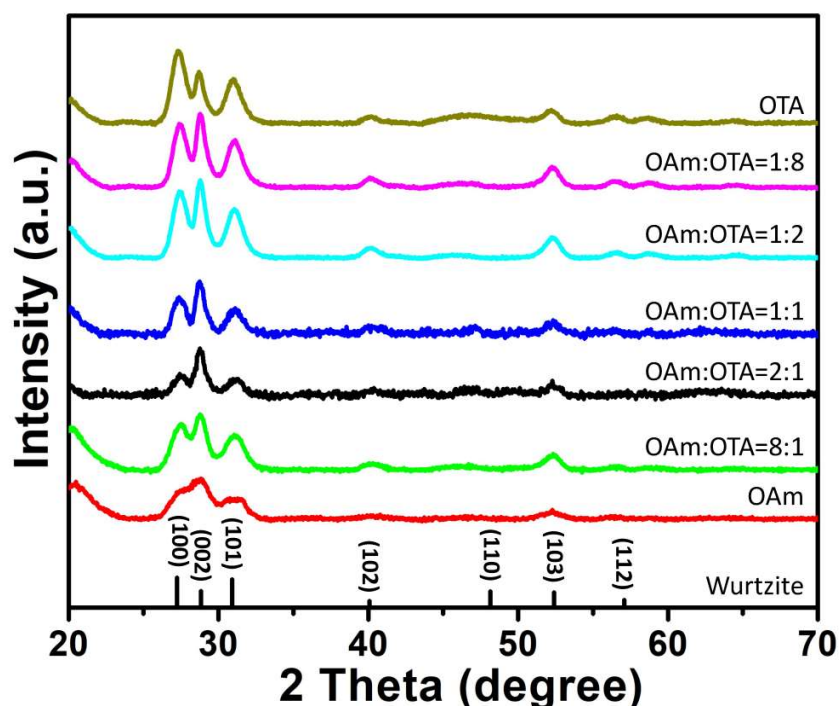
Figure 2-9. Influence of the volume ratio between OAm and OTA on the crystal structure of ZnS NCs. XRD patterns of ZnS NCs synthesized with different volume ratios between OAm and OTA. At the bottom (WZ, ICPDS 00-080-0007), the diffractograms of the bulk ZnS is shown. The XRD patterns are vertically shifted for clarity.

2.2.5 Shape/Phase Transformation of ZnS Nanocrystals

In addition to the volume ratio between OTA and OAm, the influence of the amount of sulfur on the shape and phase of ZnS was studied in detail. A series of syntheses with varying the amount of sulfur while keeping all other parameters constant were conducted. It is noted (see Figure 2-10, a−f) that the shape of ZnS NCs changes upon increase of the amount of sulfur. With a small amount (0.45 mmol) of sulfur, homogenous ZnS NPLs were synthesized (see Figure 2-10a). When the amount of sulfur was increased from 0.45 to 4.05 mmol, the shape of NCs changed from NPLs to a mixture of NPLs and NRs (0.90, 1.35, and 2.70 mmol, see Figure 2-10, b−d) to NRs (4.05 mmol, see Figure 2-10e). The average diameter of the rods is 2.8 ± 0.3 nm (see Figure 2-11, blue) directly measured from TEM images. Further increase in the amount of sulfur to 8.1 mmol, thicker rods with a mean diameter of 3.6 ± 0.4 nm were obtained (see Figure 2-11, olive).

40
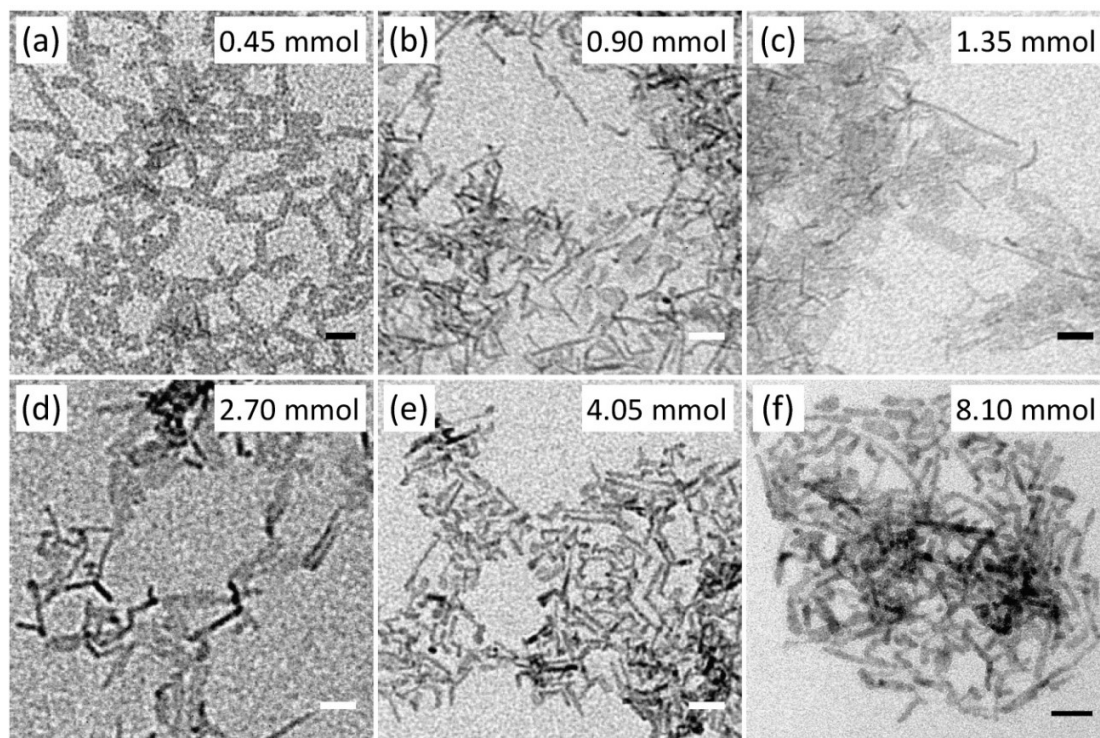
Figure 2-10. Shape transformation of ZnS NCs controlled by the amount of sulfur. TEM images of (a) ZnS NPLs (0.45 mmol), (b−d) a mixture of ZnS NPLs and NRs (0.90, 1.35, and 2.70 mmol), and (e, f) ZnS NRs (4.05 and 8.10 mmol). The scale bars represent 20 nm.
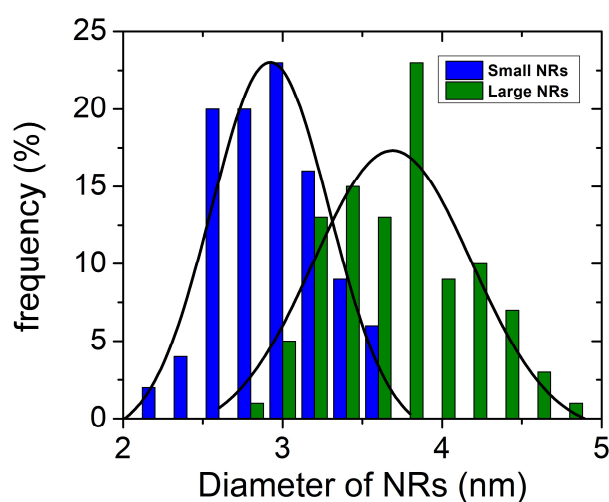
Figure 2-11. Size distribution histograms of ZnS NRs synthesized with 4.05 (blue) and 8.1 (olive) mmol sulfur, respectively.

2.2 Results and Discussion

The sulfur-dependent shape evolution of the ZnS NCs shows that the NPLs are formed preferentially at a relatively small amount of sulfur. When the amount of sulfur was continually decreased to 0.3 and 0.15 mmol, only small ZnS NPs with irregular shapes were obtained (see Figure 3-12a and b). This result suggests that the minimum required amount of sulfur for the formation of the NPLs is around 0.45 mmol.
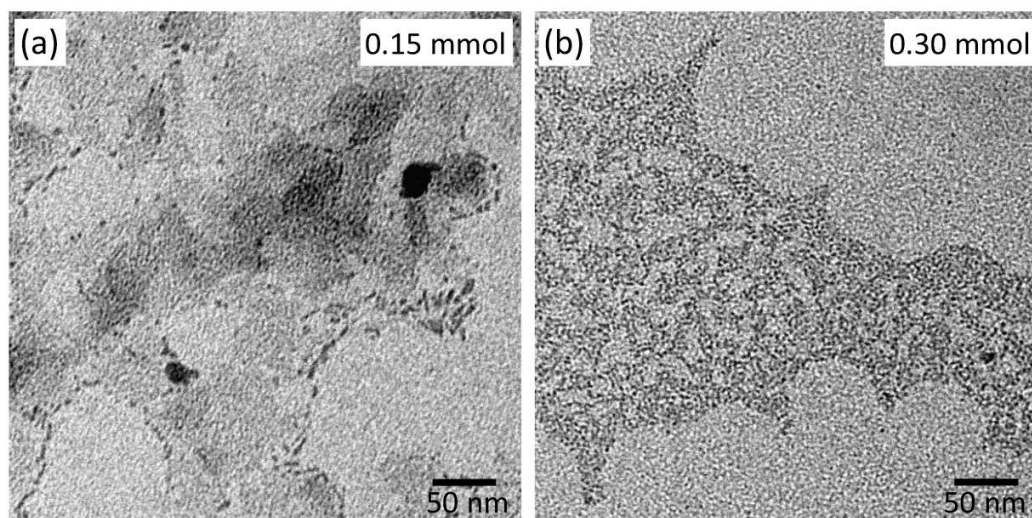
Figure 2-12. Shape transformation of ZnS NCs controlled by the amount of sulfur. TEM images of ZnS NCs synthesized with (a) 0.15 and (b) 0.3 mmol sulfur, respectively.

To study the influence of the amount of sulfur on the crystal structure of ZnS NCs, XRD was performed. The XRD patterns (see Figure 2-13) reveal that a change in the crystal structure from WZ to ZB occurred, accompanied by the shape evolution of ZnS NCs from NPLs to NRs (see Figure 2-10) with the amount of sulfur. At a small amount (0.45 mmol) of sulfur, the characteristic diffraction peaks correspond to the WZ structure of ZnS (ICPDS 00−080−0007). Upon increase in the amount of sulfur from 0.45 to 2.7 mmol, the hexagonal (100), (101), (102), and (103) peaks diminish gradually, while the characteristic peaks of cubic (111), (220), and (311) planes corresponding to the ZB structure of ZnS (ICPDS 00−077−2100) become discernible. When the amount of sulfur exceeds 2.7 mmol, the XRD pattern (see Figure 2-13, cyan and pink) displays all characteristic peaks of the ZB-ZnS pattern without impurity peaks. It was reported that the width of the diffraction peaks correlates with the growth direction for the ZB-ZnS

NWs.[116] A narrow peak and a broad peak are assigned to long axis directions and short axis directions, respectively. Thus, for the ZB-ZnS NRs, the narrowest (111) and broadest (220) peaks uncover that the long axis grows along [111] direction and the short axis is along [220] direction. Besides, it is discovered that the (220) peak corresponding to the diameter of NRs narrows (FWHM: from 2.9 to 2.4 degree) as the amount of sulfur is increased from 4.05 to 8.1 mmol, indicating that the average crystallite sizes are larger. The mean diameters of the two different NRs, as estimated from Scherrer's equation by fitting the (220) XRD peak, are 2.99 and 3.63 nm, which is nearly consistent with the sizes determined by the TEM observations.
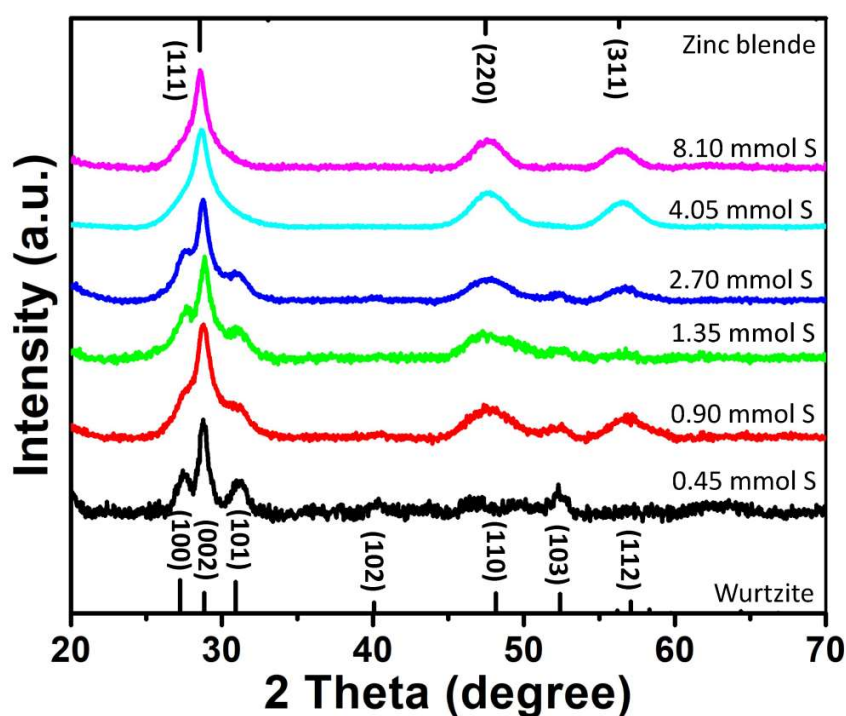
Figure 2-13. Phase transformation of ZnS NCs controlled by the amount of sulfur. XRD patterns of ZnS NCs synthesized with increasing amounts of sulfur. At the bottom (WZ, ICPDS 00−080−0007) and the top (ZB ICPDS 00−077−2100), the diffractograms of the bulk ZnS are shown. The XRD patterns are vertically shifted for clarity.

The ZB structure of the ZnS NRs is confirmed by SAED pattern, HRTEM image, and FFT pattern. The SAED pattern (see Figure 2-14a) corresponds to reflections from two

43

crystal planes, indicating (111) and (220). The distinct lattice spacings shown in the HRTEM image (see Figure 2-14b) were measured to be ~3.13 Å, matching the (111) plane spacing of the bulk cubic ZB-ZnS structure (ICPDS 00−077−2100). It is also observed that the [111] crystallographic axis is parallel to the long axis of the rod, indicating that the rod grows along the [111] direction, a thermodynamically favorable growth direction of ZB-ZnS.[116] This observed [111] growth direction is supported by the corresponding FFT pattern (see Figure 2-14c), which is consistent with the XRD observations (see Figure 2-13). The atomic models for the ZB-ZnS NRs as discussed above are shown in Figure 2-14d, revealing that the basal (111) facets are either Zn-rich (gray) or S-rich (yellow), while the side {110} and {11-2} facets are mixtures of Zn and S. In addition, the energy dispersive X-ray (EDX) spectrum of the rods (see Figure 2-15) suggests the atomic ratio of Zn:S to be 0.95:1, in agreement with the stoichiometric ratio of ZnS compound.
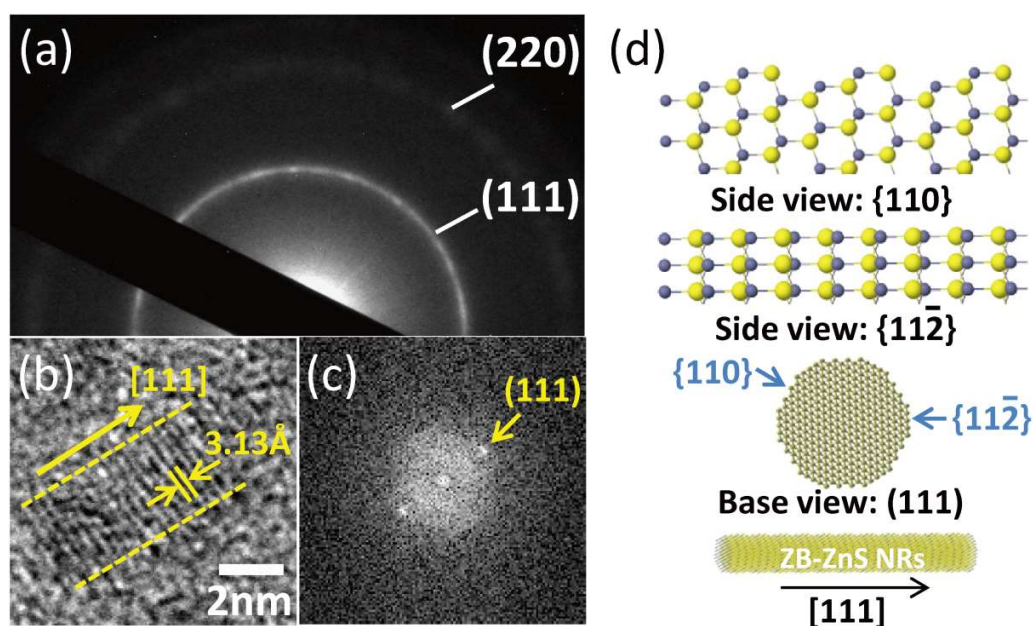
Figure 2-14. Structural characterization of ZnS NRs. (a) SAED pattern, (b) HRTEM image, and (c) FFT pattern of ZnS NRs synthesized with a Zn:S molar ratio of 1:27 in the synthesis. (d) Schematic illustration of the crystallographic nature of the ZnS NRs. Gray: Zn atoms; yellow: S atoms.

Element	Mass%	Atom%
S K	34.00	51.30
Zn K	66.00	48.70
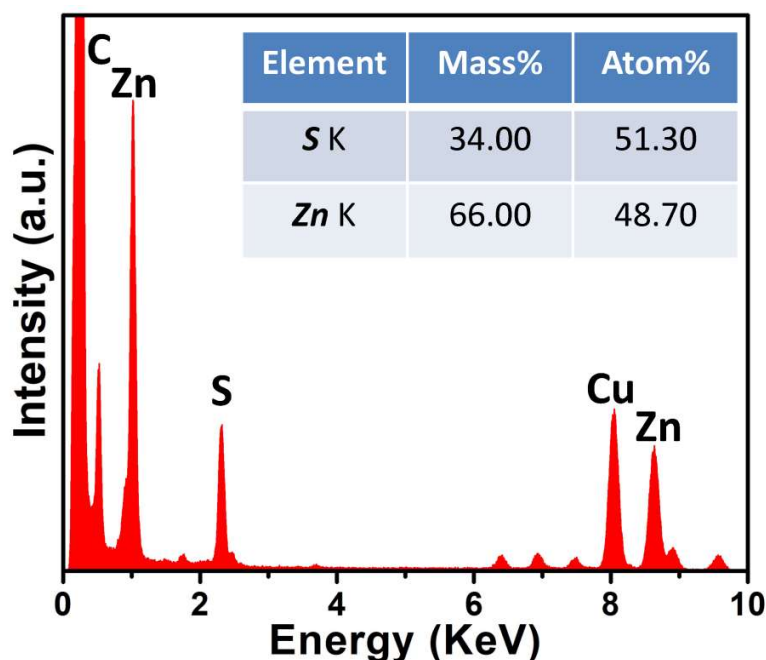
Figure 2-15. Component characterization of ZnS NRs. EDX spectrum of ZnS NRs synthesized with a Zn:S molar ratio of 1:27 in the synthesis.

The optical properties of ZnS NRs were characterized by UV−vis absorbance and PL spectra. The absorption spectrum (see Figure 2-16a, black curve) shows a continuum-like absorption ranging from the blue to the ultraviolet region. A shoulder absorption peak appears at 305 nm in the spectrum, which is attributed to the BE absorption onset. The band gap value (E_g) of the NRs, as estimated by the Tauc linearization, is ~3.87 eV (see Figure 2-16b) slightly blue-shifted by 0.15 eV compared to the bulk ZB-ZnS band gap (3.72 eV).[111, 117] This small blue-shift in the optical band gap implies a weak quantum confinement effect, which is in agreement with recent *ab initio* simulations of ZnS NRs.[118] The PL spectrum (see Figure 2-16a, red curve) exhibits a broad and asymmetric emission band consisting of peaks at 335 and 359 nm and weak shoulders at 395 and 468 nm, respectively. These peaks can be ascribed to the BE emission (335 nm, 3.7 eV), the exciton emissions at interstitial S (359 nm, 3.45 eV) and Zn (395 nm, 3.14 eV), and the dangling S bonds at the interface of ZnS (468 nm, 2.65 eV).[25, 119] In the current case, the well-known deep-trap emission around 450 nm (2.76 eV) generated from surface sulfur

vacancies is not observed,[25, 120] which can be explained by the excess sulfur in the rods as demonstrated by the EDX analysis (see Figure 2-15).
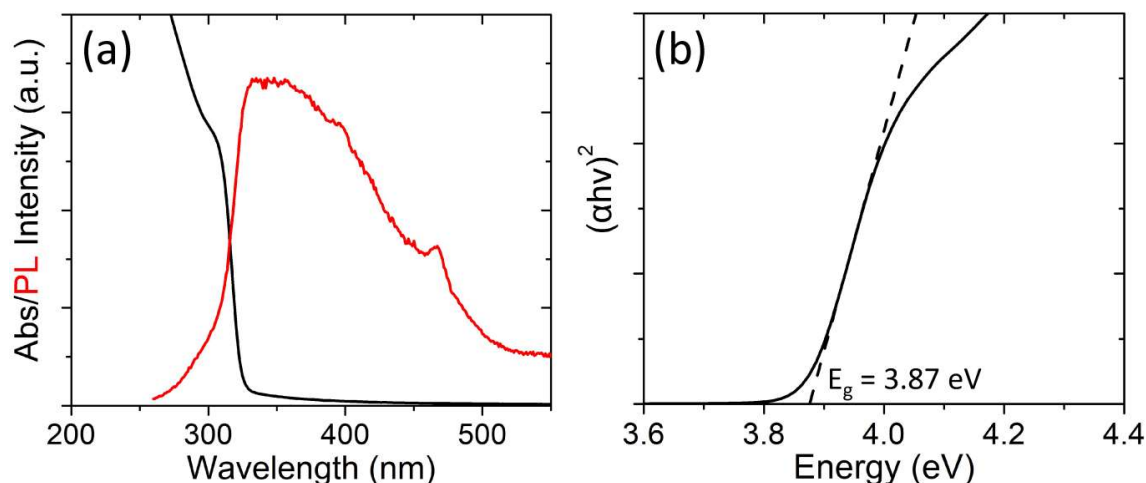
Figure 2-16. Optical characterization of ZnS NRs. (a) UV−vis absorbance (black) and PL (red) spectra of ZnS NRs synthesized with a Zn:S molar ratio of 1:27 in the synthesis. (b) $(\alpha h v)^2$ vs photon energy representation of the absorbance spectra for ZnS NRs. The band gap (E_g) of ZnS NRs is analyzed from the UV−vis absorbance spectra by calculating the absorption coefficient (α). E_g is calculated by using the relation for direct band gap semiconductors: $(\alpha h v)^2 = E_g - hv$.

The sulfur-dependent syntheses show that the shape control of ZnS NCs can be realized simply by varying the amount of sulfur. Recently, Peng and co-workers showed that the shape-evolution was correlated with the monomer concentration.[40-41, 121] For a given solution system, a high monomer concentration can support the growth of NCs in 1D growth stage, which generates rod-shaped NCs. In contrast, the dot-shaped NCs are preferentially formed due to the 3D growth stage at a low monomer concentration. In our case, it is clearly observed that the shape of ZnS NCs changed from dots to rods when the amount of sulfur was increased from 0.15 to 8.1 mmol, which is in line with Peng's growth mode. Furthermore, both the HRTEM image (see Figure 2-14b) and FFT pattern (see Figure 2-14c) confirm the 1D growth stage. Thus, the formation of the ZnS NRs is attributed to the effect of the high monomer concentrations.

2.3 Conclusions

In this work, a relatively simple, robust and effective method was developed for the synthesis of colloidal atomically precise ZnS NPLs. The resulting ZnS NPLs with well-defined structures exhibit narrow excitonic emission that has not been observed in previous reports. The observed optical features such as a considerable Stokes shift and several excitonic peaks in the absorption spectrum were confirmed by *ab initio* based calculations. It reveals that the observed absorption and emission bands arise from electronic interband transitions ($h_{0,1,2}-e_0$, h_4-e_1, h_1-e_3, h_5-e_2), and the splitting of hh-, lh-, and so-sublevels contributes merely to the broadening of excitonic transitions observed at room temperature. Moreover, a precise shape/phase control in ZnS NCs was achieved at a relatively low temperature (150 °C). By increasing the amount of sulfur, the shape was tuned from NPLs to NRs and the phase was transformed from WZ to ZB, which is confirmed by TEM, XRD, SAED, HRTEM, and FFT. The shape/phase transformation can be attributed to changes in nucleation and growth of NCs induced by different reactant concentrations. A phase switch of NPLs from WZ to ZB by tuning of the synthetic parameters (sulfur amount, volume ratio between OAm and OTA, reaction temperature, and reaction time) was unrealized revealing strong linking of the shape and crystal phase of the ZnS NCs. The evolution of the shape and phase shown in this chapter endows the nanomaterials with tunable optoelectronic properties, making them potentially attractive for optoelectronic and catalytic applications.

2.4 Experimental Section

2.4.1 Chemicals

Zinc chloride (97+%), octylamine (OTA, 99+%) and methanol (99.8%) were purchased from Acros. Sulfur powder (99.998%) and oleylamine (OAm, 70%) were ordered from Sigma-Aldrich. Toluene (99.5%), isopropanol (99.7%), and hexane (95%) were purchased from VWR. Acetone (99%) was purchased from Th. Geyer. Chloroform-d ($CDCl_3$, 99.80%) was ordered from Euriso-Top. Tetramethylsilane (TMS, 100%) was purchased from Deutero. All chemicals were used without further purification.

2.4 Experimental Section

2.4.2 Synthesis of ZnS Nanoplatelets

Standard Synthetic Procedure for ZnS NPLs. In a typical synthesis, 0.15 mmol (20.4 mg) of $ZnCl_2$ and 0.45 mmol (14.4 mg) of sulfur powder were dissolved in a mixture of 5 mL OTA and 10 mL OAm in a round-bottom three-necked flask (25 mL) equipped with a septum and a thermocouple in a glass mantle. The mixed solution was purged with nitrogen at 100 °C for 30 min under vigorous stirring. Then the reaction solution was heated to 150 °C and maintained for 6 h at this temperature with magnetically stirring under nitrogen atmosphere. After the reaction, the solution was cooled down naturally to room temperature by removing the heating mantle. The resulting NCs were purified by precipitation with a mixture of acetone/isopropanol (1 : 1 vv), centrifugation, removal of the supernatant, and re-suspension in hexane or toluene for further characterization.

Synthesis of a mixture of ZnS NPLs and NRs. The synthetic procedure was the same as that for ZnS NPLs, except that the amounts of sulfur powder in each experiment were 0.9, 1.35, and 2.70 mmol, respectively.

Synthesis of ZnS NRs. The synthetic procedure was the same as that for ZnS NPLs, except that the amounts of sulfur powder in each experiment were 4.05 and 8.1 mmol, respectively.

2.4.3 Preparation of the Soft Template

Preparation of the [$ZnCl_2$ (OTA, OAm)$_x$] soft template. The synthetic procedure was similar to that for ZnS NPLs, except that 0.15 mmol of $ZnCl_2$ without sulfur powder was added to a mixture of 5 mL OTA and 10 mL OAm. After the reaction, the resulting products were purified by precipitation with acetone, centrifugation, removal of the supernatant, and re-suspension in hexane for further characterization. For the ^{1}H NMR characterization, the samples were re-dispersed in $CDCl_3$.

2.4 Experimental Section

2.4.4 Characterizations and Simulations

TEM and SAED. TEM images and SAED patterns were performed on a JEOL Jem-1011 microscope at an acceleration voltage of 100 kV. Samples for the TEM and SAED analyses were prepared by drop-casting 10 μL of the dilute NC dispersion onto carbon-coated copper grids.

HRTEM and EDXS. HRTEM images and EDX spectra were obtained with a Philips CM 300 UT microscope operated at an acceleration voltage of 200 kV.

XRD. XRD measurements were performed with a Philips X'Pert PRO MPD diffractometer with monochromatic X-Ray radiation from a copper anode with a wavelength of 0.154 nm (CuKα). Samples for the XRD analysis were prepared by drop-casting a few μL of the concentrated NC solution onto silicon wafer substrates with subsequent solvent evaporation.

UV−vis absorbance and PL spectra. UV−vis absorbance and PL spectra were obtained with a PerkinElmer Lambda 25 two-beam spectrometer and a Horiba Fluoromax-4 spectrometer, respectively. Samples were prepared by adding a few μL of the NC solution into 3 mL hexane in quartz vessels with an optical path length of 10 mm.

^{1}H NMR. ^{1}H NMR spectra were recorded on a Bruker AVANCE 400 MHz Spectrometer (AV4002), and referenced to TMS as the internal standard.

***ab initio* simulations.** The simulations were performed in cooperation with the group of *Prof. Gabriel Bester* (University of Hamburg) (contributions from *Dr. Anastasia Karpulevich* and *Dr. Abderrezak Torche*). The DFT-LDA based atomic effective potentials[106] with non-local beta-correction,[122] spin-orbit coupling,[108] and pseudo hydrogen passivation of the surface[107] were used. Absorption spectra were modeled by calculations of the dipole transitions matrix elements within independent particle approximation.[123] Temperature-dependent broadening of the dipole transitions was implemented according to a previous work reported by Sun and co-workers.[124]

CHAPTER 3

Doping of ZnS Nanoplatelets with Mn²⁺ Ions

3.1 Introduction

3.1.1 Background

Since the first milestone in the preparation of Mn^{2+}-doped ZnS (ZnS:Mn) QDs,[125] doping of ZnS NCs with Mn^{2+} ions has been extensively explored due to advantages of low toxicity and high thermal and environmental stability. Besides, the absorption of ZnS NCs is limited to the UV-blue range. Doping ZnS with Mn^{2+} ions can lead to a large red-shift of emission with respect to the ZnS absorption, which can effectively avoid self-absorption. Recently, numerous approaches have been developed to fabricate ZnS:Mn QDs.[76, 126-127] Apart from 0D ZnS QDs, Liu and co-workers doped 1D ZnS QRs with Mn^{2+} ions, and the resulting Mn^{2+}-doped QRs had a high PLQY of up to 45%.[128] Despite the syntheses of the ZnS:Mn dots, rods, and wires have been reported, the literature related to the ZnS:Mn NPLs is scarce. As far as I know, only one work showed the preparation of colloidal ZnS:Mn NPLs by a post-synthesis treatment so far,[89] but the as-synthesized ZnS:Mn NPLs were quite unstable at room temperature. The Mn^{2+} ions are ejected immediately from the ZnS NPLs when the temperature is below 180 °C. This research reflects that the synthesis of ZnS:Mn NPLs still remains a big challenge.

3.1.2 Motivation

In Chapter 2, ultrathin colloidal ZnS NPLs were successfully synthesized and display the advantage of superior excitonic absorption and fluorescence properties in the UV range. To investigate the excitonic features further, doping the ZnS NPLs with Mn^{2+} ions was taken into account.

The ZnS NPLs represent an attractive choice as a matrix for Mn^{2+} ions. First of all, zinc and manganese ions in tetrahedral coordination have similar ionic radii (74 vs 80 pm),[129-130] which is beneficial for insertion of Mn^{2+} ions into a Zn-containing matrix. Because of the strong quantum confinement in NPLs, the matrix absorption and Mn^{2+} emission can be separated in the spectrum by more than 2 eV. Moreover, it is found that the WZ phase of ZnS shows enhanced spontaneous polarization being able potentially to influence the dopant PL.[96] Altogether, this creates a perspective nonexplored platform for low-toxic energy conversion units with no self-absorption and dramatically enhanced

oscillator strength. However, as mentioned above, the synthetic methods for stable colloidal ZnS:Mn NPLs are lacking, which promotes us to explore an effective and "green" synthetic route. Besides, doping the ZnS NPLs with Mn^{2+} ions can open a new avenue for ZnS NPLs. The investigation of the relationship between excitons of ZnS and Mn^{2+} ions is helpful to understand the relaxation mechanisms for the excited charge carriers in NPLs.

3.2 Results and Discussion

3.2.1 Structural Characterizations of ZnS:Mn Nanoplatelets

Colloidal ZnS:Mn NPLs were synthesized by adapting the soft-template method. This method is similar to that for the synthesis of ZnS NPLs except that $Mn(OAc)_2$ was added. The experimental parameters such as temperature, reaction time, and molar ratio of Zn and S have been optimized to obtain the most stable and homogeneous product in the synthesis of ZnS NPLs. Thus, the parametric window for the doped NPLs was very narrow. In a typical synthesis, the nominal Mn:Zn:S molar ratio was set as x:1:3, where x can be varied between approximately 0.03% and 16%. After reaction, the resulting product was purified by precipitation with acetone/isopropanol and re-dispersion in toluene or hexane for further characterization.

An exemplary TEM image (see Figure 3-1a) of the as-synthesized ZnS:Mn (x = 4%) nanostructures shows that they have a platelet-like shape similar to the undoped NPLs (see Figure 3-1b). The HRTEM image (see Figure 3-1c) and FFT pattern (see Figure 3-1d) reveal that the doped NPLs are well crystallized. The interplanar spacings shown in Figure 3-1c were measured as 3.09 and 3.27 Å, corresponding to the (0001) and (10-10) planes of WZ-ZnS, respectively. The crystal structure of the NPLs with and without Mn^{2+} doping was compared using XRD. It is found (see Figure 3-1e) that the doped NPLs have the same phase (WZ-ZnS, ICPDS 00-080-0007) as that of the undoped NPLs, suggesting that doping has no obvious influence on the crystal structure of the NPLs.
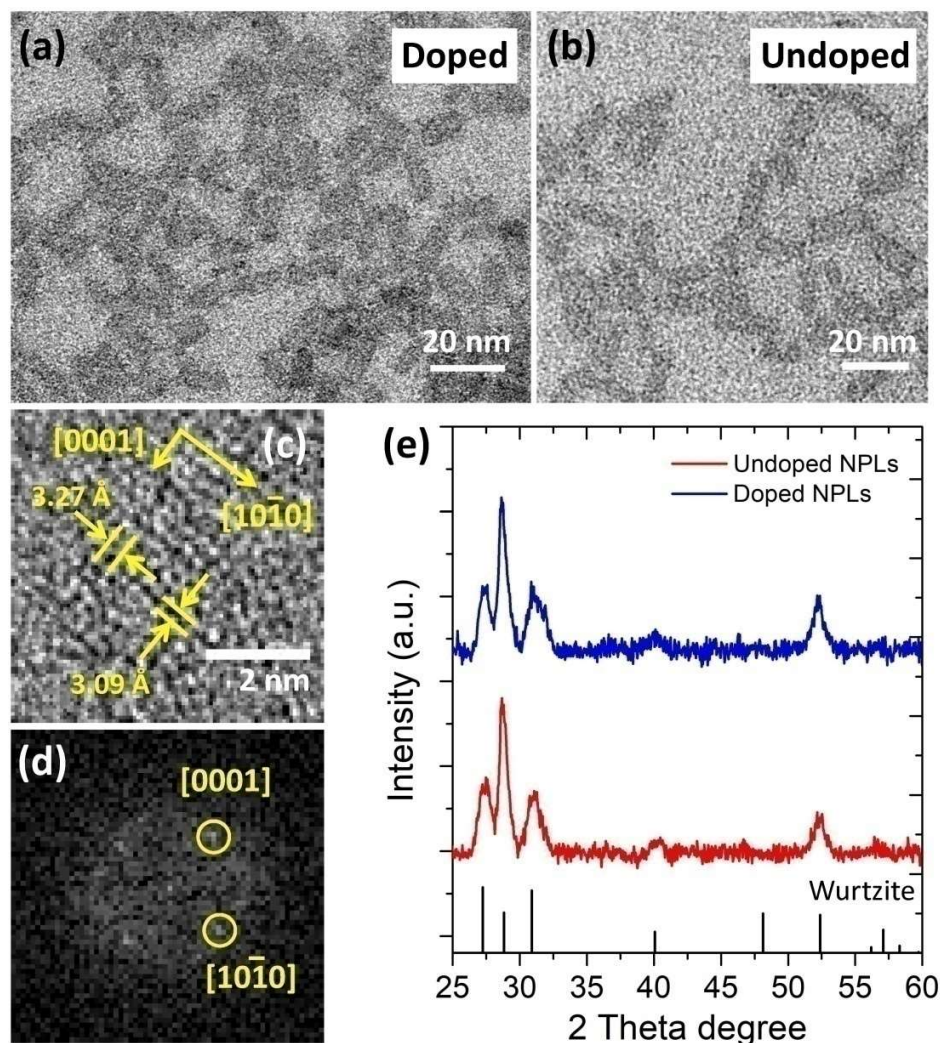
Figure 3-1. Shape and phase characterization of the doped and undoped NPLs. TEM images of (a) doped and (b) undoped NPLs synthesized with an Mn:Zn:S ratio of 0.04:1:3 and 0:1:3 in the synthesis, respectively. (c) HRTEM image and (d) the corresponding FFT pattern of an individual doped NPL. (e) XRD patterns of the undoped (red) and doped (blue) NPLs. Vertical lines indicate the bulk WZ-ZnS pattern (ICDD card no. 00-080-0007). The XRD patterns are vertically shifted for clarity.

The EDX spectrum (see Figure 3-2) confirms the presence of an Mn component in the doped NPLs, showing the atomic ratio of Mn:Zn:S to be 0.02:1:1.1, different than the ratio of 0.04:1:3 as set for the precursors. To accurately determine the content of Mn in the NPLs, inductively coupled plasma optical emission spectroscopy (ICP-OES) was

performed and the result will be discussed below. Additionally, the atomic ratio of Zn:S is found to be 1:1.1, which is close to the stoichiometric ratio of ZnS compound, indicating a slight zinc deficiency.

Element	Mass %	Atom%
Zn	64.17	47.09
S	34.71	51.93
Mn	1.13	0.98
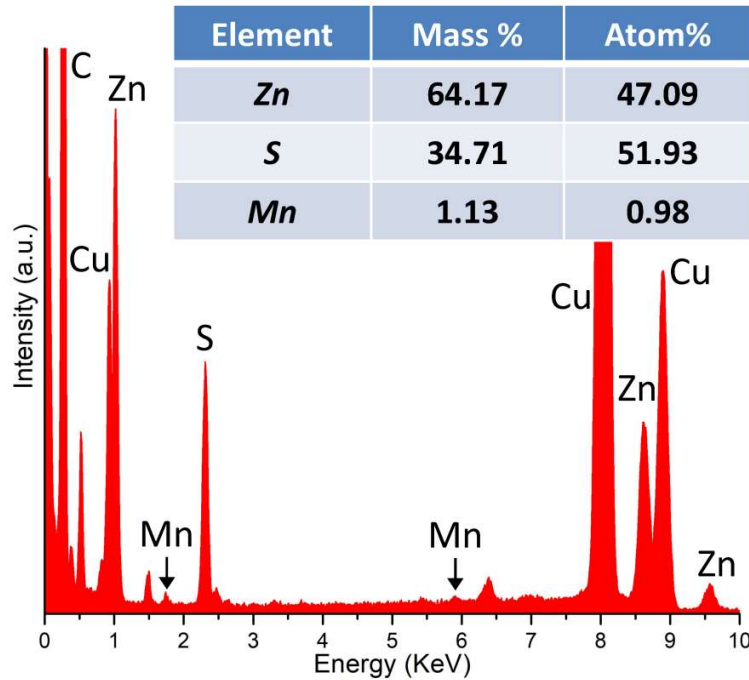
Figure 3-2. Component characterization of ZnS:Mn NPLs. EDX spectrum of ZnS:Mn NPLs synthesized with a nominal Mn:Zn:S ratio of 0.04:1:3. The atomic ratio of the Mn:Zn:S is listed in the tables.

3.2.2 Optical Properties of ZnS:Mn Nanoplatelets

The optical properties of doped NPLs (x = 4%) were characterized by steady-state UV−vis absorbance and PL spectroscopy. The absorbance spectra (see Figure 3-3, left) show that the doped and undoped samples possess nearly identical spectral features, manifesting that the electronic structure of the host was unaltered when Mn^{2+} ions were added. A narrow excitonic absorption peak centered at 283 nm (4.38 eV) is clearly observed, reflecting a high uniformity in thickness (5 MLs thick, 1.8 nm) of the doped NPLs.[131] The PL spectra of the samples with and without doping were recorded with an excitation wavelength of 260 nm. Note that the prominent peak at 520 nm in the spectra

is not a PL signal, but a signal originating from the second diffraction order of the excitation light. A smaller peak around 560 nm can be assigned to the second diffraction order of the Raman signal from the solvent (hexane).[128] The PL spectrum of doped NPLs (Figure 3-3, right) displays an emission band centered at 601 nm (2.06 eV) with a FWHM of ~237 meV, which is not observed in the PL spectrum of undoped NPLs. This band can be assigned to the $^4T_1-^6A_1$ transitions of Mn^{2+} ions.[76-77] A typical orange emission of the ZnS:Mn sample is observed by eye, as proven by a photograph of a NPL-coated cover slide under UV illumination (inset in Figure 3-3), which is a clear indication of the successful doping of the ZnS crystal lattice with Mn^{2+} ions.
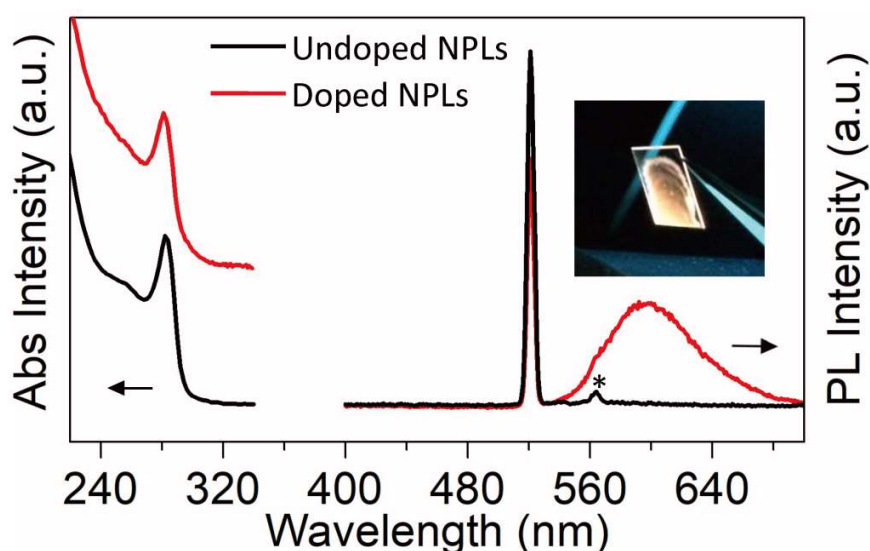
Figure 3-3. Optical characterization of doped and undoped NPLs. Left: UV−vis absorbance spectra of undoped (black) and doped (red) NPLs. The spectra are vertically shifted for clarity. Right: The corresponding steady-state PL spectra ($\lambda_{exc} = 260$ nm). The inset shows a photograph of the doped NPL dispersion under UV illumination. The scattered light of the lamp (narrow peaks at 520 nm) and the solvent (hexane) Raman peaks (marked with an asterisk) are also detected.

The PL excitation (PLE) spectrum of doped NPLs was recorded for which the detection wavelength was set to 600 nm. The intense feature at 300 nm (see Figure 3-4a, red solid) is again a signal from the second diffraction order of the spectrometer grating.

3.2 Results and Discussion

It is found that the PLE spectrum of the Mn^{2+} emission resembles the absorbance spectrum (see Figure 3-4a, black dashed), indicating that upon ZnS excitation an energy transfer from the host material to the dopant occurs before the Mn^{2+} PL is emitted. This finding of the energy transfer is further supported by comparison of the PL spectra of undoped and doped NPLs (see Figure 3-4b). Here, the excitation wavelength was set to 280 nm for two purposes. First, this excitation wavelength is in resonance with the exciton absorption, which significantly increases the PL intensity of the sample.
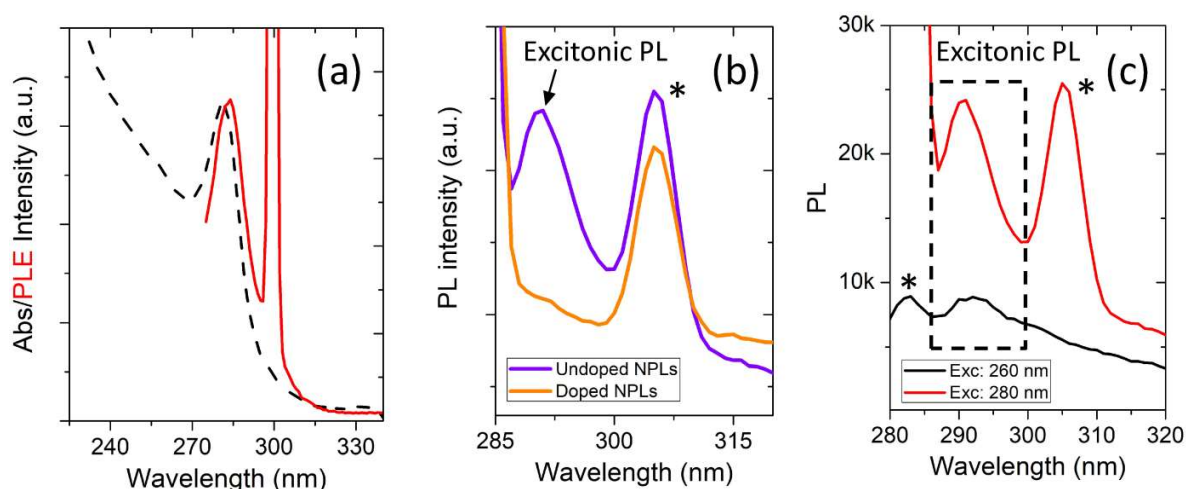
Figure 3-4. Optical characterization of doped and undoped NPLs. (a) UV−vis absorbance (black dashed) and PLE (red solid) spectra of doped NPLs monitored at 600 nm. (b) PL spectra of undoped (purple) and doped (orange) NPLs (λ_{exc} = 280 nm). (c) PL spectra of doped NPLs with different excitation wavelengths. The scattered light of the lamp (the narrow peak at 300 nm in panel b) and the solvent (hexane) Raman peaks (marked with an asterisk) are also detected.

As shown in Figure 3-4c, the maximum of the PL peak increases by ~2.5 times when the excitation wavelength is changed from 260 to 280 nm. Second, the spectral overlap between the exciton emission of the ZnS NPLs and the Raman peak of the solvent (hexane) is minimized. Without Mn^{2+} doping, the spectrum of the sample (see Figure 3-4b, purple) shows a discernible emission band centered at 292 nm, which originates from the exciton recombination of ZnS NPLs.[131] With Mn^{2+} doping, the exciton emission disappears (see Figure 3-4b, orange), suggesting a strong coupling of excitons and Mn^{2+}

58

ions in the NPLs. The overall photophysical process between the host and dopants is summarized in Figure 3-5.
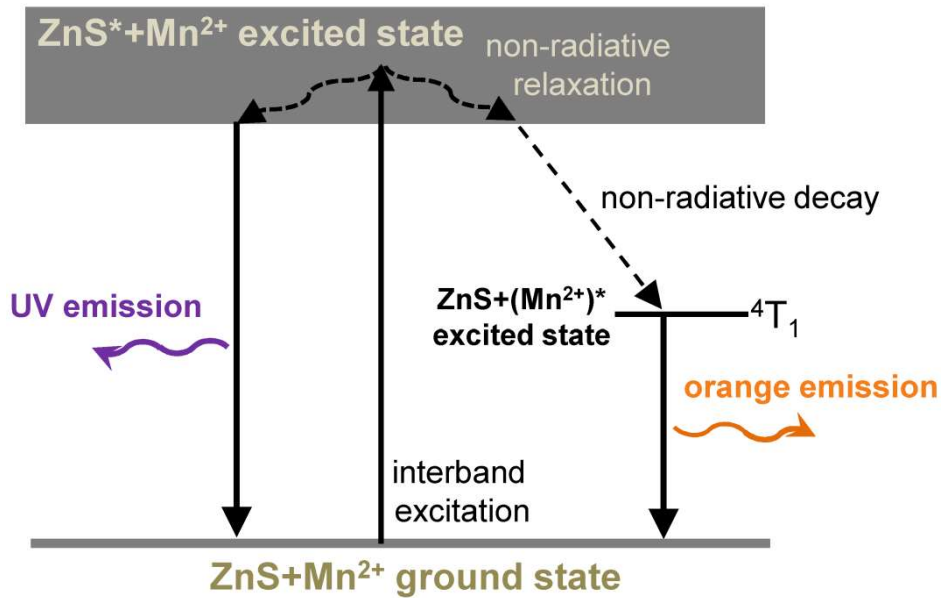
Figure 3-5. Schematic illustration of the photophysical processes in ZnS:Mn NPLs.[127, 132]

3.2.3 Influence of the Mn^{2+} Concentration on the Optical Properties of ZnS:Mn Nanoplatelets

In this section, the effect of Mn^{2+} concentrations on the optical properties of ZnS:Mn NPLs was studied. A set of samples with a nominal Mn:Zn atomic ratio of the precursors varying from approximately 0.03% to 16% were synthesized. The XRD patterns (see Figure 3-6) show that the characteristic diffraction peaks of these samples correspond to the hexagonal WZ-ZnS structure (ICDD card no. 00−080−0007). As the doping level increases, no significant changes in the crystal structure are observed, which is very different from the results in previous reports.[133-135] The detailed discussion will be given after the presentation of detailed X-ray photoelectron spectroscopy (XPS) and ICP-OES results.
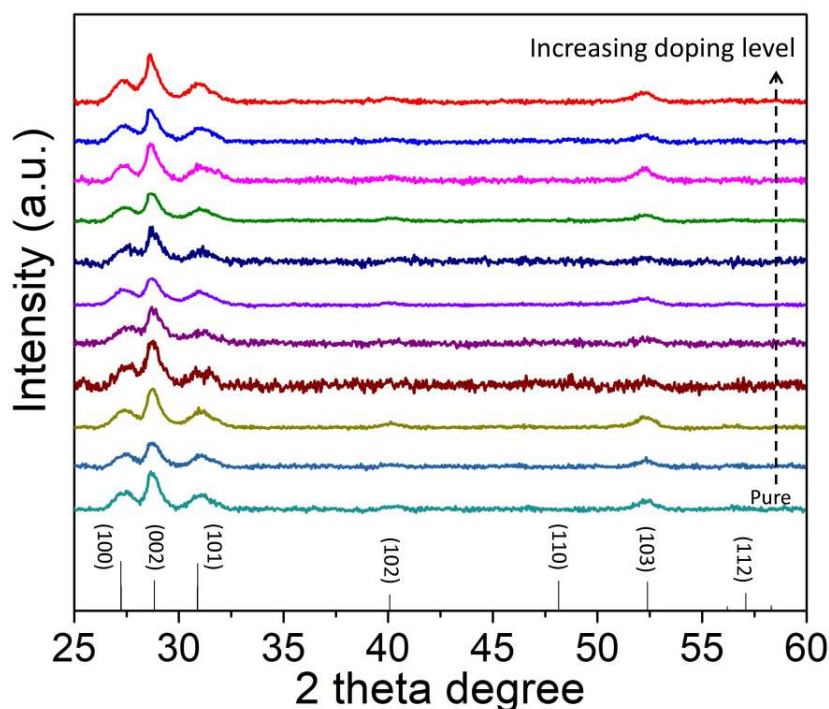
Figure 3-6. Influence of the Mn^{2+} concentration on the crystal structure of ZnS:Mn NPLs. XRD patterns for a set of samples with different doping levels. Vertical lines indicate bulk WZ-ZnS pattern (ICDD card no. 00−080−0007). The XRD patterns are vertically shifted for clarity.

To determine the actual Mn:Zn atomic ratios in the doped NPLs, ICP-OES was performed. The nominal Mn:Zn ratios used in the synthesis and the actual Mn:Zn ratios in the NPL samples were compared, which is summarized in Table 3-1. Notably, the actual Mn:Zn atomic ratio in the NPLs is generally lower than the nominal ratio in the reaction solution, indicating that Mn^{2+} ions are less active than Zn^{2+} ions during the synthesis. Additionally, it is found that the actual ratio is close to the nominal ratio at very low (0.03%) and very high (16%) doping levels, while the strongest deviations occur at medium doping levels. According to the average NPL dimensions of 15.8 and 6.4 nm in length and width, as measured from TEM images and 1.8 nm in thickness, the average number of Mn^{2+} ions per NPL can be estimated. For the set of samples, the range of 0.03−16.64% Mn:Zn ratios corresponds to 1.4−793 Mn atoms per NPL (see Table 3-1).

3.2 Results and Discussion

Table 3-1. Determination of the Mn^{2+} concentration in the ZnS:Mn NPLs. The nominal Mn:Zn atomic ratio used in the synthesis, the actual Mn:Zn atomic ratio in the NPL samples determined by ICP-OES, and the average number of Mn^{2+} ions per NPL determined via ICP-OES.

nominal Mn:Zn atomic ratio (%)	Mn:Zn atomic ratio determined by ICP-OES (%)	average number of Mn^{2+} ions per NPL
0.03	0.03	1.4
0.06	0.04	1.9
0.13	0.06	2.9
0.25	0.10	4.9
0.50	0.20	9.5
1	0.38	18
2	0.69	33
4	1.52	73
8	4.89	233
16	16.64	793

The optical properties of these samples were characterized using the steady-state UV−vis absorbance and PL spectroscopy. With increase in the Mn^{2+} doping level from 0.03% to 1.52% (corresponding to up to 73 Mn^{2+} ions per NPL), no other particular features in the absorbance spectra of doped NPLs occur as compared to the undoped NPLs (see Figure 3-7a, left). When the doping level exceeds 1.52%, the excitonic absorption peak at 283 nm broadens slightly (see Figure 3-7b), which could be a result of perturbation of Mn^{2+} ions to the electronic structure of ZnS.[136] The PL spectra of doped NPLs show a broad Mn emission peak with a nearly stable value for the FWHM of 0.24−0.29 eV. Looking closer at the emission spectra, a red-shift can be seen in the PL peak center with increasing doping level (see Figure 3-7c). This large shift ($\Delta\lambda = \sim 15$ nm) can be attributed to the $Mn^{2+}−Mn^{2+}$ interaction.[137-138]
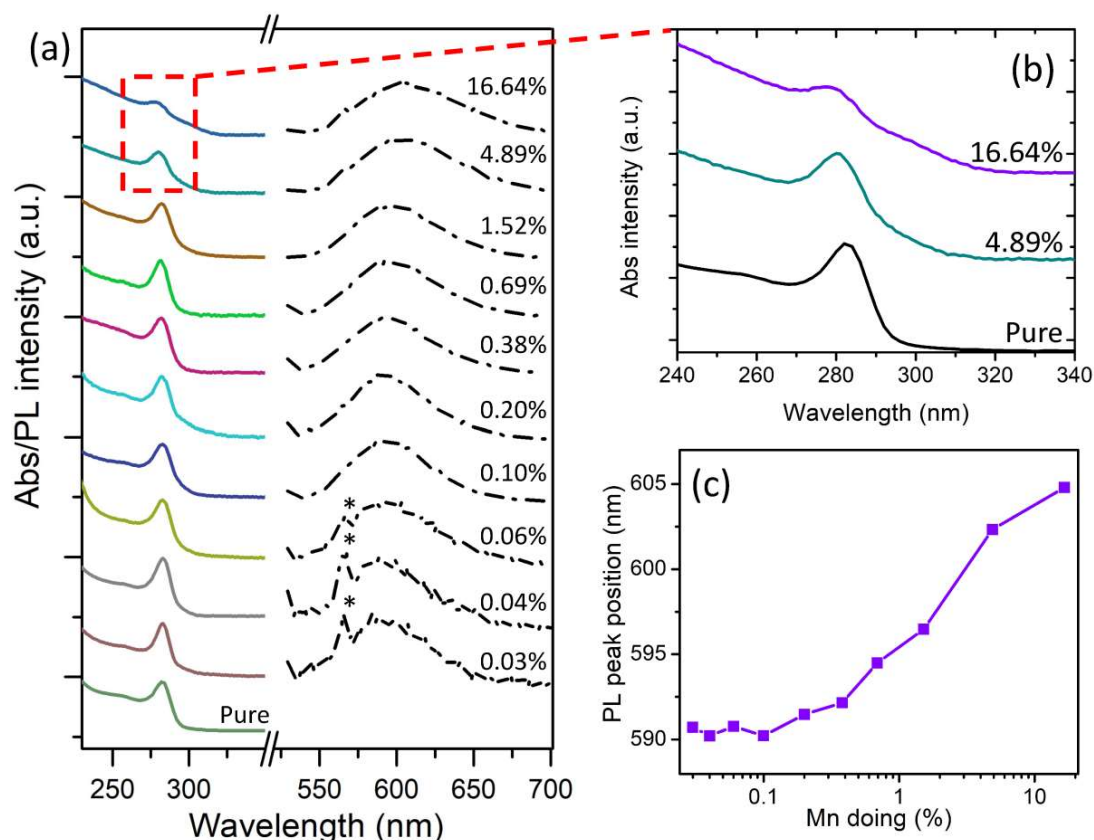
Figure 3-7. Influence of the Mn^{2+} concentration on the optical properties of ZnS:Mn NPLs. (a) Steady-state UV−vis absorbance and PL spectra of NPLs with increasing Mn^{2+} doping levels determined by ICP-OES (λ_{exc} = 260 nm). The solvent (hexane) Raman peaks (marked with an asterisk) are also shown. The spectra are vertically shifted for clarity. (b) Magnified view of the UV−vis absorbance spectra for doped NPLs. (c) Variation of the Mn^{2+} emission peak position against the doping level determined by ICP-OES.

Apart from the Mn^{2+} PL, the influence of Mn^{2+} concentrations on the exciton emission of ZnS was investigated. To directly compare the intensity of the exciton emission, the samples with the same NPL concentration (*i. e.* the same optical density at the maximum of the exciton absorption peak) were measured. The emission spectrum of undoped NPLs (see Figure 3-8a) exhibits the characteristic exciton emission around 292 nm. As the average number of Mn^{2+} ions per NPL increases, the intensity of the exciton emission decreases gradually and the peak is quenched when each NPL is doped with 73 Mn^{2+} ions on average. This result indicates that the competitive kinetics between excitons

and Mn^{2+} ions is dramatically affected by doping, which is further uncovered by comparing the intensity of the host and dopant emission. As shown in Figure 3-8b, the intensity ratio of the exciton and Mn^{2+} emission decreases from 0.27 to 0 when the doping level was increased from 0.03% to 16.64%.
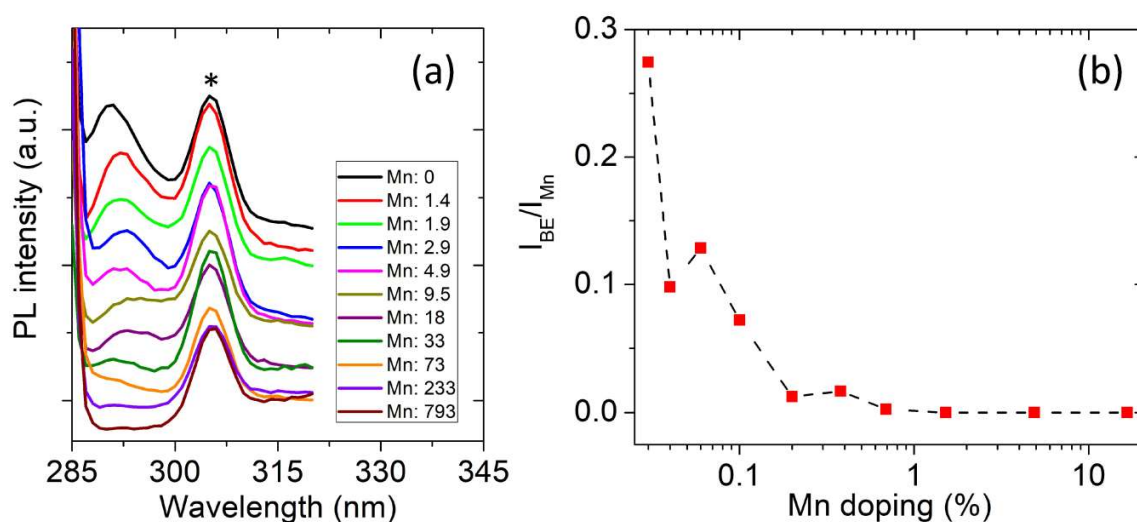
Figure 3-8. Influence of the Mn^{2+} concentration on the host and dopant emission. (a) PL spectra of ZnS:Mn NPLs with different Mn^{2+} doping levels. The spectra are vertically shifted for clarity. The solvent (hexane) Raman peaks (marked with an asterisk) are also shown. (b) Intensity ratio of the ZnS and Mn^{2+} emission as a function of the Mn^{2+} doping level.

3.2.4 Investigation of Mn^{2+} Distribution

In addition to the Mn^{2+} concentration, the Mn^{2+} distribution in the host can also influence the optical properties of ZnS:Mn NPLs. Many researches show that the emission of doped NCs can be tuned by controlling the dopant position.[81-82, 137] In the present ZnS:Mn system, electron paramagnetic resonance (EPR) spectroscopy was employed to investigate the exact location of Mn^{2+} ions in the ZnS NPLs. At a very low doping level (0.04%), some multiplet hyperfine splitting lines can be seen in the EPR spectrum (see Figure 3-9, black), revealing the existence of several Mn^{2+} species. Two sets of six-line signals of Mn^{2+} ions at $g = 2.004$ with resolved hyperfine structure ($A = 70$ and 92 G, zero-fine-splitting parameter $D = 410$ and 189 MHz, respectively) are

extracted from the EPR spectrum of the sample (0.04%). The one with higher degree of symmetry (A = 70 G) can be assigned to the tetrahedral symmetry of Mn^{2+} ions incorporated in the ZnS lattice,[76, 128, 136] and the other one with lower degree of symmetry (A = 92 G) is close to surface/edges or on the surface of NPLs.[139-140] Based on this result, it can be deduced that the Mn^{2+} ions were incorporated not only inside the NPLs but also on the surface of the NPLs during the synthesis. When the doping level increases, the contribution of hyperfine splitting signals diminishes gradually and they nearly disappear at a doping level of 4.89% (see Figure 3-9, blue), whereas a broad signal develops and becomes more and more apparent. This broad, smooth signal indicates the presence of magnetically interacting Mn^{2+} species and/or Mn^{2+} aggregations[141] at high doping levels.
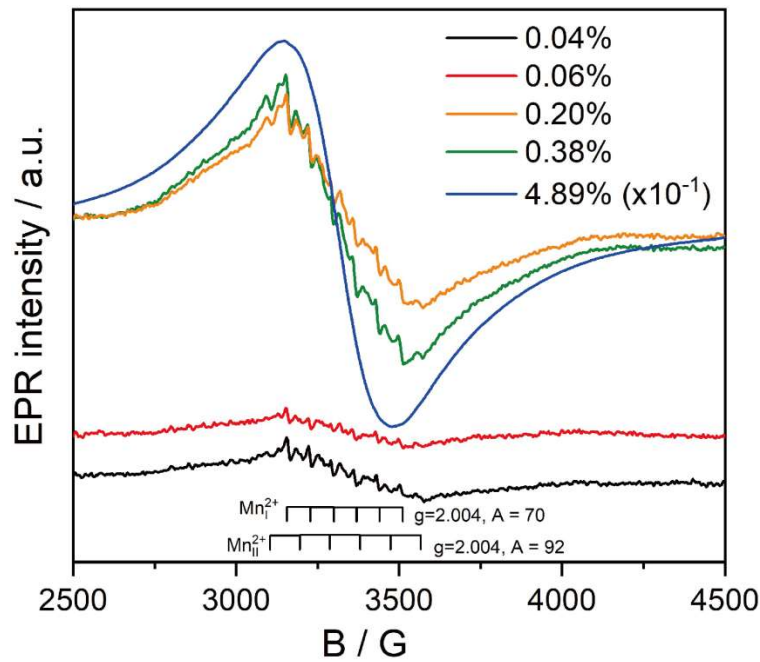
Figure 3-9. Determination of the local environment of Mn^{2+} ions in the ZnS:Mn NPLs. EPR spectra of ZnS:Mn NPLs with different Mn^{2+} doping levels determined by ICP-OES. Two sets of vertical lines indicate the sextet lines hyperfine splitting of 70 and 92 G.

To study the chemical state of the doped samples, XPS was conducted. The XPS survey spectrum of ZnS:Mn (1.52%, determined via ICP-OES) in Figure 3-10 shows that

Zn, S, Mn, O, C, and N elements can be detected in the doped NPL sample. The presence of C and N elements results from the OAm and OTA capping on the surface of NPLs.
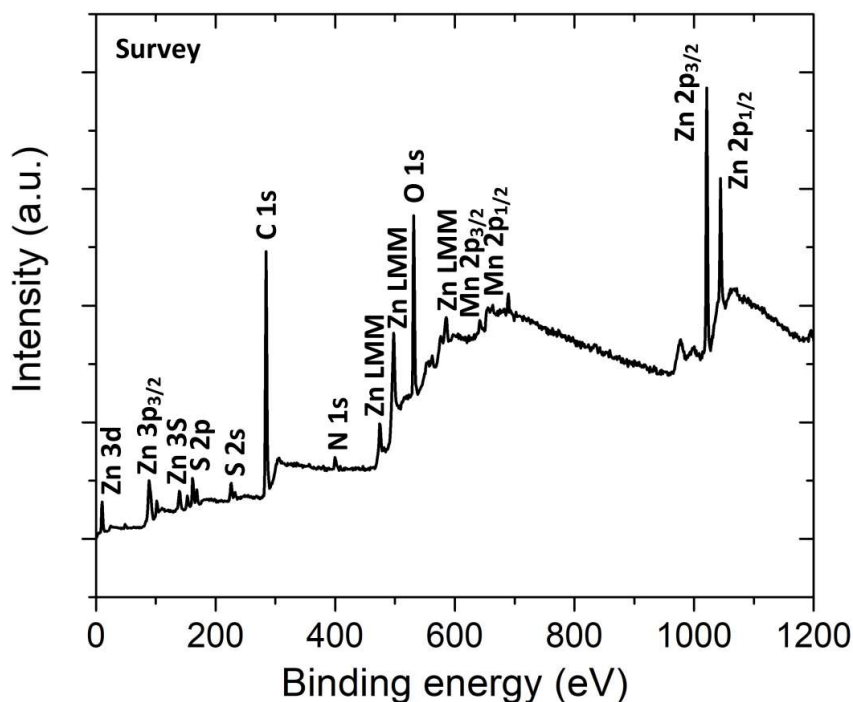
Figure 3-10. XPS survey spectrum of ZnS:Mn NPLs synthesized with a nominal Mn:Zn:S ratio of 0.04:1:3 in the synthesis.

The high-resolution Zn-2p, S-3p, Mn-2p$_{3/2}$, and O-1s core-level XPS spectra of ZnS:Mn NPLs are given in Figure 3-11 to determine the oxidation states of the constituent elements. The Zn-2p core level XPS spectrum (see Figure 3-11a) splits into Zn-2p$_{3/2}$ (1021.7 eV) and Zn-2p$_{1/2}$ (1044.8 eV) with a spin−orbit splitting energy of 23.1 eV, in line with that of Zn^{2+}.[142] The spectrum in the S-2p region (see Figure 3-11b) can be fitted by two species. The two strong peaks located at 161.8 eV (S-2p$_{3/2}$) and 163 eV (S-2p$_{1/2}$) confirms the exsitence of the bivalent S^{2-} state with its characteristic peak separation of 1.2 eV. The S-2p$_{3/2}$ signal centered at 161.8 eV is assigned to Zn−S bonds.[143] The signals of Mn-2p core level are very weak (see Figure 3-10), suggesting low content of Mn in the sample, which has been verified by the ICP-OES analysis. The XPS spectrum of Mn-2p$_{3/2}$ core level is asymmetric and multiplet peaks are detecable,

signifying a complicated electronic environment of Mn. The models reported by Biesinger et al.[144] was applied to fit the Mn-2p$_{3/2}$ spectrum.
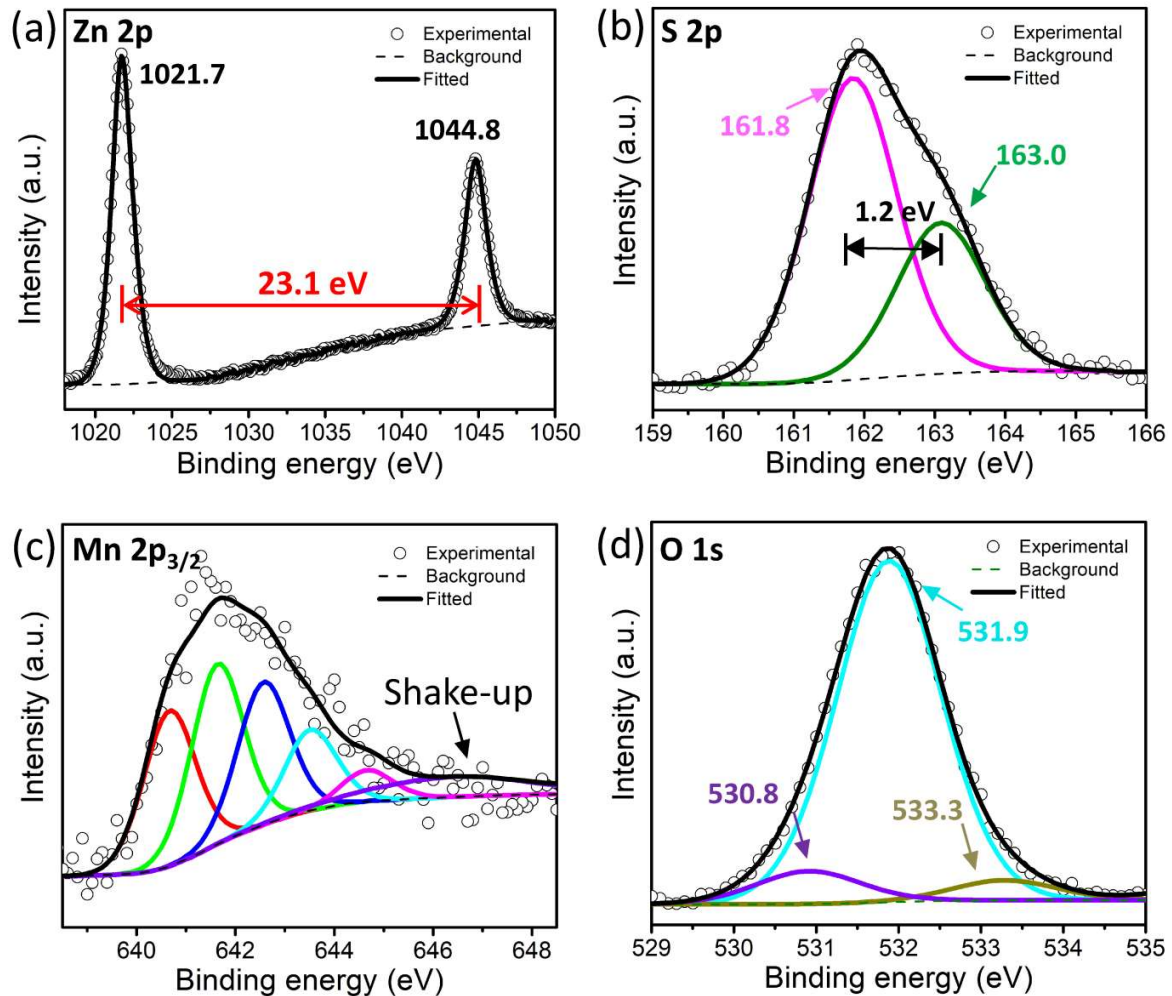
Figure 3-11. Core-level XPS spectra of (a) Zn-2p, (b) S-2p, (c) Mn-2p$_{3/2}$, and (d) O-1s regions of ZnS:Mn NPLs synthesized with a nominal Mn:Zn:S ratio of 0.04:1:3 in the synthesis.

As seen in Figure 3-11c, a set of peaks centered in the region of 640−645 eV can be assigned to Mn(II) (or Mn^{2+}),[144] indicating that Mn^{2+} ions are placed in slightly different electronic environment during doping. The different local environment of Mn^{2+} ions in NPLs is likely caused by their different degrees of coupling. Additionally, a small shake-up peak assigned to surface oxidation of Mn (Mn−O),[144] appears around 646 eV, which could be a sign of the presence of surface Mn. The spectrum in the O-1s region (see

Figure 3-11d) can be deconvoluted into three peaks located at 530.8, 531.9, and 533.3 eV. The former corresponds to oxygen in metal oxides (O^{2-})[145] and might be partially attributed to Mn^{2+} conjugated to O^{2-}. The latter two result from O^{2-} in the oxygen-deficient regions and the surface hydroxyl groups (O−H) adsorbed on the surfaces of the samples.[146] As mentioned above, the EPR results show that the doped NPL samples contain several Mn species: some incorporated into the ZnS lattice (inner Mn), and the other ones located presumably on the surface/edges of the NPLs (surface Mn), which is further supported by the XPS analyses.

From the XPS spectra, the atomic ratio of Mn:Zn can be obtained. A significant difference in the Mn content is found when the results of the ICP-OES and XPS analyses are compared. It appears (see Table 3-2) that the ratio of Mn:Zn measured by XPS is much higher than the one determined by ICP-OES in all samples.

Table 3-2. The nominal Mn:Zn atomic ratio used in the synthesis and the measured Mn:Zn atomic ratios determined via XPS and ICP-OES, respectively.

nominal Mn:Zn atomic ratio (%)	Mn:Zn atomic ratio measured by XPS (%)	Mn:Zn atomic ratio determined by ICP-OES (%)
0.5	1.87	0.20
1	1.94	0.38
2	3.03	0.69
4	11.63	1.52
8	12.50	4.89
16	19.67	16.64

The discrepancy is attributed to two factors. First, despite the ultrathin structure of the NPLs, the surface sensitivity of XPS might still contribute. Because ICP-OES probes the entire composition of the sample by dissolving the NPLs, XPS would then suggest that Mn^{2+} ions might occupy the surface more readily than the volume. Similar results were observed in a study of mercury-doped CdSe NPLs.[147] Second, the surface of the NPLs is

67

zinc-deficient jointly confirmed by EDX (see Figure 3-2) and the experiments of the Zn^{2+} treatment that will be discussed in the following section. Both two factors lead to an increase in the Mn:Zn ratio when XPS probes the NPLs. It is worth noting that the Mn content determined by XPS exceeds the nominal value added in the synthesis, revealing that Mn atoms readily occupy the surface of the NPLs during the doping process. This phenomenon can be well explained by the "self-purification" effect,[71, 79] which is usually observed in ultrasmall or ultrathin nanostructures. For the ultrathin ZnS:Mn NPLs, Mn^{2+} ions tend to be expelled and easily migrate to the surface due to the small interior volume of the NPLs.

The invariability in the XRD patterns of NPLs after strong Mn^{2+} doping is mentioned above (see Figure 3-6), which can be mainly ascribed to the "self-purification effect" along with close ionic radii of Zn^{2+} ions and Mn^{2+} ions (74 vs 80 pm).[129-130]
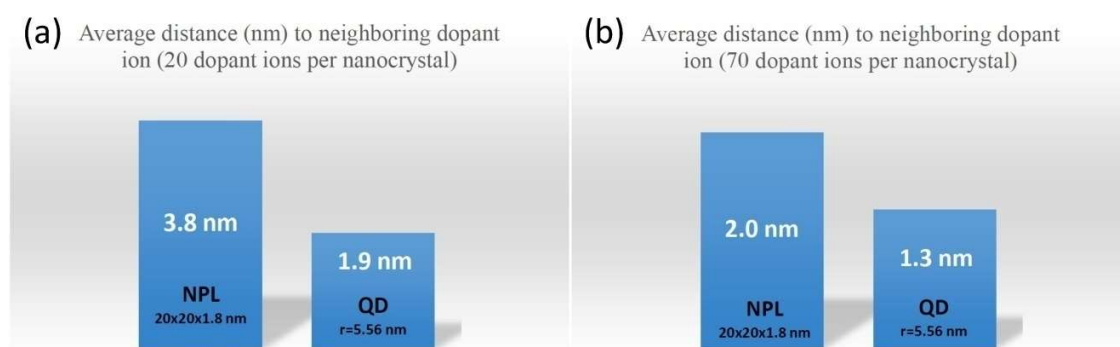
Figure 3-12. Diagrams visualizing a comparison of average distance between neighboring dopant ions inside a NPL and a QD of identical volume exemplarily for (a) 20 and (b) 70 dopant ions per NC.

Besides, in comparison to spherical particles the geometrical peculiarity of the 2D NPLs offers the following advantage: dopants (such as Mn^{2+} ions) induce less stress due to the smaller packing density. This conclusion can be supported by means of the Monte-Carlo approach (The Monte-Carlo calculations were contributed by *Dr. Rostyslav Lesyuk*). For the NPLs and QDs with the same volume and random dopant distribution, the average distance between dopants in NPLs is estimated to be 1.6 times larger than that in QDs at

the same doping level (see Figure 3-12). This also can contribute to the invariability of the XRD patterns.

3.2.5 Investigation of Mn^{2+} Photoluminescence Kinetics

To further study the Mn^{2+} emission kinetics, a series of samples with increasing Mn^{2+} doping concentration ranging in average from 1.4 to 793 dopants per NPL were measured with time-resolved PL (TRPL) at a low repetition rate (240 Hz) and a long integration time (1 hour). For all samples, the PL decay curves exhibit a multi-exponential decay behavior (see Figure 3-13), suggesting an inhomogeneous local environment of Mn^{2+} ions in the NPLs. This coincides with the previous EPR results.
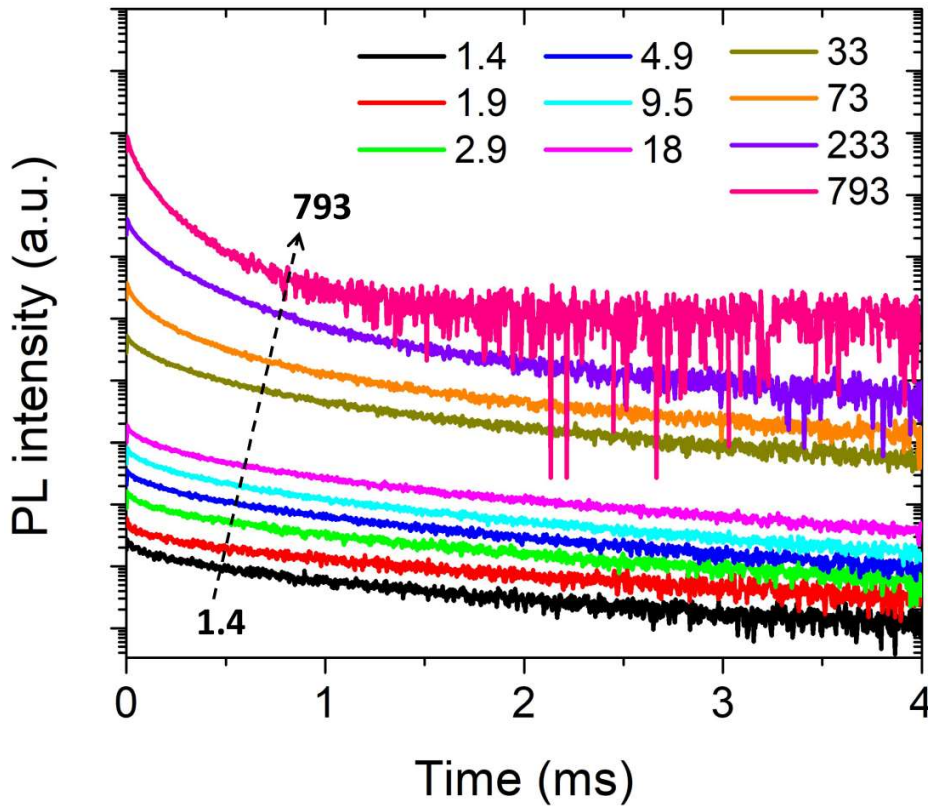
Figure 3-13. PL decay curves of ZnS:Mn NPLs with increasing Mn^{2+} doping levels detected at the maximum of the Mn^{2+} emission peak with an excitation wavelength of 285 nm. The spectra are vertically shifted for clarity.

These decay curves can be well fitted by a triexponential function[148]:

$$I(t) = y_0 + A_1\exp\left(-t/\tau_1\right) + A_2\exp\left(-t/\tau_2\right) + A_3\exp\left(-t/\tau_3\right), \quad (3\text{-}1)$$

where τ_1, τ_2, and τ_3 are the time constants and A_1, A_2, and A_3 are the normalized amplitudes of the components. The average lifetime (τ_{ave}) can be determined by the equation[148]:

$$\tau_{ave} = (A_1\tau_1^2 + A_2\tau_2^2 + A_3\tau_3^2)/(A_1\tau_1 + A_2\tau_2 + A_3\tau_3). \quad (3\text{-}2)$$

With increasing doping level, the average decay lifetime decreases (see Figure 3-14a), which can be assigned to the increasing $Mn^{2+}-Mn^{2+}$ coupling. The strong magnetic coupling between Mn^{2+} ions, evidenced by the previous EPR results, could partially lift the spin-forbidden $^4T_1-^6A_1$ $d-d$ transition, resulting in reduced PL decay lifetimes.[149] The development of the time constants of the three components is shown in Figure 3-14b.
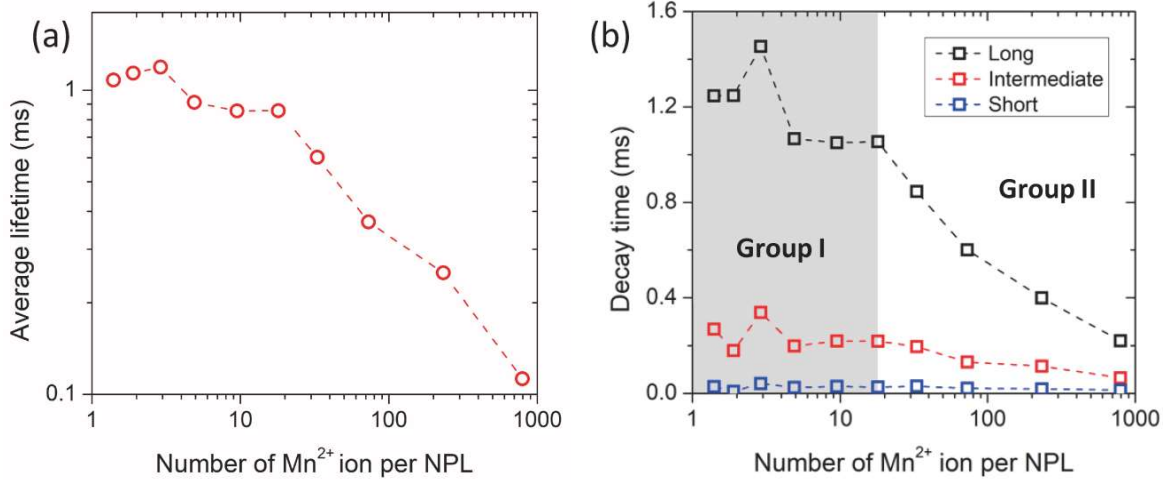
Figure 3-14. Plots of (a) the average lifetime of the Mn^{2+} emission and (b) the time constants of the three components as a function of the Mn^{2+} doping level.

The samples with the mean number of Mn^{2+} ions per NPL $\leqslant$ 18 are classified as "Group I" and the rest as "Group II". For the Group I, the decay time constants of the three components (long, intermediate, and short components) are found to be on the scale of 1−2 milliseconds, hundreds of microseconds, and tens of microseconds, respectively. As

the average number of Mn^{2+} ions per NPL increases from 1.4 to 18, the time constants of the intermediate and short components keep nearly constant, while the time constant of the long component decreases slightly. Looking at the Group II, the time constant of the short components is almost unchanged, whereas the time constants of the long and intermediate components decrease as the doping level increases. It is worth noting that the long component drops much faster than the intermediate component. When the doping level was further increased to the maximum (793 Mn^{2+} ions per NPL), the time constant of the long component reaches the same time scale as that of the intermediate component.

In order to investigate the microscopic origin of the three decay components, density functional theory (DFT) calculations were performed in cooperation with the group of *Prof. Gabriel Bester* (contributed by *Dr. Abderrazak Torche*). A slab containing 288 atoms with a thickness of 1.52 nm was constructed to simulate the experimentally synthesized ultrathin ZnS:Mn NPLs (~1.8 nm in thickness), because the thickness was limited by the consumable numerical algorithm. Since the Mn^{2+} $d-d$ transition is orbital- and spin- forbidden, spin polarization and spin-orbit coupling have to be considered in the ground state calculation in order to relax these selection rules and reveal a finite lifetime. Figure 3-15 shows the unit cell used to simulate the Mn^{2+}-doped slab (left panel) together with the resulting eigen-energies from the DFT calculations (middle panel) and a schematic of the energy levels in the area around the band gap (right panel). It is worth noting that the situation where the Mn^{2+} ions reside on the surface is more complex involving a large number of atoms for the passivation and could not be simulated within DFT. In Figure 3-15b the color bar denotes the d-character of the state (higher value means approaching the pure d-state). The half-filled and 10-fold degenerate d-states of the Mn^{2+} ion split in the ZnS environment because of the spin-orbit, spin polarization, and ligand field effects. The filled states reside near the VBM while the empty states reside near the CBM. Note that this splitting between filled and empty d-states which corresponds to the observed orange emission might be overestimated in the calculations because of the local density approximation (LDA) used in DFT, which is known to perform less well in the description of localized states. Nevertheless, for lifetime calculations DFT gives reliable results, which is consistent with the experiments as

71

discussed later. In the independent particle approximation (*i.e.* DFT level without excitonic effects) the lifetime of the optical transition can be estimated as[150]:

$$t \text{ (ns)} = \frac{1}{21.42 \, n \, E \, |M_{if}|^2}, \qquad (3\text{-}3)$$

where t is the lifetime in nanoseconds, E is the $d-d$ transition energy (in Hartree), n is the refractive index (~2.5 for ZnS), and M_{if} is the dipole matrix element between in the i and f states in atomic units. The situation where a Mn^{2+} ion substitutes a Zn^{2+} ion in the 288 atom unit cell as in Figure 3-15a corresponds to a doping of 0.6 % and an $Mn^{2+}-Mn^{2+}$ distance of 19.8 Å, for which the Mn^{2+} ions can be considered as non-interacting.
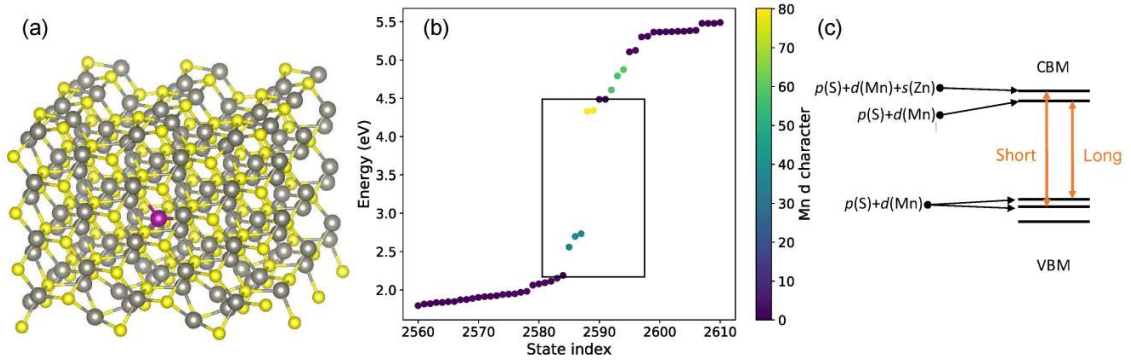
Figure 3-15. (a) The Mn (purple) doped ZnS unit cell (gray and yellow) with 288 atoms used to simulate the platelet. (b) Energy level of the doped slab in (a) at the DFT-LDA level. The color bar reflects the d-character of the Mn^{2+} states. (c) Schematics of the energy levels in (b) around the gap areas showing the origin (orbital hybridization) of the state involved the Mn^{2+} emission (long and short components).

At this doping level, lifetime calculations reveal (see Table 3-3) that the Mn^{2+} ion has two lifetime components, a longer one in the range of a few milliseconds (3.2 ms) and a shorter one in the range of hundreds of microseconds (370 μs). The origin of these two components is schematically depicted in Figure 3-15c as transitions between filled and empty d-states with different hybridization with the host material. The longer component occurs between $p(S) + d(Mn)$ orbits so it is an $p-d$-like transition whereas the shorter component occurs between an $p(S) + d(Mn)$ hybridized orbit and an $p(S) + d(Mn) + s(Zn)$

orbit so it is closer to an $s-p$-like transition. It is known that $s-p$ transitions are the strongest, thus, they should indeed reflect a faster decay.

To trace back the variation of the Mn^{2+} PL lifetime with doping within DFT, lifetime calculations with two Mn^{2+} ions inside the unit cell at different distances were performed. The results are depicted in Table 3-3. In all cases, two different decay components are revealed. The longer component lifetime decreases with decreasing distance between Mn^{2+} ions rather evenly from 3.2 to 1.27 ms. The reduction in the longer component lifetime is due to the increased hybridization between d-orbitals of the two Mn^{2+} ions, which lifts the selection rule for spin-forbidden transitions and makes the decay of the Mn^{2+} transition more probable and thus faster. Interestingly, the shorter component first does not change strongly, only for the smallest distance (3.82 Å) possible in the lattice between the Mn^{2+} ions, the lifetime drastically shortens by nearly one order of magnitude to 50 μs.

Table 3-3. DFT calculations of the Mn^{2+} (long and short components) PL lifetime as a function of the $Mn^{2+}-Mn^{2+}$ distance.

$Mn^{2+}-Mn^{2+}$ distance (Å)	long (ms)	short (μs)
19.80	3.20	370
14.74	3.16	220
12.03	2.08	270
9.48	2.01	330
6.21	1.55	330
3.82	1.27	**50**

Based on Table 3-3, Mn^{2+} ions with different $Mn^{2+}-Mn^{2+}$ distances in the ZnS NPLs can be classified into three scenarios: non-interacting isolated Mn^{2+} ions (distance ⩾

19.8 Å), weakly coupled Mn^{2+} ions (3.82 Å < distance < 19,8 Å), and strongly coupled Mn^{2+} ions (distance = 3.82 Å). Although the simulation results reveal that each Mn^{2+} species has only two decay components (long and short), a triexponential function is found to fit the PL decay curves well because the ensemble NPLs were measured. From the simulations, it is known that the longer component has the slowest decay time when the Mn^{2+} ions are non-interacting (distance $\geqslant$ 19.8 Å), and then it shortens by a factor of almost 3 as the $Mn^{2+}-Mn^{2+}$ distance decreases from 19.8 to 3.82 Å, which corresponds to the variation of the fitted long component lifetime (see Figure 3-14b, black dotted line). Thus, for the isolated Mn^{2+} ions, the "actual" time constant of the longer component can be estimated to be 1.2 ms by averaging the fitted long time constants of the Group I (shown in Figure 3-14b, black dotted line) since the local environment of the isolated Mn^{2+} ions in the Group I is stable. Based on simulations, it is also found that the shorter component of the strongly coupled Mn^{2+} ions (distance = 3.82 Å) has the fastest decay time in the range of tens of microseconds. This value matches well the fitted lifetime of the short component (see Figure 3-14b, blue dotted line). It is easy now to explain the observed doping independence of this component as shown in Figure 3-14b. In fact, since the shorter component with a time constant of tens of microseconds appears only when the Mn^{2+} ions are at the smallest distance, there is no way to change the lifetime of this transition by changing the doping level as this will not bring the ions closer together anymore. Similarly, the "actual" time constant of the shorter component for the strongly coupled Mn^{2+} ions is estimated to be 24 μs by averaging the fitted short time constants of the whole series of the samples (shown in Figure 3-14b, blue dotted line). To study the fraction of the three Mn^{2+} species as a function of the doping level, global fitting was performed with sharing the fixed time constants for the isolated Mn^{2+} ions (1.2 ms) and the strongly coupled Mn^{2+} ions (24 μs), while the time constant for the weakly coupled Mn^{2+} ions is not fixed because the distance between weakly coupled Mn^{2+} ions differs in samples with different doping levels. The results (see Figure 3-16) show that the fraction of the isolated Mn^{2+} ions changes slightly in the Group I, confirming the relatively stable environment of Mn^{2+} ions. However, apparent changes are observed in the Group II. The fraction of the isolated Mn^{2+} ions decreases sharply, which in turn leads to an increasing fraction of the other two Mn^{2+} ion species.
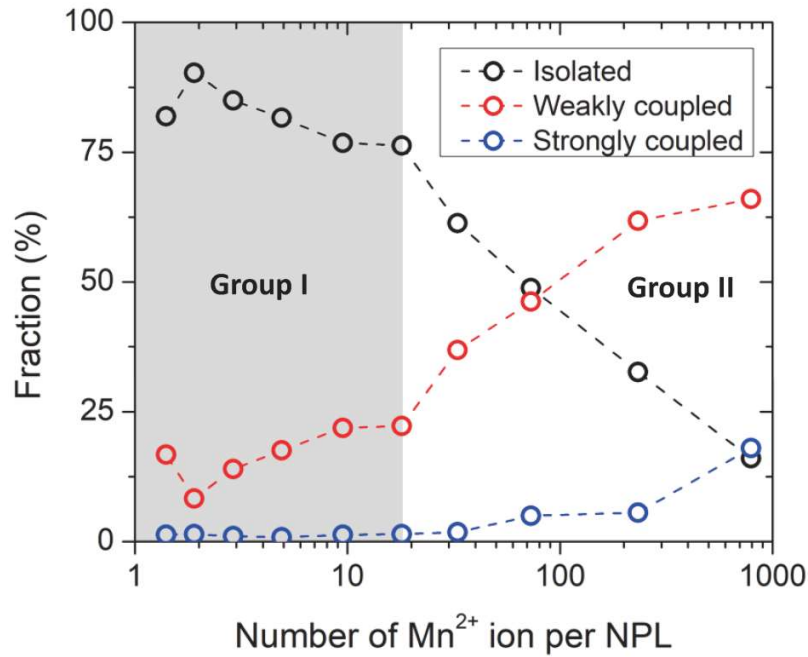
Figure 3-16. Plots of the fraction of the three Mn^{2+} species as a function of the doping level.

To disclose the relationship between the orange emission around 550−675 nm and Mn^{2+} species, the PL decay behavior of ZnS:Mn NPLs at variable emission wavelengths was investigated further. For that, a typical sample with 18 Mn^{2+} ions per NPL was measured. Figure 3-17a shows that the PL decay kinetics of the sample differ from one wavelength to another, revealing the heterogeneous character of the orange emission. The global fitting was performed again to fit these PL decay curves. It is found (see Figure 3-17b) that the fraction of the isolated Mn^{2+} ions decreases with increasing wavelength, while the coupled Mn^{2+} ions (weakly and strongly coupled Mn^{2+} ions) has a reverse variation trend. This suggests that the isolated Mn^{2+} ions preferentially emit at shorter wavelengths, whereas the coupled Mn^{2+} ions preferentially emit at longer wavelengths. The average lifetime of the Mn^{2+} emission decreases with an increase in the emission wavelength (see Figure 3-17c), which is reasonable because the fraction of the short-living coupled Mn^{2+} ions becomes more and more dominant at longer wavelengths.
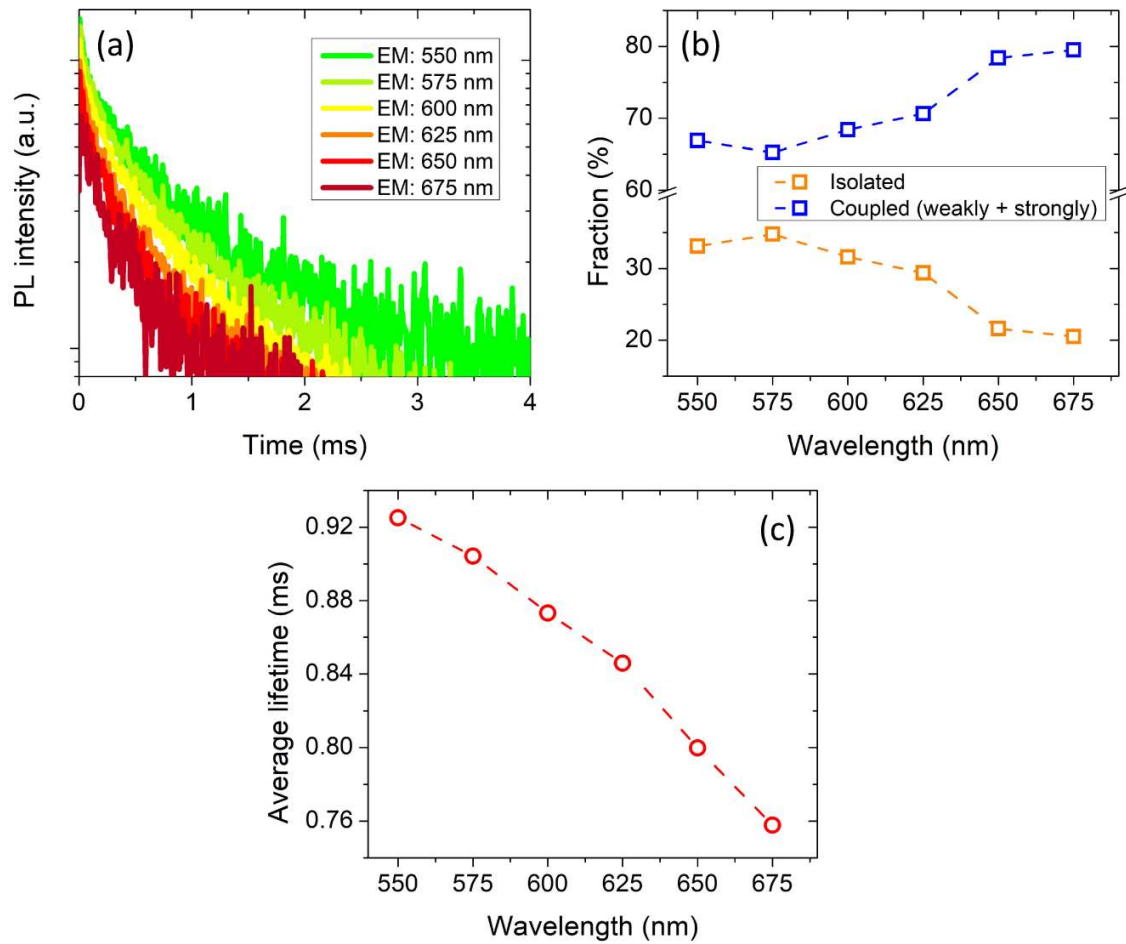
Figure 3-17. (a) PL decay curves of ZnS:Mn (18 Mn^{2+} ions per NPL) NPLs at different emission wavelengths. (b) Wavelength-dependent fraction of the isolated and coupled Mn^{2+} ions. (c) PL average lifetime for the sample at different emission wavelengths.

3.2.6 Enhancement of the Photoluminescence Quantum Yield

The PLQY of ZnS:Mn NPLs as a function of the Mn^{2+} doping level is demonstrated in Figure 3-18a. For each doping level, the PLQY was measured three times with different samples and the error bars are also displayed. It appears that initially the PLQY increases with increasing doping level and reaches a maximum of 1.25% at a doping level of 0.69%. This increase can be ascribed to the introduction of more Mn^{2+} luminescent centers. With continually increasing the doping level, however, the PLQY decreases gradually, which can be assigned to the strong concentration-quenching effect.[151] From

76

the PLQY results, it seems that the doping level of 0.69% is a critical point where the $Mn^{2+}-Mn^{2+}$ interaction becomes dominant, which strongly influences the optical properties of doped NPLs. It is also possible to evaluate the PLQY contribution per Mn^{2+} ion for the series of samples. As shown in Figure 3-18b, the PLQY contribution per Mn^{2+} ion decreases monotonically in the entire doping range. This is perhaps due to competitive effects of addition of more luminescent centers, self-purification, and introduction of more strain and defects on the surface and inside.
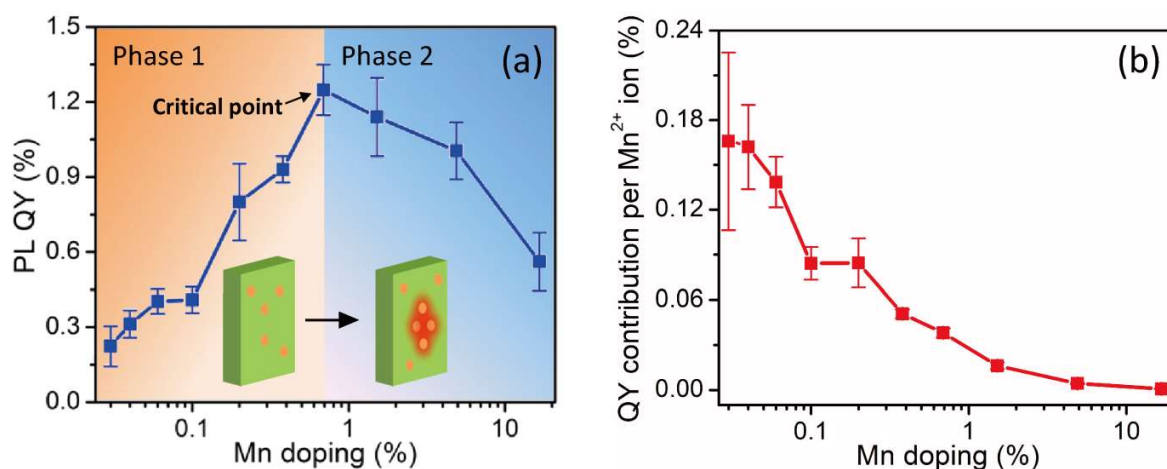
Figure 3-18. Influence of the Mn^{2+} concentration on the PLQY of ZnS:Mn NPLs. Plots of (a) the PLQY of ZnS:Mn NPLs and (b) the corresponding PLQY contribution per Mn^{2+} ion as a function of the doping level determined by ICP-OES.

The PLQY (0.22−1.25%) of Mn^{2+}-doped NPLs shown above is relatively low in comparison to the reported Mn^{2+}-doped dots and rods,[128, 152] which is probably due to the presence of numerous surface trap states. To investigate the influence of the surface trap states, the following control experiments exemplarily for the ZnS:Mn NPL sample with estimated 18 Mn^{2+} ions per NPL (0.38% doping level determined by ICP-OES) were performed. First, the PLQY of the original OAm/OTA-capped sample was measured to be 0.93% (see Figure 3-19, red). After washing once, the PLQY of the sample dropped significantly to 0.43% (cf. Figure 3-19, green). A further decrease in the PLQY of the sample was observed after a second washing step (cf. Figure 3-19, blue). According to the literature,[153-154] the reduced PLQY upon removal of ligands could be ascribed to two

mechanisms: (1) the formation of unstable structures and (2) the exposure of more surface trap states. In the current case, the first possibility can be ruled out because the UV−vis absorbance and PL spectral profile of the sample did not change before and after washing (see Figure 3-19). In a next step, the surface of the sample was passivated again by OAm and OTA via the addition of the ligand solution.
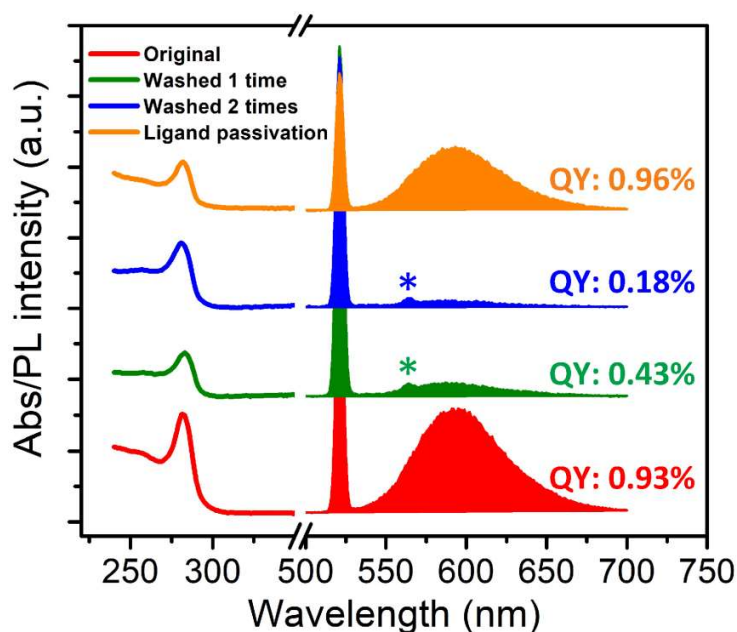
Figure 3-19. Influence of the ligand passivation on the optical properties of ZnS:Mn NPL. Left: UV−vis absorbance spectra of ZnS:Mn NPLs synthesized with a nominal Mn:Zn:S ratio of 0.01:1:3 in the synthesis. Right: The corresponding room-temperature PL emission spectra (λ_{exc} = 260 nm). The second-order scattering of the solvent (hexane) Raman peaks (marked with an asterisk) and the lamp peaks (narrow peaks at 520 nm) are also visible. The spectra are vertically shifted for clarity.

Afterwards, it is noted that the PLQY of the passivated sample increased to 0.96% (cf. Figure 3-19, orange) basically consistent with that of the initial sample. This ligand-related luminescence change proves the existence of numerous surface trap states in ZnS:Mn NPLs. The decrease in the PLQY can be thus explained by the increasing number of unpassivated surface trap states.

Furthermore, the spectra of the washed samples show no other emission except the Mn^{2+} emission band centered at ~590 nm (see Figure 3-20), indicating that the energy released by the surface trap states was through a nonradiative process.
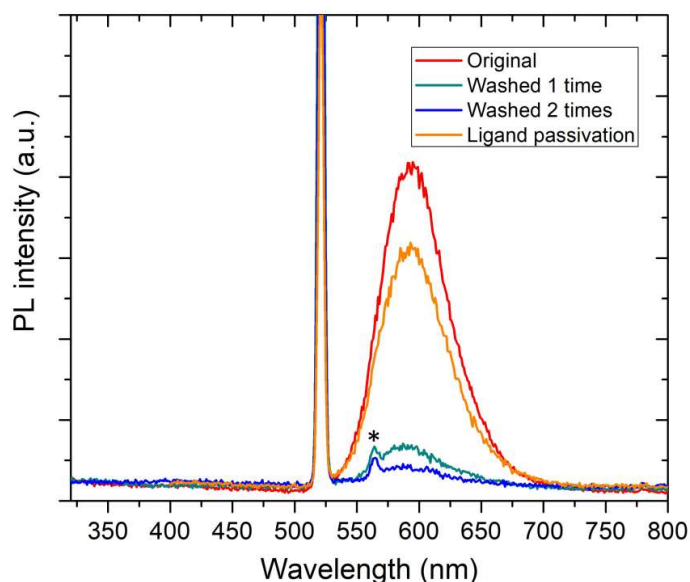
Figure 3-20. Room temperature PL spectra of ZnS:Mn NPLs synthesized with an Mn:Zn:S ratio of 0.01:1:3 in the synthesis (λ_{exc} = 260 nm). The 2nd order scattering of the solvent (hexane) Raman peaks (marked with an asterisk) and the lamp (narrow peaks at 520 nm) are also shown.

The surface trap states induced low PLQY of ZnS:Mn NPLs was further confirmed by employing the following post-synthetic treatment. In this treatment, a zinc-containing precursor solution ($ZnCl_2$ in hexane) was used to passivate the surface of the ZnS:Mn NPLs. As in the experiment above, the ZnS:Mn NPLs with 18 Mn^{2+} ions per NPL were studied. After addition of the Zn^{2+} ion solution to the doped NPL dispersion, it can be seen that the PLQY of the sample increased substantially from 0.93% to 2.32% (cf. Figure 3-21a, right). Both absorption and PL peak positions of the sample remained nearly unaltered (cf. Figure 3-21a, left), suggesting that the thickness and uniformity of the NPLs were not affected significantly during this treatment. For comparison, a S^{2-} solution (hexane) was introduced into the doped NPL dispersion. It turns out that the PLQY of the sample dropped significantly compared to the original one (cf. Figure 3-21b).
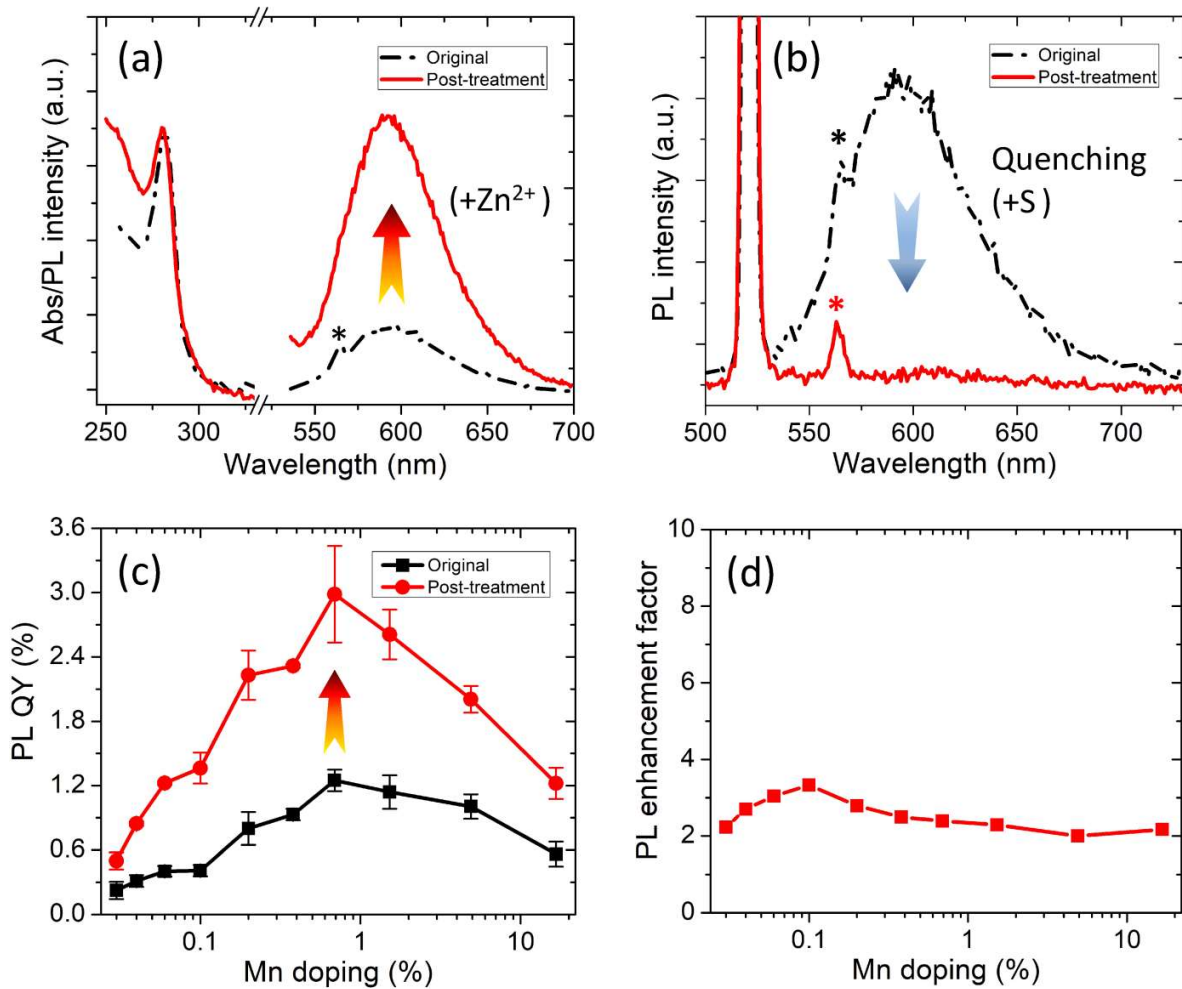
Figure 3-21. Enhancement of the PLQY. (a) Left: UV−vis absorbance spectra of ZnS:Mn NPLs before (black dashed) and after (red solid) the post-treatment with a Zn^{2+} solution. Right: The corresponding room-temperature PL emission spectra (λ_{exc} = 260 nm) of the sample. (b) PL emission spectra (λ_{exc} = 260 nm) of ZnS:Mn NPLs before (black dashed) and after (red solid) the post-treatment with a S^{2-} solution. (c) Plot of the PLQY of ZnS:Mn NPLs as a function of the doping level. (d) The enhancement factor of the PLQY over the doping level. The second order scattering of the solvent (hexane) Raman peaks (marked with an asterisk) and the lamp peaks (narrow peaks at 520 nm) are also visible.

This decrease in the PLQY is a result of the quenching effect of S^{2-} ions due to photogenerated hole trapping.[155-156] This post-treatment with a Zn^{2+} ion solution is also applicable to other samples with different doping levels. Figure 3-21c shows that the

PLQY of all samples (from 0.02% to 16.64%) was boosted after the surface passivation. The enhancement factor for all samples was calculated to be ~2.5 (see Figure 3-21d). This is reasonable since all samples have an identical surface-to-volume ratio.

3.3 Conclusions

In this work, direct doping of the colloidal ZnS NPLs with Mn^{2+} ions via the nucleation-doping strategy was achieved, which was not reported in literature for the ZnS NPLs so far. With a certain amount of Mn^{2+} ions incorporated into the ZnS matrix, the shape and phase of the host were unchanged. The obtained ZnS:Mn NPLs exhibit orange luminescence that can be clearly observed by eye and is attributed to the $d-d$ transitions of Mn^{2+} ions. The correlation between the doping level and the evolution of PL properties was established, which reveals the presence of the energy-transfer between ZnS and Mn^{2+} ions. The atomic environment of the dopant ions was determined using EPR and XPS. Based on that, it provides insights into the relaxation mechanisms of the excited charge carriers in quasi-2D NPLs. The relationship between Mn^{2+} species (isolated and coupled Mn^{2+} ions) and Mn^{2+} PL kinetics was revealed by means of TRPL, which is further supported by DFT-based calculations.

In addition, the surface of the NPLs was found to be a critical and limiting factor for the effective energy conversion. It is shown that the PLQY can be substantially enhanced by passivating the surface of the samples with an appropriate ion solution. The presented synthetic strategy of the ZnS:Mn platelets and the surface post-treatment opens a new pathway to synthesize further doped systems of quasi-2D NPLs and to improve their PLQY.

3.4 Experimental Section

3.4.1 Chemicals

Zinc chloride (97+%), octylamine (OTA, 99+%), and methanol (99.8%) were purchased from Acros. Sulfur powder (99.998%), manganese (II) acetate (98%, $Mn(OAc)_2$), nitric acid, and oleylamine (OAm, 70%) were ordered from Sigma-Aldrich. Toluene (99.5%), isopropanol (99.7%), and hexane (95%) were purchased from VWR

.Acetone (99%) was purchased from Th. Geyer Chemicals. All chemicals were used without further purification.

3.4.2 Synthesis of ZnS:Mn Nanoplatelets

Standard Synthetic Procedure for ZnS:Mn NPLs. In a three-necked flask equipped with a septum and a thermocouple in a glass mantle, 0.15 mmol (20.4 mg) of $ZnCl_2$, 0.45 mmol (14.4 mg) of sulfur powder, and a certain amount of $Mn(OAc)_2$ were dissolved in a mixture of 10 mL of OAm and 5 mL of OTA. The mixed solution was bubbled with nitrogen at 100 °C for 30 min under vigorous stirring. Afterwards, the reaction solution was heated to 150 °C for 6 h with magnetic stirring under nitrogen flow. After the reaction, the solution was naturally cooled to room temperature. The resulting NCs were purified as follows: (1) 15 mL of reaction solution was mixed with 5 mL of acetone and 5 mL of isopropanol. (2) The mixture was shaken well and centrifuged for 10 min at 9000 rpm. (3) The supernatant was discarded, and the precipitation was dispersed into 3 mL of hexane or toluene for further characterization.

Synthesis of ZnS:Mn NPLs with variable Mn^{2+} concentrations. For the synthesis of ZnS:Mn NPLs with different Mn^{2+} concentrations, the amount of $Mn(OAc)_2$ was varied while the amounts of $ZnCl_2$ and sulfur powder in the initial mixture were fixed.

3.4.3 Ligand-dependent Photoluminescence

A certain volume of ZnS:Mn NPL dispersion (hexane) was purified by precipitation with a mixture of acetone/isopropanol (1:1 vv), centrifugation, removal of the supernatant and re-suspension in hexane. The purification process can be repeated to further get rid of ligands. To passivate the NPLs again, a mixture of OAm/OTA (2:1 vv) was added. The NPL dispersion was stirred for 10 min at room temperature, followed by centrifugation for 10 min at 9000 rpm to remove excess OAm and OTA. Finally, the passivated NPLs were re-dispersed into hexane.

3.4 Experimental Section

3.4.4 Characterizations

TEM. TEM images were taken by using a JEOL Jem-1011 microscope at an acceleration voltage of 100 kV. Samples for the TEM analysis were prepared by drop-casting 10 μL of the dilute NC dispersion onto carbon-coated copper grids. HRTEM images and EDX spectra were obtained with a Philips CM 300 UT microscope operated at an acceleration voltage of 200 kV.

XRD. XRD measurements were performed with a Philips X'Pert PRO MPD diffractometer with monochromatic X-ray radiation from a copper anode with a wavelength of 0.154 nm (Cu Kα). Samples for the XRD analysis were prepared by drop-casting a few μL of the concentrated NC solution onto silicon wafer substrates with subsequent solvent evaporation.

UV−vis Absorbance and PL Spectra. Steady-state UV−vis absorbance and PL spectra were obtained with a PerkinElmer Lambda 25 two-beam spectrometer and a Horiba Fluoromax-4 spectrometer, respectively. TRPL measurements were performed with Picoquant FluoTime 300 fluorescence spectrometer. Samples were prepared by adding a few μL of the NC solution into 3 mL of hexane in quartz vessels with an optical path length of 10 mm.

ICP-OES. Mn^{2+} concentrations in the NPLs were determined via ICP-OES (type: ARCOS) produced by Fa. Spectro. Samples for the ICP-OES analysis were prepared with three steps: (1) 2 mL of the concentrated NC solution was pipetted into a 25 mL beaker and evaporated at room temperature. (2) The dried sample was dissolved in 4 mL of concentrated HNO_3 at 160 °C. (3) The mixed solution was diluted in a 25 mL volumetric flask.

XPS. XPS was performed on a Kratos Axis Supra instrument using a monochromatic Al Kα X-ray source operated at 225 W (15 mA emission current). For each sample wide scans were performed at a pass energy of 160 eV over the 1200−0 eV binding energy range to identify all the elements present on the surface. Based on the survey scans, high-resolution spectroscopy was recorded for each element as a pass energy of 40 eV. Typically high-resolution spectra were recorded with a step size of 0.1 eV, with a 1000

ms dwell time and repeated sweeps to improve the signal:noise. The charge neutralizer was used to eliminate any differential charging, and subsequently the binding energy axis was corrected to the CxHy component of the carbon components at 284.8 eV. Data were quantified by using CasaXPS (2.3.23rev1.1K) with the Kratos sensitivity factor library based on Shirley backgrounds.

EPR Spectroscopy. EPR measurements were recorded at 100 K on a Bruker EMX CW-micro X-band EPR spectrometer equipped with an ER4119HS high-sensitivity resonator, with a microwave power of Ca 6.9 mW, modulation frequency of 100 kHz, and amplitude of 5 G. The EPR spectrometer was equipped with a temperature controller and liquid N_2 cryostat for low-temperature measurements. For each measurement, 2 mL of ZnS:Mn NPLs with different Mn^{2+} doping levels (in hexane) was used. For calculation of g values, the equation $hv = g\beta B_0$ was used with β, B_0, and v being the Bohr magneton, resonance field, and frequency, respectively. Calibration of the g values was performed by using a DPPH standard ($g = 2.0036 \pm 0.0004$). The EPR spectra of the samples were simulated by using the software package Easyspin implemented in MATLAB.

DFT Calculations. DFT calculations have been carried out within the LDA in coorperation with the group of *Prof. Gabriel Bester* (contributed by *Dr. Abderrezak Torche*). The slab was constructed as $3 \times 3 \times 4$ repetition of a ZnS bulk supercell with 8 atoms and thus containing 288 atoms. Structural relaxation with stress minimization has been performed using the default convergence values of the quantum espresso package followed by ground state calculations to generate the Kohn−Sham energies and wave functions. Note that the relative position of the d-level of Mn^{2+} ions with respect to the ZnS bulk VBM and CBM are not accurate at the DFT-LDA level due to the known lack of correlation. This could have been corrected with post-DFT methods such as the GW approximation. However, due to the large simulation cell, this type of calculations could not be performed. It is also worth noting that the previous problem is not supposed to influence the lifetime calculation as this latter is mainly wave-function-dependent only through eh M_if and DFT and GW wave functions are in most cases identical up to a very good approximation.

CHAPTER 4

Shell Growth on ZnSe:Mn Nanoplatelets

4.1 Introduction

4.1.1 Background

In the past two decades, core/shell NCs are highly demanded in practical applications because of their improved optical and electronic properties. When designing core/shell NCs, the lattice mismatch between the core and the shell compound has to be considered. Generally, the lattice mismatch should be small enough so that the shell can epitaxially grow on the core without inducing interfacial defects.[157] These defects can act as trap states for photogenerated charge carriers, and thereby diminish the PLQY. Besides, other growth modes (*i.e.* "island" growth) will take place and the formation of core/shell structures will be less likely as the shell and core exhibit a large lattice mismatch.

A variety of methods have been applied to achieve high-quality shell growth. To minimize the interfacial defects induced by large lattice mismatch, either alloyed shells or shells with graded composition were coated on the core materials. For example, Xie et al. showed that the shell composition can be gradually tuned from CdS to alloyed $Zn_{0.5}Cd_{0.5}S$ to ZnS through a successive ion layer adhesion and reaction technique, which effectively reduces the interfacial defects.[158] Consequently, the obtained core/shell QDs exhibit a high PLQY of up to 85%. Similarly, $CdSe/Cd_{1-x}Zn_xS$ core/shell NRs with graded composition were synthesized by Banin et al.[159] By tuning the Zn amount, the core/shell NRs show bright and highly polarized green emission with minimal intermittency. Heavy-metal-free core/shell Zn chalcogenide NCs are also well developed. The lattice mismatch between ZnSe and ZnS is relatively small (~4.5%) compared to that between CdSe and CdS (7.6%).[160] Therefore, less strain will be induced when the ZnS shell is coated on the ZnSe core. Many research groups have shown successful syntheses of highly fluorescent ZnSe/ZnS core/shell QDs.[161-163] Very recently, Banin et al. investigated the effect of the ZnSe shell growth rate on the structure and optical properties of ZnSe/ZnS core/shell QDs.[164] The authors noted that the growth mode of the ZnS shell on ZnSe cores can be tuned from kinetic (fast) to thermodynamic (slow) growth regimes by changing the precursor reactivity. The thermodynamic growth promotes the epitaxial growth of a ZnS shell, and therefore core/shell QDs with enhanced PLQY and reduced on−off blinking are achieved.

4.1 Introduction

Unlike core/shell QDs, the synthesis of core/shell NPLs is still a big challenge. For example, NPLs with anisotropic structures have big energy differences between basal and side facets, which commonly leads to inhomogeneous or selective deposition of a shell. As a consequence, core/crown NPLs form. The second issue is the poor thermal stability of NPLs. As discussed in Chapter 1, NPLs tend to re-dissolve at high temperatures due to the high solubility. Recently, efforts have been made to improve the thermal stability. In a synthesis of CdSe/CdS core/shell NPLs, Norris and co-workers[62] added excess Cd precursor into the shell-growth solution prior to raising the reaction temperature. When the concentration of Cd precursor is above the solubility of CdSe NPLs, the dissolution becomes unfavorable, and thereby CdS shells can grow on CdSe cores. Although successful preparation of core/shell NPLs has been shown, precise control in shell thickness and morphology is still difficult. Additionally, the mechanisms for the shell growth on NPLs via high-temperature methods are not fully understood.

4.1.2 Motivation

Quasi-2D NPLs possess a large number of exposed surface atoms because of higher surface to volume ratio relative to 0D and 1D NCs. These surface atoms are incompletely bonded to the other atoms in the crystal structure, which can result in dangling bonds. When the surface of NPLs is not completely passivated, the unshared atomic orbitals of surface atoms can create energy levels within the band gap.[165-166] The generated surface trap states are detrimental to the PLQY of NPLs, because trapping of charge carriers can reduce the overlap between the electron and hole wave functions, thereby the radiative recombination becomes less likely. Instead, the exciton decays nonradiatively.

To address the low PLQY issues, it is necessary to develop strategies to protect charge carriers away from the surface and/or eliminate surface trap states. Currently, two approaches are reported: (1) coating the surface with suitable ligands and (2) overgrowing a shell of a material (*e.g.* a semiconductor with a larger band gap) on the bare NPLs. The ligand-based approach has been experimentally proven to be effective for the enhancement of the PLQY in Chapter 3. Here, the fabrication of type-I core/shell structures is taken into account to achieve highly luminescent NPLs. Secondly, doping is

also applied into such core/shell NPLs to investigate the emission kinetics of the host and dopants, as well as the influence of the shell on the optical properties of NPLs.

4.2 Results and Discussion

4.2.1 Synthesis of ZnSe Nanoplatelets

ZnSe NCs, as heavy-metal-free semiconductors, emit light in wavelength ranging from ~320 nm to 460 nm, making them promising candidates for blue light-emitting diodes.[167-168] Moreover, ZnSe has a smaller band gap than ZnS, which allows designing ZnSe-based type-I core/shell heterostructures. Because of high similarity between ZnS and ZnSe, the recipe for the synthesis of ZnS NPLs was extended to prepare ZnSe NPLs. In all syntheses, temperature, and amounts of precursors were unchanged. Briefly, zinc chloride and selenium powder with a nominal Zn:Se molar ratio of 1:3 were dissolved in a mixture of OAm and OTA. The mixture was purged with nitrogen at 100 °C for half an hour and then was heated to 150 °C for 6 hours. After the reaction, the purified products were characterized by TEM. The result (see Figure 4-1b) shows that the products have a platelet-like shape, but they were connected forming branched structures.
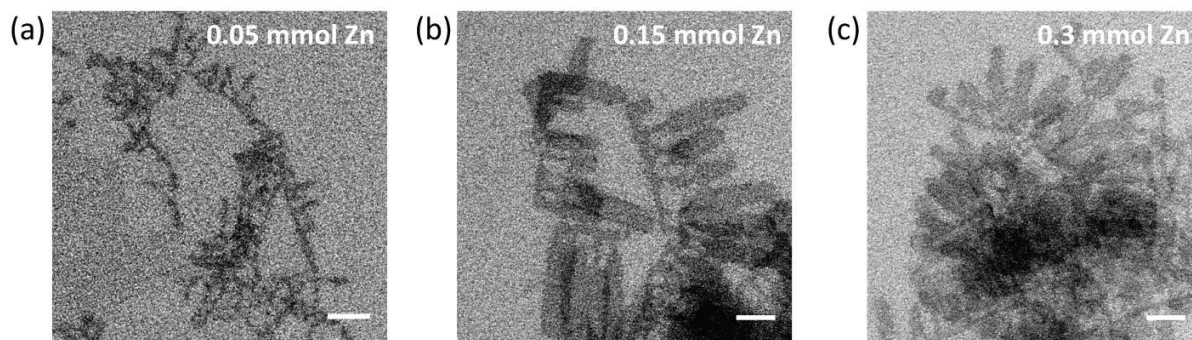
Figure 4-1. Influence of the amount of the Zn precursor on the shape of ZnSe NCs. TEM images of ZnSe NCs synthesized at 150 °C with (a) 0.05, (b) 0.15, and (c) 0.3 mmol Zn, respectively. Scale bars represent 20 nm.

The formation of platelets indicates that the soft-template-based recipe is effective for the synthesis of ZnSe NPLs despite the existence of some by-products. To remove the

branched structures, the recipe was modified. First, the variation of the precursor amount is taken into account since it can strongly influence the formation of the final products in colloidal syntheses.[87, 169] Here, the amount of the Zn precursor was changed while the molar ratio between Zn and Se was fixed to 1:3. When the amount of the Zn precursor was reduced to 0.05 mmol, the branched structures were still present and the width of the platelets narrowed (see Figure 4-1a). Apparently, reduction in the amount of precursors plays a negative role in achieving well-separated NPLs. The amount of the Zn precursor was then increased to 0.3 mmol. It is found that the result was similar compared to that of 0.15 mmol Zn (see Figure 4-1c). This suggests that the variation of the precursor amount has almost no impact on the removal of the branched structures.

Temperature, as another critical parameter in the NC synthesis, can tune the morphology of NCs by changing the reaction activity.[10, 39] In the following synthesis, the temperature was increased while other parameters were fixed.
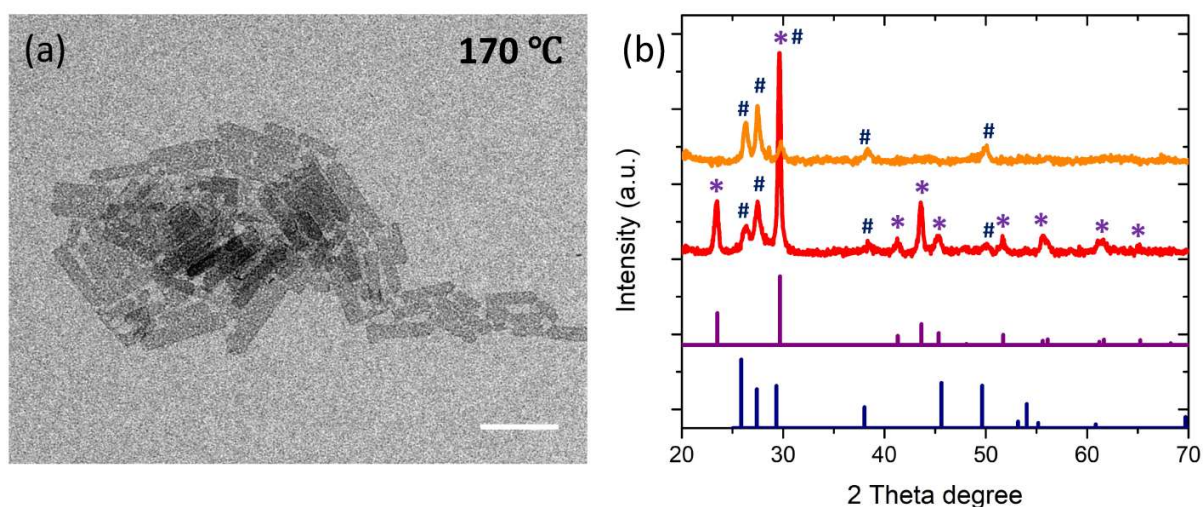
Figure 4-2. Shape and phase characterization of ZnSe NPLs. (a) TEM image of ZnSe NPLs synthesized with 0.15 mmol Zn at 170 °C. The scale bar represents 100 nm. (b) XRD patterns of ZnS NPLs purified without (red) and with (orange) TOP. At the bottom, the reference patterns of WZ-ZnSe (dark blue, ICPDS 01-080-0008) and Se powder (purple, ICPDS 01-073-0465) are also shown. The XRD patterns are vertically shifted for clarity.

4.2 Results and Discussion

Note that the highest temperature that can be raised is ~170 ℃, which is very close to the boiling point of OTA. The TEM image (see Figure 4-2a) of the product obtained at 170 ℃ shows that the NPLs were separated without branched structures. The uniform contrast suggests that the NPLs have a homogeneous thickness. This result reveals that a higher temperature is required for the synthesis of ZnSe NPLs in comparison to that of ZnS NPLs. To determine the crystal structure of the obtained NPLs, XRD was performed. The XRD pattern (see Figure 4-2b, red) indicates that the NPLs have the WZ structure of ZnSe (ICPDS 01-080-0008). However, the product is not phase-pure and several diffraction peaks (marked with asterisks) that matches to Se powder (ICPDS 01-073-0465) were observed. Considering that Se is in excess (molar ratio of Zn:Se = 1:3) in the synthesis, the diffraction peaks of Se could be from the unreacted Se powder. To confirm this, a certain amount of trioctylphosphine (TOP) that was used as dispersant for the preparation of TOP-Se in many syntheses[55, 170-171] were added into the product solution after reaction. The XRD pattern of the purified sample (see Figure 4-2b, orange) displays all characteristic peaks of the WZ-ZnSe pattern (ICPDS 01-080-0008) without any impurity peaks.

The optical properties of ZnSe NPLs were characterized by steady-state UV−vis absorbance and PL spectroscopy, respectively. The UV−vis absorbance spectrum (see Figure 4-3, black) shows two sharp peaks at 328 nm (~3.78 eV) and 345 nm (~3.59 eV), which can be assigned to the light hole−electron and heavy hole−electron transitions, respectively.[172] The absorption peaks were significantly blue-shifted compared to peaks of bulk ZnSe (E_g = 2.7−2.8 eV),[5] suggesting the existence of strong quantum confinement. The steady-state PL spectrum (see Figure 4-3, red) shows an obvious emission band at 347 nm, which is not reported for ZnSe NPLs perhaps due to massive surface trap states.[173] The narrow emission with a FWHM of 7.5 nm indicates a uniform thickness of the NPLs, which agrees with the TEM results.
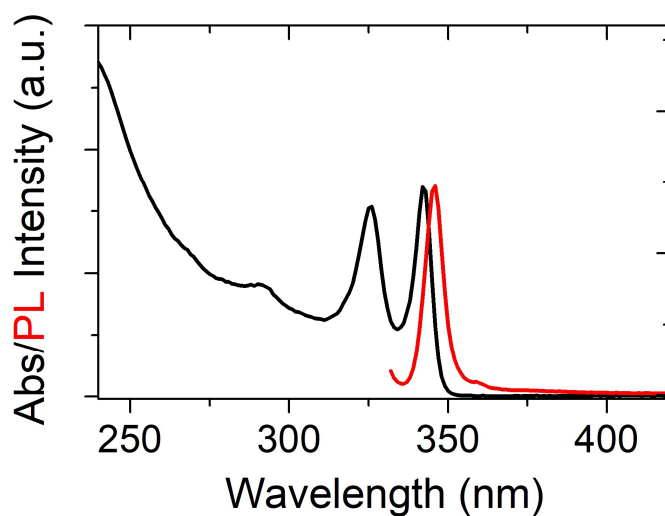
Figure 4-3. Optical characterization of ZnSe NPLs. UV−vis absorbance (black line) and PL (red line) spectra of ZnSe NPLs synthesized with 0.15 mmol $ZnCl_2$ and 0.45 mmol Se powder at 170 °C.

4.2.2 Doping of ZnSe Nanoplatelets with Mn^{2+} Ions

The recipe for the synthesis of ZnSe:Mn NPLs is the same as that for the ZnSe NPLs, except that a certain amount of Mn precursor (nominal Mn:Zn:S molar ratio of x:1:3) is added. Here x is set to 8%. The TEM image (see Figure 4-4a) shows that the as-synthesized ZnSe:Mn (x = 8%) NCs retain platelet-like as Mn^{2+} ions were added. The mean length and width of ZnSe:Mn NPLs were calculated to be 61.1 and 17.3 nm (see Figure 4-4b and c), respectively. Additionally, the crystal structure of the doped NPLs is found to be nearly unchanged by Mn^{2+} ions (see Figure 4-4d). The main diffraction peaks correspond to the WZ structure of ZnSe (ICPDS 01-080-0008). Both TEM and XRD results suggest that all experimental parameters of the ZnSe NPL synthesis also work very well for the synthesis of the ZnSe:Mn NPLs.
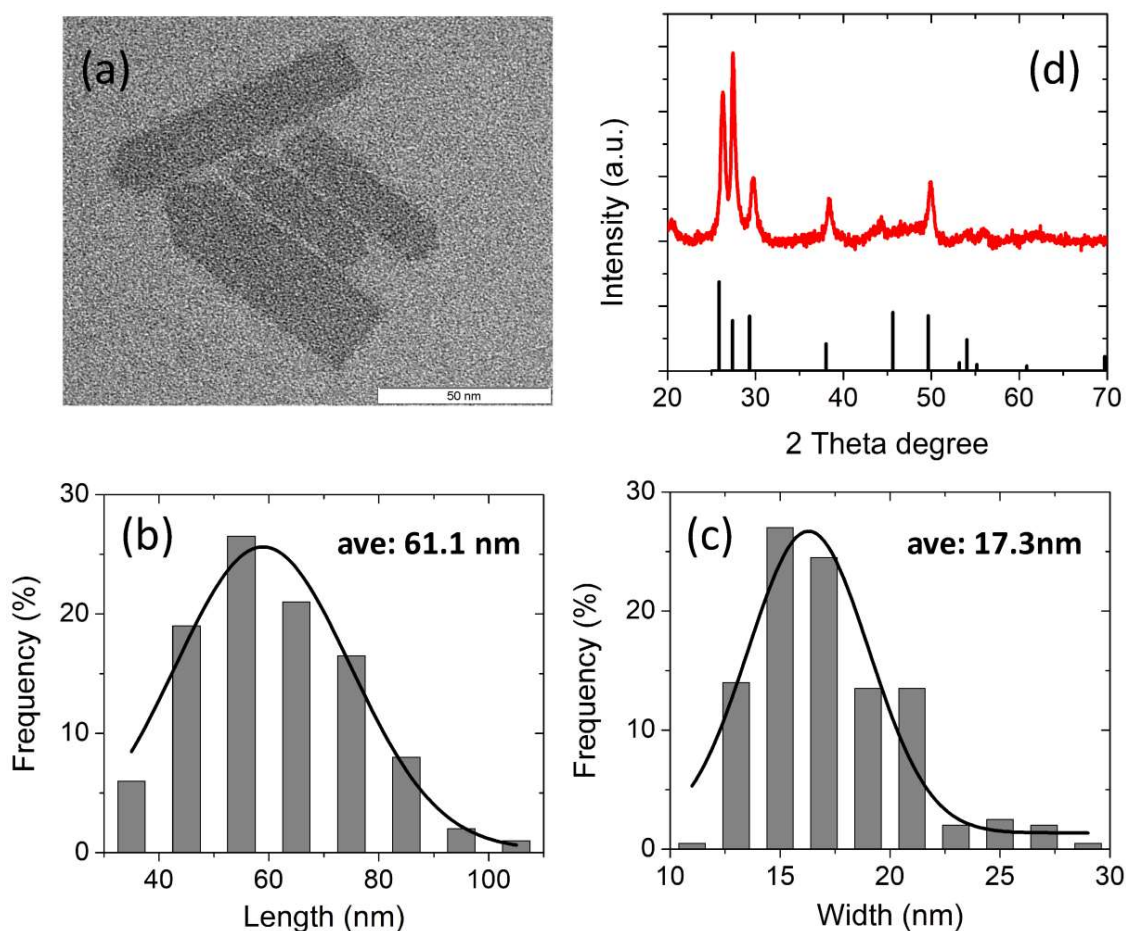
Figure 4-4. Shape and phase characterization of ZnSe:Mn NPLs. (a) TEM image and (d) XRD pattern of ZnSe:Mn ($x = 8\%$) NPLs. At the bottom, the reference pattern of WZ-ZnSe (black, ICPDS 01-080-0008) is displayed. The (b) length and (c) width distribution histograms of ZnSe:Mn ($x = 8\%$) NPLs.

To check if Mn^{2+} ions were incorporated into the ZnSe NPLs, optical spectroscopy measurements were performed. From the UV−vis absorbance spectrum of ZnSe:Mn ($x = 8\%$) NPLs (see Figure 4-5a, black), no significant change was observed in comparison to ZnSe NPLs. However, a new strong emission band centered at 590 nm was observed in the PL spectrum in addition to the typical BE emission of ZnSe NPLs (see Figure 4-5a, red). This broad orange emission can be attributed to the Mn^{2+} ion $^4T_1-^6A_1$ transitions,[76] revealing the successful doping of the ZnSe crystal lattice with Mn^{2+} ions. It is worth noting that the peak marked with an asterisk is not a PL signal but a Raman signal from

the solvent (hexane).[128] The presence of the energy-transfer between the ZnSe and Mn^{2+} ions was evidenced by comparing the UV−vis absorbance and PLE spectra monitored at 590 nm. As can be seen (see Figure 4-5b), the PLE spectrum of Mn^{2+} ions coincides perfectly with the absorbance spectrum of ZnSe.
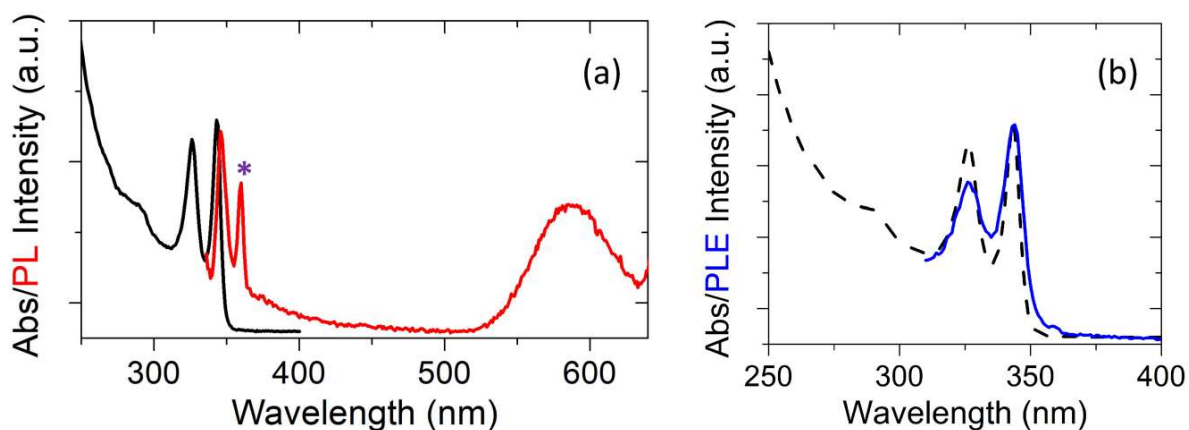
Figure 4-5. Optical characterization of ZnSe:Mn ($x = 8\%$) NPLs. (a) UV−vis absorbance (black) and PL (red) spectra of ZnSe:Mn ($x = 8\%$) NPLs ($\lambda_{exc} = 325$ nm). The scattering of the solvent (hexane) Raman peaks (marked with an asterisk) is also visible. (b) The corresponding PLE (blue) spectrum monitored at the maximum of the Mn^{2+} emission.

As "seeds" for the preparation of the ZnSe:Mn/ZnS core/shell NPLs, ZnSe:Mn NPLs play a significant role in influencing the optoelectronic properties of the final core/shell products. Hence, tuning the Mn^{2+} amount to optimize the optical properties of the doped NPLs is very important. Here, the nominal Mn:Zn atomic ratio of the precursors was changed from ~0.06% to 64%. The actual Mn:Zn atomic ratio in the ZnSe:Mn NPLs was determined by ICP-OES, which is shown in Table 4-1. The presented results show that the Mn:Zn atomic ratio determined by ICP-OES is much lower than the one used in the synthesis, revealing that only small parts of Mn^{2+} ions were incorporated into ZnSe NPLs. The average number of Mn^{2+} ions per NPL in the series of samples can be estimated by knowing the mean volume of NPLs ($61.1 \times 17.3 \times 1.4$ nm³). The doping range between 0.01% and 10.23% corresponds to 3−3404 Mn^{2+} ions per NPL.

4.2 Results and Discussion

Table 4-1. The nominal Mn:Zn atomic ratio used in the synthesis, the actual Mn:Zn atomic ratio in the ZnS:Mn NPL samples determined by ICP-OES, and the average number of Mn^{2+} ions incorporated per ZnSe:Mn NPL determined via ICP-OES.

nominal Mn:Zn atomic ratio (%)	Mn:Zn atomic ratio determined by ICP-OES (%)	average number of Mn^{2+} ions per NPL
0.06	0.01	3
1	0.32	108
4	0.90	300
8	0.97	323
16	2.06	686
64	10.23	3404

The absorption and PL features of the series of samples with increasing Mn^{2+} doping level were recorded, which are shown in Figure 4-6. When the doping level increased from 0 to 16%, no obvious change on the absorption spectra was observed. The two characteristic absorption peaks corresponding to the light hole−electron and heavy hole−electron transitions appear in all spectra. With further increase in the doping level, the two absorption peaks broaden slightly, which could be a result of the Mn^{2+} ion influence on the electronic structure of the host.[136] Analyzing the PL spectra, it is found that the center of the BE emission keeps nearly fixed, while the Mn^{2+} emission band red-shifts as the doping level increases (see Figure 4-7a). This distinct red-shift ($\Delta\lambda = 17$ nm) can be ascribed to the $Mn^{2+}-Mn^{2+}$ interaction, which is similar to the previous result of ZnS:Mn NPLs in Chapter 3.
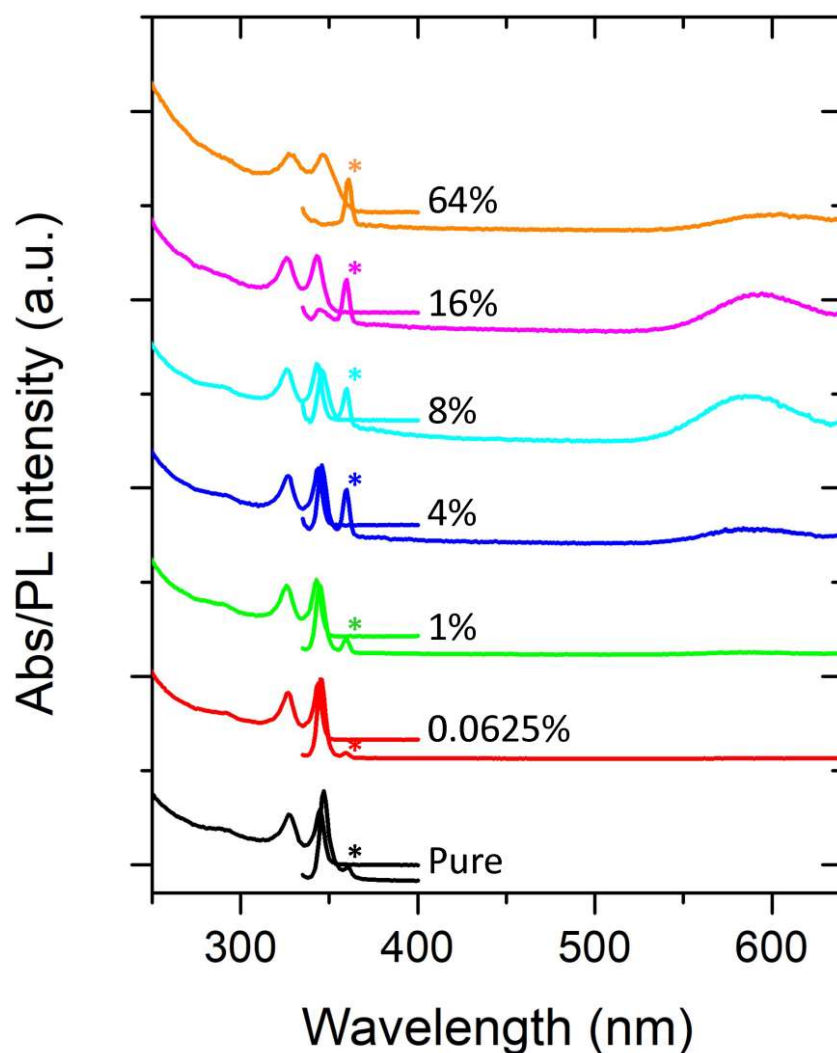
Figure 4-6. Effect of the Mn^{2+} doping level on the optical properties of ZnSe:Mn NPLs. UV−vis absorbance and PL spectra of ZnSe:Mn NPLs with increasing Mn^{2+} doping level added in the synthesis. The scattering of the solvent (hexane) Raman peaks (marked with an asterisk) is also detected. The spectra are vertically shifted for clarity.

Although no shift in the BE emission band is observed, the BE emission kinetics might be changed by the Mn^{2+} doping. To verify this, the TRPL feafures of an undoped sample and a doped sample with a high doping level ($x = 8\%$) were compared. Figure 4-7b shows that the doped NPLs have a faster BE emission decay lifetime in comparison to

the undoped NPLs. This change reveals that doping the ZnSe NPLs with Mn^{2+} ions increases the relaxation rate of the excited charge carrires of ZnSe NPLs.
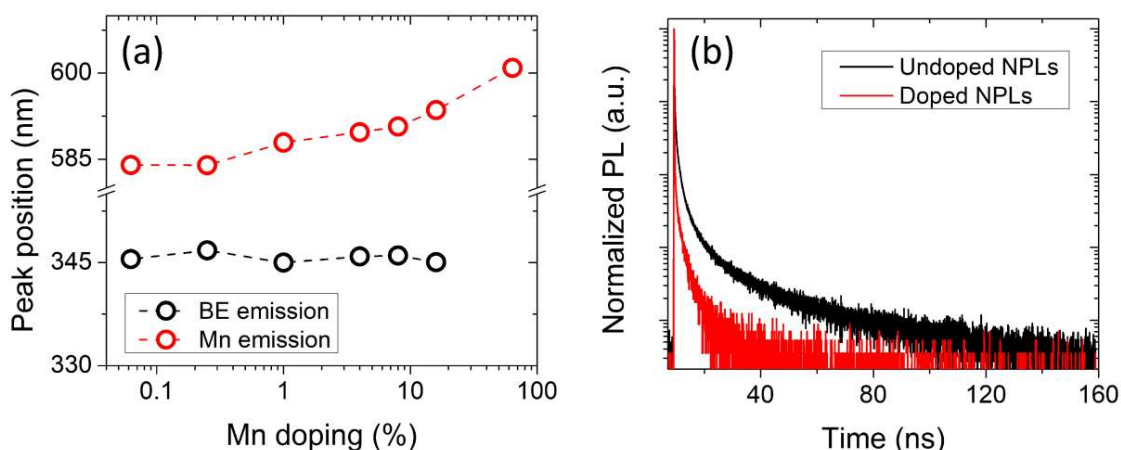
Figure 4-7. (a) Variation of the emission peak position with increasing doping level. (b) BE emission decays of undoped NPLs (black) and doped ($x = 8\%$) NPLs (red).

It is also noted that the BE emission diminishes gradually as the doping level increases, and it almost vanishes at the doping level of 64%. To quantitatively describe the variation in intensity of the BE and Mn^{2+} emission, the PLQYs of the series of the samples were calculated, which is shown in Figure 4-8a. With increasing doping level, the PLQY of the BE emission monotonically decrease from ~0.17% to 0.0%. In contrast, the PLQY of the Mn^{2+} emission increases until the doping level reaches 8%. With further increase in the doping level, it drops. The initial increase can be attributed to the increasing number of Mn^{2+} luminescent centers, while the subsequent decrease is due to the "quenching effect" induced by the strong $Mn^{2+}-Mn^{2+}$ interaction.[136] Such a "quenching effect" is verified by investigating the variation of the Mn^{2+} PLQY per Mn^{2+} ion as a function of the doping level. It shows (see Figure 4-8b) a decrease of the Mn^{2+} PLQY per Mn^{2+} ion with increasing doping level. Besides, it is also found that the total PLQY of ZnSe:Mn NPLs decreases gradually as the doping level increases from 0.0625% to 64%. One of the reasons for the decrease can be attributed to the increasing "quenching effect" between Mn^{2+} ions, which is in line with previous reports.[140, 174] The changes in the PLQY for the BE and Mn^{2+} emission indicate a change in the energy-

transfer efficiency (Φ_{ET}) between the host and the dopant. It is known that the intensity ratio of the Mn^{2+} emission (I_{Mn}) and the host BE emission (I_{BE}) is proportional to the relaxation rate of the host−dopant energy-transfer (k_{ET}) (*i.e.* $I_{Mn}/I_{BE} \square k_{ET}$).[140] As the doping level increases, it is found that I_{Mn}/I_{BE} increases (see Figure 4-8c), suggesting an increase in the energy-transfer rate.
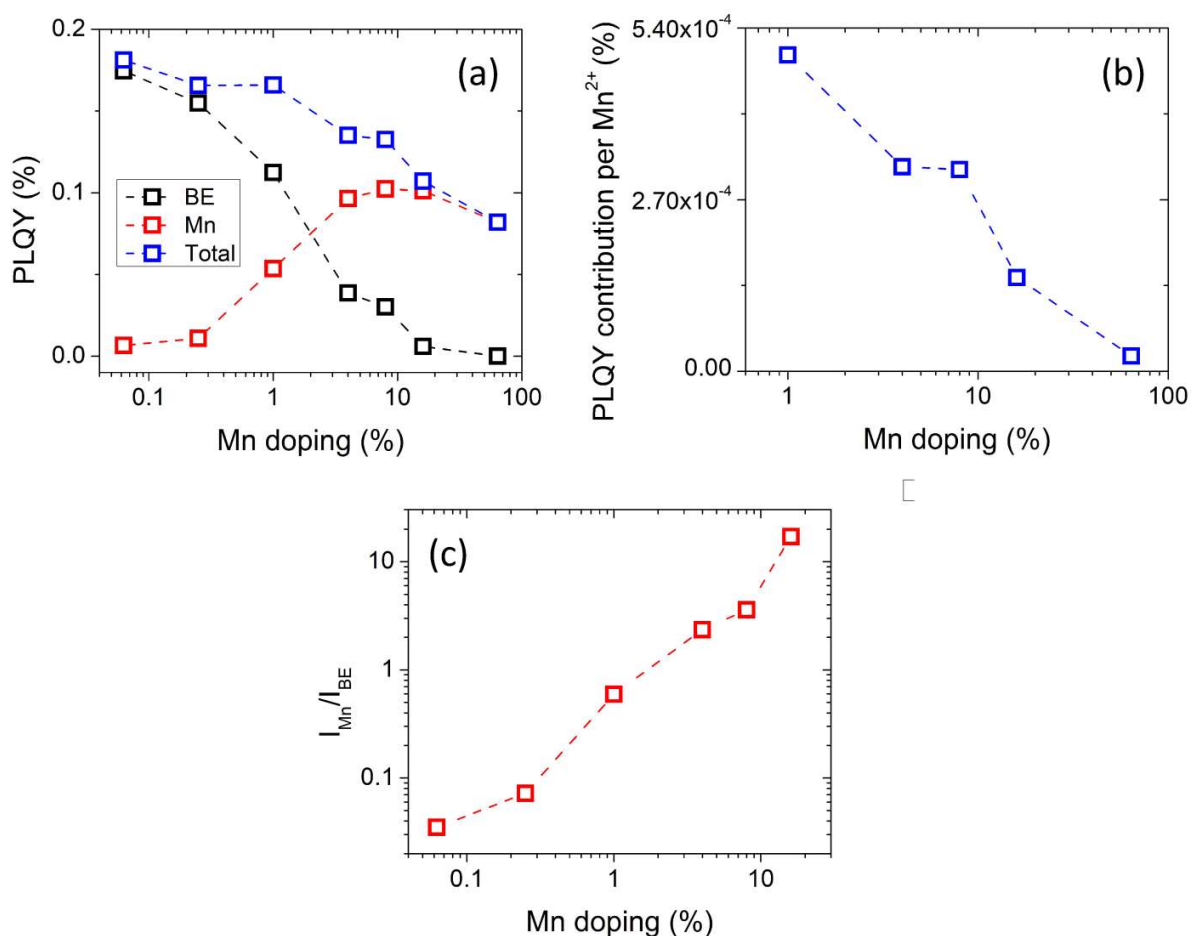
Figure 4-8. Effect of the Mn^{2+} concentration on the BE and Mn^{2+} emission. (a) Plot of the PLQY as a function of the Mn^{2+} doping level added in the synthesis. (b) Variation of the PLQY contribution per Mn^{2+} ion with increasing doping level. (c) Intensity ratio of the BE and Mn^{2+} emission as a function of the Mn^{2+} doping level.

The influence of Mn^{2+} concentrations on the dopant emission kinetics of ZnSe:Mn NPLs was also investigated via TRPL measurements. Interestingly, the average lifetime of the Mn^{2+}

emission increases gradually from 19.8 to 23.1 μs as the doping level increases from 0.0625% to 8% (see Figure 4-9a and b), which is contrary to the previous observation in ZnS:Mn NPLs (see Figure 3-14). Although the reason is unclear, the result suggests that the local environment of Mn^{2+} ions in the ZnSe NPLs is altered by changing the doping level. When the doping level exceeds 8%, the average lifetime of the Mn^{2+} emission decreases dramatically. This decrease can be well-explained by the magnetically coupled Mn^{2+} ions, which coincides with the reported results.[136, 175]
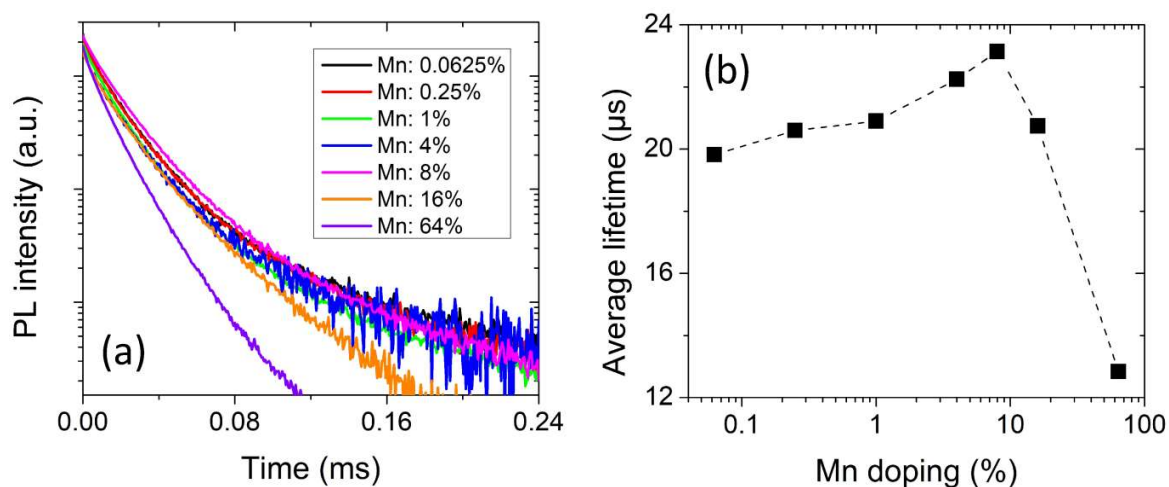
Figure 4-9. Influence of the Mn^{2+} concentration on the Mn^{2+} emission kinetics. (a) Mn^{2+} PL decay of ZnSe:Mn NPLs with increasing Mn^{2+} doping level added in the synthesis. (b) Plot of the average lifetime of the Mn^{2+} emission as a function of the doping level.

4.2.3 ZnS Shell Growth

The above results show that colloidal ZnSe:Mn NPLs with well-defined structure were successfully synthesized. To improve the optical properties and environmental stability, ZnS shells were grown on the ZnSe:Mn NPLs to obtain ZnSe:Mn/ZnS core/shell NPLs using the c-ALD method.[65] This method allows the precise control of the ZnS shell at the atomic scale. Additionally, unlike other methods (*e.g.* one-pot and hot-injection), c-ALD can be conducted at room temperature, which effectively avoids the poor thermal stability issue of platelets.[62] Here, ZnSe:Mn (*x* = 8%) NPLs were chosen as "seeds" for the fabrication of core/shell NPLs since they exhibit better optical performance (*e.g.* a

higher PLQY and longer lifetime) compared to the samples with other doping levels. After five cycles of c-ALD was performed, the product still remains platelet-like (see Figure 4-10). Nevertheless, different from the core NPLs (see Figure 4-4a), the edges of the core/shell NPLs are not smooth and have higher contrast than their center. Similar results can be seen in previous reports.[176-177] This suggests that the ZnS shell is inhomogeneous.
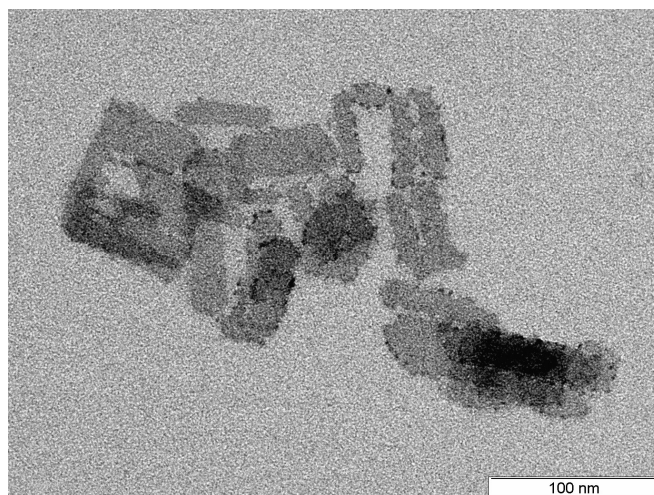
Figure 4-10. TEM image of ZnSe:Mn/ZnS core/shell NPLs synthesized by using the c-ALD method.

To check if the ZnS shell really grows on the ZnSe:Mn NPLs, atomic force microscopy (AFM) measurements were performed to compare the thickness of the ZnSe:Mn NPLs and ZnSe:Mn/ZnS core/shell NPLs. To minimize the deviation, the thickness of each NPL was measured four times in different directions. Figure 4-11a shows that the mean thickness of the ZnSe:Mn NPLs is measured to be ~1.70 nm, smaller than the mean thickness (~3.98 nm) of the ZnSe:Mn/ZnS core/shell NPLs (see Figure 4-11b). This increase in thickness of the NPLs qualitatively suggests that the ZnS shell successfully grows on the ZnSe:Mn core NPLs via the c-ALD method. Additionally, according to the measured values, it can be known that the thickness of the ZnS shell is ~1.14 nm. Assuming that each cycle of the c-ALD process can generate one ML of the ZnS (~0.31 nm[173, 178]), the shell thickness of the sample performed with 5 cycles of

the c-ALD process is 1.55 nm, which is close to the measured value (1.14 nm). The slight difference can be attributed to the experimental errors.
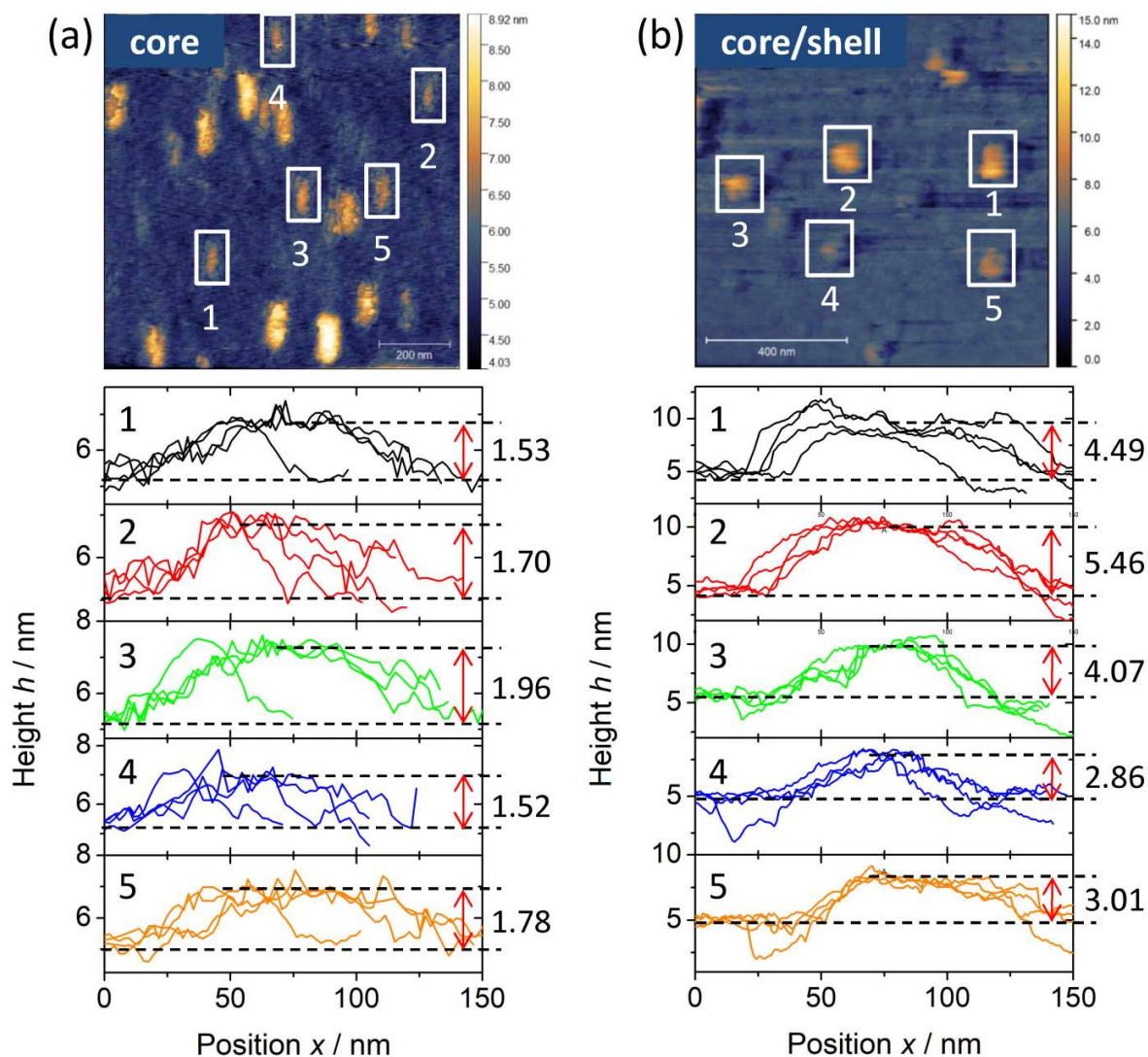
Figure 4-11. AFM images of (a) ZnSe:Mn NPLs and (b) ZnSe:Mn/ZnS NPLs. Bottom: The height determination of the NPLs from the cross sections of individual NPL circled by the white rectangles.

To study the influence of the ZnS shell on the optical properties of ZnSe:Mn/ZnS core/shell NPLs, a series of samples with increasing ZnS ML were prepared. Compared to the core NPLs, the absorbance spectra of the core/shell NPLs display enhanced

absorption in the UV range between 250 and 300 nm (see Figure 4-12a), which could be due to the absorption of ZnS.
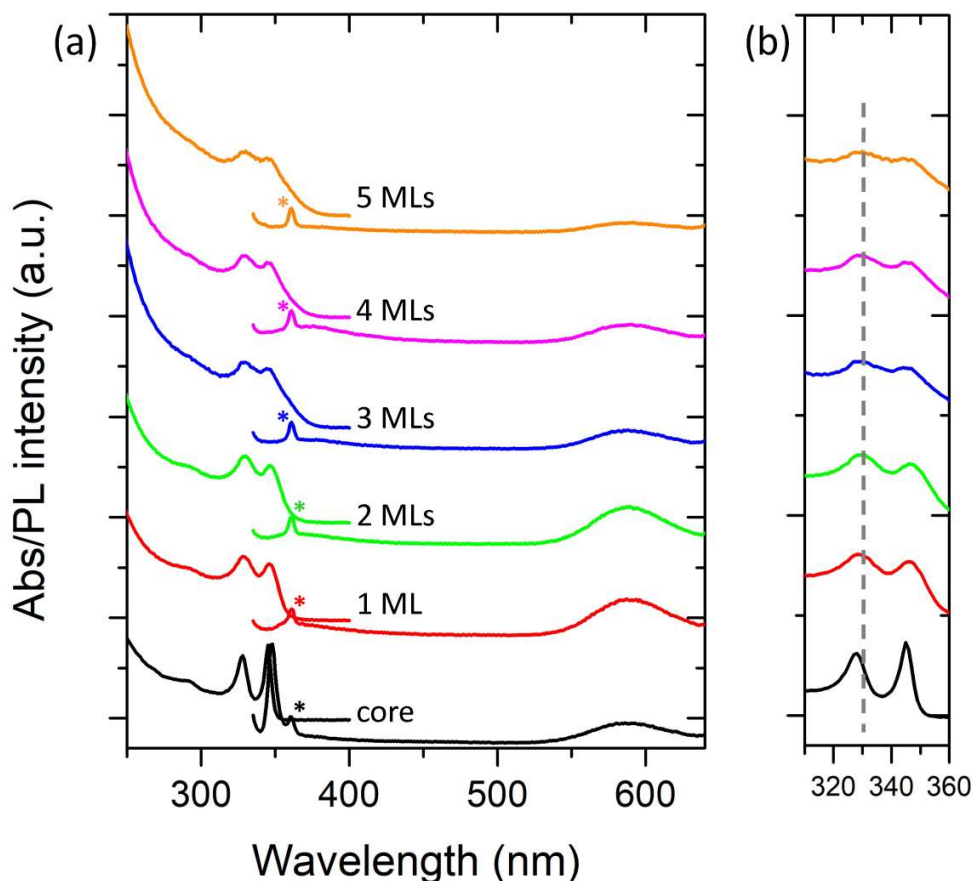
Figure 4-12. (a) UV−vis absorbance and PL spectra of ZnSe:Mn NPLs and ZnSe:Mn/ZnS core/shell NPLs with different ZnS MLs. (b) Zoomed-in UV−vis absorbance spectra. The scattering of the solvent (hexane) Raman peaks (marked with an asterisk) is also detected. The spectra are vertically shifted for clarity.

With increasing number of the ZnS-shell ML, the absorption in the UV range increases gradually, followed by a red-shift of the two main absorption peaks (see Figure 4-12b). Such a small red-shift in absorption was also observed in the previous report on the core/shell ZnSe/ZnS QDs, which is regarded as a sign of the formation of a shell.[60, 164, 179] This is consistent with the AFM results. Looking at the PL spectra, it is surprising to find that the BE emission of the host disappeared and only the Mn^{2+} emission was detectable

after the deposition of ZnS. The disappearance of the BE emission is probably due to the surface defects, considering the rough edges of the core/shell NPLs. In addition, the PLQY of core/shell NPLs was still relatively low (< 0.2%). One reason could be the inhomogeneous ZnS shell with low crystallinity since c-ALD was conducted at room temperature. To address this issue, post-treatment such as annealing is required. Recently, Dubertret and co-workers[176] found the same issue in the fabrication of the CdSe/CdZnS core/shell NPLs. The as-synthesized CdSe/CdZnS NPLs were then annealed at 300 °C in trioctylamine in the presence of an excess of cadmium oleate. After this treatment, the CdZnS shell became smooth and homogeneous.

Although the Mn^{2+} PLQY was not improved after the growth of the ZnS shell, the Mn^{2+} PL kinetics may be changed. To verify this, TRPL measurements were performed. Figure 4-13 (a−b) shows a significant increase in the Mn^{2+} PL average lifetime from 27 μs to 200 μs upon deposition of the first ML of ZnS. This change suggests that the Mn^{2+} PL kinetics were highly influenced by the ZnS shell. With increasing thickness of the ZnS shell, the Mn^{2+} PL average lifetime remains almost unchanged.
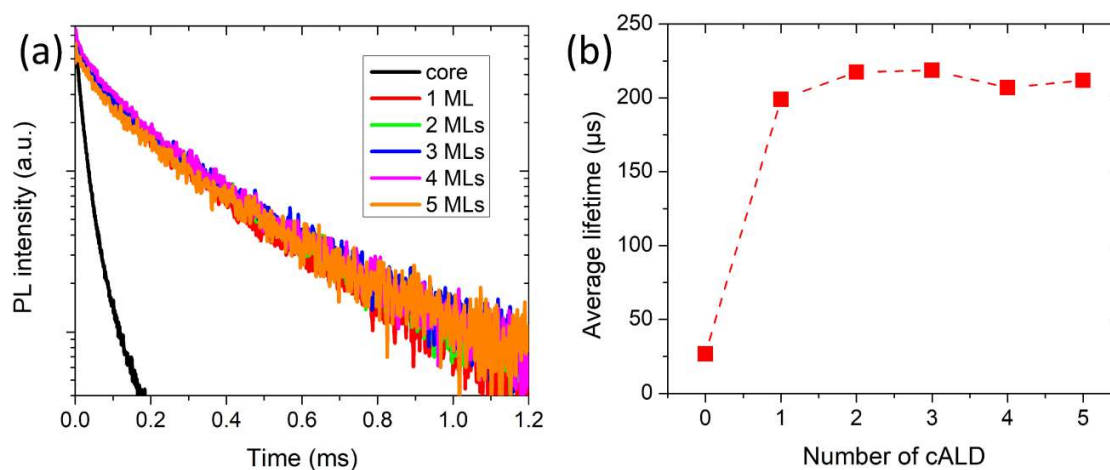
Figure 4-13. (a) The Mn^{2+} PL lifetime of the ZnSe:Mn/ZnS core/shell NPLs as a function of the layer number of the ZnS shell. (b) The average lifetime of the NPLs as a function of the layer number of the ZnS shell.

It is well-known that the Mn^{2+} PL decay lifetime from $^4T_1$–$^6A_1$ transitions is proportional to the Mn^{2+}–Mn^{2+} distance.[80, 137] For a given Mn^{2+}-doped system, there are two ways to increase the Mn^{2+}–Mn^{2+} distance and thereby leading to a long Mn^{2+} PL decay lifetime: (1) decrease the Mn^{2+} concentration and (2) place Mn^{2+} ions further away from each other. Considering that no additional Mn^{2+} ions were added during the formation of the ZnS shell, the Mn^{2+} concentration in the NPLs should remain unchanged before and after the ZnS growth. Thus the increase in Mn^{2+} PL decay lifetime is likely due to the increase in Mn^{2+}–Mn^{2+} distance. Recently, Zheng's group[140, 180] showed that interface between the core and the shell can create a driving force to trigger migration of Mn^{2+} ions from the core to the interface. Here, the migration of Mn^{2+} ions, which leads to an increase in the Mn^{2+}–Mn^{2+} distance, is considered as a possible reason for the increase in PL decay lifetime of Mn^{2+}-doped core/shell structures.

4.3 Conclusions

In this work, atomically precise ZnSe NPLs with a sharp BE emission were successfully synthesized by adapting the soft-template-guided approach. The subsequent introduction of Mn^{2+} ions into the ZnSe endows the doped NPLs with dual emission. The coupling between excitons and Mn^{2+} ions was investigated in detail using spectroscopic characterization. By varying the concentration of Mn^{2+} ions, the intensity ratio of the BE and Mn^{2+} emission can be easily tuned. To improve the optical properties, ZnS shells were successfully grown on the ZnSe:Mn NPLs through the c-ALD method. The formation of the ZnS shell is evidenced by the TEM, UV−vis absorbance, and AFM measurements. After the growth of the ZnS shell, the Mn^{2+} emission kinetics is found to be significantly changed. The decay of Mn^{2+} PL becomes more homogeneous, accompanied by a dramatical increase in lifetime from tens of μs to hundreds of μs when the ZnS shell grows on the ZnSe:Mn NPLs.

4.4 Experimental Section

4.4.1 Chemicals

Zinc chloride (97+%), octylamine (OTA, 99+%), and methanol (99.8%) were purchased from Acros. Manganese (II) acetate (98%, $Mn(OAc)_2$), selenium powder,

oleylamine (OAm, 70%), trioctylphosphine (TOP, 97%), formamide (99+%), N-methylformamide (NMF, 99%), and ammonium sulfide ($(NH_4)_2S$, 20 wt% in H_2O) were ordered from Sigma-Aldrich. Toluene (99.5%), isopropanol (99.7%), and hexane (95%) were purchased from VWR. Acetone (99%) was purchased from Th. Geyer Chemicals. All chemicals were used without further purification.

4.4.2 Synthesis of ZnSe Nanoplatelets

Standard Synthetic Procedure for ZnSe NPLs. In a three-necked flask equipped with a septum and a thermocouple in a glass mantle, 0.15 mmol (20.4 mg) of $ZnCl_2$ and 0.45 mmol (35.5 mg) of selenium powder were dissolved in a mixture of 10 mL of OAm and 5 mL of OTA. The mixed solution was bubbled with nitrogen at 100 °C for 30 min under vigorous stirring. Afterwards, the reaction solution was heated to 170 °C for 6 h with magnetic stirring under nitrogen flow. After the reaction, the solution was naturally cooled down by removal of the heating mantle. When the temperature reached 100 °C, ~2 mL of TOP was added into the flask to remove unreacted selenium. The resulting NCs were purified as follows: (1) 15 mL of reaction solution was mixed with 5 mL of acetone and 5 mL of isopropanol. (2) The mixture was shaken well and centrifuged for 10 min at 9000 rpm. (3) The supernatant was discarded, and the precipitation was dispersed into 3 mL of hexane or toluene for further characterization.

4.4.3 Synthesis of ZnSe:Mn Nanoplatelets

Standard Synthetic Procedure for ZnSe:Mn NPLs. In a three-necked flask equipped with a septum and a thermocouple in a glass mantle, 0.15 mmol (20.4 mg) of $ZnCl_2$, 0.45 mmol (35.5 mg) of selenium powder, and a certain amount of $Mn(OAc)_2$ were dissolved in a mixture of 10 mL of OAm and 5 mL of OTA. The mixed solution was bubbled with nitrogen at 100 °C for 30 min under vigorous stirring. Afterwards, the reaction solution was heated to 170 °C for 6 h with magnetic stirring under nitrogen flow. After reaction, the solution was naturally cooled down by removal of the heating mantle. When the temperature reached 100 °C, ~2 mL of TOP was added into the flask to remove unreacted selenium. The resulting NCs were purified as follows: (1) 15 mL of reaction solution was mixed with 5 mL of acetone and 5 mL of isopropanol. (2) The mixture was

shaken well and centrifuged for 10 min at 9000 rpm. (3) The supernatant was discarded, and the precipitation was dispersed into 5 mL of hexane for further preparation of ZnSe:Mn/ZnS core/shell NPLs.

Synthesis of ZnSe:Mn with Variable Mn^{2+} Concentrations. For the synthesis of ZnSe:Mn NPLs with different Mn^{2+} concentrations, the amount of $Mn(OAc)_2$ was varied while the amounts of $ZnCl_2$ and selenium powder in the initial mixture were fixed.

4.4.4 Synthesis of ZnSe:Mn/ZnS Core/Shell Nanoplatelets

Standard Synthetic Procedure for ZnSe:Mn/ZnS Core/Shell NPLs. 200 μL of ZnSe:Mn NPLs was purified by centrifugation, and the precipitation was then re-dispersed into 1 mL of hexane in a 5 mL glass vial. 1 mL of NMF and 22 μL of aqueous $(NH_4)_2S$ solution (20 wt% in H_2O) were added into the vial. The two-phase mixture was stirred vigorously until complete phase transfer of NPLs from hexane to NMF. The upper phase (hexane) was discarded. The lower phase (NMF) containing S^{2-}-coated NPLs was rinsed two times with hexane, followed by centrifugation and re-dispersion in 1 mL of NMF. To deposit a layer of Zn^{2+} ion, 120 μL of 0.1 M $ZnCl_2$ solution in formamide was added, and the mixture was stirred vigorously for 30 s. Finally, the NPLs were purified by centrifugation and re-dispersed in 1 mL of NMF. The above procedure was repeated until the desired number of layers was obtained.

4.4.5 Characterizations

TEM. TEM images were taken by using a JEOL Jem-1011 microscope at an acceleration voltage of 100 kV. Samples for the TEM analysis were prepared by drop-casting 10 μL of the dilute NC dispersion onto carbon-coated copper grids. HRTEM images and EDX spectra were obtained with a Philips CM 300 UT microscope operated at an acceleration voltage of 200 kV.

XRD. XRD measurements were performed with a Philips X'Pert PRO MPD diffractometer with monochromatic X-ray radiation from a copper anode with a wavelength of 0.154 nm (Cu Kα). Samples for the XRD analysis were prepared by drop-

casting a few µL of the concentrated NC solution onto silicon wafer substrates with subsequent solvent evaporation.

UV−vis Absorbance and PL Spectra. UV−vis absorbance and steady-state PL spectra were obtained with a PerkinElmer Lambda 25 two-beam spectrometer and a Horiba Fluoromax-4 spectrometer, respectively. TRPL measurements were performed with Picoquant FluoTime 300 fluorescence spectrometer. Samples were prepared by adding a few µL of the NC solution into 3 mL of hexane in quartz vessels with an optical path length of 10 mm.

ICP-OES. The Mn^{2+} concentration in NPLs was determined via ICP-OES (type: ARCOS) produced by Fa. Spectro. Samples for the ICP-OES analysis were prepared with three steps: (1) 2 mL of the concentrated NC solution was pipetted into a 25 mL beaker and evaporated at room temperature. (2) The dried sample was dissolved in 4 mL of concentrated HNO_3 at 160 °C. (3) The mixed solution was diluted in a 25 mL volumetric flask.

AFM. AFM from JPK Instruments was used to determine the thickness of NPLs. Data processing was done with the software package *Gwyddion*. The samples were prepared by drop-casting a diluted NPL suspension on a silicon wafer.

CHAPTER 5

Conclusions and Outlook

5.1 Conclusions

In the first part of the project, a simple and effective colloidal method for the preparation of 2D ZnS NPLs was developed. This method can be applied for the synthesis of layered and non-layered 2D nanomaterials. The soft-template-guided formation mechanism for the ZnS NPLs was studied using TEM, XRD, and ^{1}H NMR and confirmed in the OAm/OTA/Zn^{2+} precipitation experiment. The synthesized ZnS NPLs exhibit not only distinct absorption features, but also a noticeable excitonic emission that is not seen in previous reports. The observed absorption bands at 4.38, 4.8, 5.62, and 5.78 eV reveal the genuine 2D nature of the obtained NPLs, which can be assigned to $h_{0,1,2}-e_0$, h_4-e_1, h_1-e_3, and h_5-e_2 transitions, respectively. Moreover, it is found that the amount of sulfur and volume ratio between amine ligands can significantly influence the shape and phase of ZnS NCs. By changing the amount of sulfur, a simultaneous shape/phase transformation between WZ-ZnS NPLs and ZB-ZnS NRs occurs at a relatively low temperature (150 °C).

The ZnS NPLs synthesized in Chapter 2 represent an attractive choice as the matrix for transition metal ions due to their flat and uniform structure, which prompts us to dope such NPLs with Mn^{2+} ions. The experimental results show that the recipe of ZnS NPLs can be extended to prepare the ZnS:Mn NPLs without changing the shape and phase of the products. In addition to the excitonic emission in the UV range, the resulting ZnS:Mn NPLs exhibit an orange emission originating from Mn^{2+} $^4T_1-^6A_1$ transitions. It is noted that both the dopant and the host optical properties (*e.g.* PL intensity ratio, lifetime, and PLQY) are highly dependent on the Mn^{2+} concentration. The connection between Mn^{2+} species and Mn^{2+} PL kinetics were also systematically investigated using TRPL and DFT-based calculations. It appears that Mn^{2+} ions with less coupling have a longer PL lifetime and tend to emit at shorter wavelengths. Additionally, it is found that the surface of ZnS:Mn NPLs is a critical and limiting factor for the effective energy conversion. By passivating the surface with zinc-containing ligands, the PLQY of ZnS:Mn NPLs can be substantially improved.

Based on that, preparation of type-I ZnSe:Mn/ZnS core/shell NPLs were considered. The goal is to improve their optical properties (*e.g.* PLQY and lifetime) and to enhance the environmental stability. The experience in the synthesis of ZnS:Mn NPLs help us to design a synthetic protocol for ZnSe:Mn NPLs. The result appears that a higher temperature (170 °C) is

required for the preparation of the well-separated ZnSe:Mn NPLs in comparison to that of ZnS:Mn NPLs (150 °C). To remove impurities (*e.g.* unreacted Se powder), it is necessary to add TOP (cosolvent) into the reaction solution during the cooling. The sample (8% in the synthesis) with a relatively high PLQY was used as "seeds" for the ZnS shell growth. Considering the poor thermal stability of NPLs, a moderate method named c-ALD was adopted to synthesize the core/shell NPLs. The formation of the ZnS shell was evidenced by TEM and AFM measurements. Although the PLQY of core/shell NPLs is still low, the shell growth is found to extend the PL lifetime from tens of microseconds to hundreds of microseconds. To improve the PLQY, several optimizations such as annealing via physical and chemical methods are proposed for future studies. Finally, the successful preparation of a series of Zn chalcogenide NPLs (ZnS, ZnSe, and ZnSe/ZnS) shown in the dissertation provides general guidelines for the design of other non-layered 2D semiconductor nanomaterials.

5.2 Outlook

The research of 2D semiconductor NPLs and their heterostructures (*e.g.* doping, core/shell, and core/crown) is still in its infancy. Thus, many aspects need to be addressed in the future to meet the increasing demands of practical applications. First of all, in addition to Cd-based NPLs, the research on other composition NPLs is still lacking. This leads to immature synthetic strategies and unclear formation mechanisms. More efforts should be made to prepare diverse NPLs. Second, it is well-known that the optical properties of NPLs are mainly governed by their thickness. Thus, precise control over the thickness of NPLs is very significant. For example, the emission spectrum of CdSe NPLs can be tuned in a wide range from 460 to 625 nm by changing their thickness.[43, 56] However, the zinc-containing NPLs (ZnS and ZnSe) presented here exhibit spectrally fixed PL due to the lack of thickness tunability. Future work should focus on developing new recipes to achieve thickness control of NPLs. Third, because of the large lateral dimension and ultrathin thickness, NPLs tend to fold and stack during synthesis, which is detrimental to their properties. For instance, it has been observed that the stacking of NPLs results in a low energy emission peak.[181-182] Further research on the stabilization of NPLs is desired.

For doping of NPLs, the "self-purification" issue induced by the ultra-small volume of NPLs is not well resolved. This phenomenon is also observed in the ZnS:Mn NPLs in Chapter 3.

Besides, it is still difficult to dope NPLs with impurities homogeneously and controllably. Further studies on enhanced control over the dopant position are required.

Unlike the core/shell QDs, most core/shell NPLs are prepared at a low temperature (or room temperature) due to the poor thermal stability of NPLs, and these core/shell NPLs generally exhibit a very low PLQY. In future studies, high-temperature based approaches need to be developed. Second, NPLs with highly anisotropic morphologies have large energy differences between basal and side facets, which commonly results in inhomogeneous or selective deposition of a shell. The low-quality shell can generate structural defects (*e.g.* grain boundaries, impurities, and dislocations), which leads to reduced optical/electronic performance. Therefore, an advanced control over the shell growth on NPLs is highly demanded.

Finally, thanks to the distinct optoelectronic properties, quasi-2D NPLs, as well as their heterostructures (*e.g.* doping, core/shell, and core/crown), have shown great potential in many fields. For example, the extremely narrow emission performance of NPLs makes them attractive for applications in lasing and displays. Because of the large absorption cross sections, NPLs shows promising for energy conversion and storage. Moverover, core/shell NPLs with good stability are ideal materials for lighting devices. However, the development of the NPL-based technology is relatively slow in comparion to QDs. Thus, more attention should be paid to the use of NPLs in the future.

Bibliography

1.   Reiss, P.; Carriere, M.; Lincheneau, C.; Vaure, L.; Tamang, S. Synthesis of Semiconductor Nanocrystals, Focusing on Nontoxic and Earth-Abundant Materials. *Chem. Rev.* **2016,** *116*, 10731-10819.

2.   Akkerman, Q. A. Perovskite Nanocrystals: A New Age of Semiconductuctive Nanocrystals. *Doctoral thesis* **2018**.

3.   Bera, D.; Qian, L.; Holloway, P. H. Semiconducting Quantum Dots for Bioimaging. *Informa Heathcare: New York, NY, USA* **2009,** *191*.

4.   Murray, C. B.; Norris, D. J.; Bawendi, M. G. Synthesis and characterization of nearly monodisperse CdE (E = sulfur, selenium, tellurium) semiconductor nanocrystallites. *J. Am. Che. Soc.* **1993,** *115*, 8706-8715.

5.   Chen, D.; Wang, A.; Buntine, M. A.; Jia, G. Recent Advances in Zinc-Containing Colloidal Semiconductor Nanocrystals for Optoelectronic and Energy Conversion Applications. *ChemElectroChem* **2019,** *6*, 4709-4724.

6.   Buhro, W. E.; Colvin, V. L. Semiconductor nanocrystals: Shape matters. *Nat. Mater.* **2003,** *2*, 138-139.

7.   Varoon, K.; Zhang, X.; Elyassi, B.; Brewer, D. D.; Gettel, M.; Kumar, S.; Lee, J. A.; Maheshwari, S.; Mittal, A.; Sung, C. Y.; Cococcioni, M.; Francis, L. F.; McCormick, A. V.; Mkhoyan, K. A.; Tsapatsis, M. Dispersible exfoliated zeolite nanosheets and their application as a selective membrane. *Science* **2011,** *334*, 72-75.

8.   Jariwala, D.; Sangwan, V. K.; Lauhon, L. J.; Marks, T. J.; Hersam, M. C. Emerging device applications for semiconducting two-dimensional transition metal dichalcogenides. *ACS nano* **2014,** *8*, 1102-1120.

9.   Smith, R. J.; King, P. J.; Lotya, M.; Wirtz, C.; Khan, U.; De, S.; O'Neill, A.; Duesberg, G. S.; Grunlan, J. C.; Moriarty, G.; Chen, J.; Wang, J.; Minett, A. I.; Nicolosi, V.; Coleman, J. N. Large-Scale Exfoliation of Inorganic Layered Compounds in Aqueous Surfactant Solutions. *Adv. Mater.* **2011,** *23*, 3944-3948.

Bibliography

10.   Han, J. H.; Lee, S.; Cheon, J. Synthesis and structural transformations of colloidal 2D layered metal chalcogenide nanocrystals. *Chem. Soc. Rev.* **2013,** *42*, 2581-2591.

11.   Acharya, S.; Sarma, D. D.; Golan, Y.; Sengupta, S.; Ariga, K. Shape-dependent confinement in ultrasmall zero-, one-, and two-dimensional PbS nanostructures. *J. Am. Chem. Soc.* **2009,** *131*, 11282-11283.

12.   Polte, J. Fundamental growth principles of colloidal metal nanoparticles – a new perspective. *CrystEngComm* **2015,** *17*, 6809-6830.

13.   Thanh, N. T.; Maclean, N.; Mahiddine, S. Mechanisms of nucleation and growth of nanoparticles in solution. *Chem. Rev.* **2014,** *114*, 7610-7630.

14.   Sugimoto, T. Monodispersed particles. *Elsevier: Amsterdam* **2001**.

15.   Kwon, S. G.; Hyeon, T. Formation mechanisms of uniform nanocrystals via hot-injection and heat-up methods. *Small* **2011,** *7*, 2685-2702.

16.   LaMer, V. K.; Dinegar, R. H. Theory, Production and Mechanism of Formation of Monodispersed Hydrosols. *J. Am. Chem. Soc.* **1950,** *72*, 4847-4854.

17.   Sugimoto, T. Preparation of monodispersed colloidal particles. *Adv. Colloid Interfac. Sci.* **1987,** *28*, 65-108.

18.   Ostwald, W. Studien über die Bildung und Umwandlung fester Körper. *Zeitschrift für Physikalische Chemie* **1897,** *22U*, 289-330.

19.   Ostwald, W. Über die vermeintliche Isomerie des roten und gelben Quecksilberoxyds und die Oberflächenspannung fester Körper. *Zeitschrift für Physikalische Chemie* **1900,** *34U*, 495–503.

20.   Voorhees, P. W. The theory of Ostwald ripening. *J. Stat. Phys.* **1985,** *38*, 231–252.

21.   Richards, V. N.; Rath, N. P.; Buhro, W. E. Pathway from a Molecular Precursor to Silver Nanoparticles: The Prominent Role of Aggregative Growth. *Chem. Mater.* **2010,** *22*, 3556-3567.

22.   Penn, R. L.; Banfield, J. F. Imperfect oriented attachment: dislocation generation in defect-free nanocrystals. *Science* **1998,** *281*, 969-971.

23.   Shields, S. P.; Richards, V. N.; Buhro, W. E. Nucleation Control of Size and Dispersity in Aggregative Nanoparticle Growth. A Study of the Coarsening Kinetics of Thiolate-Capped Gold Nanocrystals. *Chem. Mater.* **2010,** *22*, 3212-3225.

24.   Wang, F.; Richards, V. N.; Shields, S. P.; Buhro, W. E. Kinetics and Mechanisms of Aggregative Nanocrystal Growth. *Chem. Mater.* **2013,** *26*, 5-21.

25.   Yu, J. H.; Joo, J.; Park, H. M.; Baik, S. I.; Kim, Y. W.; Kim, S. C.; Hyeon, T. Synthesis of quantum-sized cubic ZnS nanorods by the oriented attachment mechanism. *J. Am. Chem. Soc.* **2005,** *127*, 5662-5670.

26.   Schliehe, C.; Juarez, B. H.; Pelletier, M.; Jander, S.; Greshnykh, D.; Nagel, M.; Meyer, A.; Foerster, S.; Kornowski, A.; Klinke, C.; Weller, H. Ultrathin PbS sheets by two-dimensional oriented attachment. *Science* **2010,** *329*, 550-553.

27.   Sarkar, S.; Acharya, S.; Chakraborty, A.; Pradhan, N. Zinc Blende 0D Quantum Dots to Wurtzite 1D Quantum Wires: The Oriented Attachment and Phase Change in ZnSe Nanostructures. *J. Phys. Chem. Lett.* **2013,** *4*, 3292-3297.

28.   Li, D.; Nielsen, M. H.; Lee, J. R.; Frandsen, C.; Banfield, J. F.; De Yoreo, J. J. Direction-specific interactions control crystal growth by oriented attachment. *Science* **2012,** *336*, 1014-1018.

29.   Zhang, J.; Huang, F.; Lin, Z. Progress of nanocrystalline growth kinetics based on oriented attachment. *Nanoscale* **2010,** *2*, 18-34.

30.   Watzky, M. A.; Finke, R. G. Nanocluster Size-Control and "Magic Number" Investigations. Experimental Tests of the "Living-Metal Polymer" Concept and of Mechanism-Based Size-Control Predictions Leading to the Syntheses of Iridium(0) Nanoclusters Centering about Four Sequential Magic Numbers†. *Chem. Mater.* **1997,** *9*, 3083-3095.

31.   Watzky, M. A.; Finke, R. G. Transition Metal Nanocluster Formation Kinetic and Mechanistic Studies. A New Mechanism When Hydrogen Is the Reductant: Slow, Continuous Nucleation and Fast Autocatalytic Surface Growth. *J. Am. Chem. Soc.* **1997,** *119*, 10382-10400.

32.   Perala, S. R.; Kumar, S. On the two-step mechanism for synthesis of transition-metal nanoparticles. *Langmuir : the ACS journal of surfaces and colloids* **2014,** *30*, 12703-12711.

33.   Peng, Z. A.; Peng, X. Mechanisms of the Shape Evolution of CdSe Nanocrystals. *J. Am. Chem. Soc.* **2001,** *123*, 1389-1395.

34.   Peng, X.; Manna, L.; Yang, W.; Wickham, J.; Scher, E.; Kadavanich, A.; Alivisatos, A. P. Shape control of CdSe nanocrystals. *Nature* **2000,** *404*, 59-61.

35.   Gibbs, J. W. On the Equilibrium of Heterogeneous Substances. *Am. J. Sci.* **1878,** *s3-16*, 441-458.

36.   Wulff, G. Zur Frage Der Geschwindigkeit Des Wachsthums Und Der Auflösung Der Krystallflächen Wachsthums Und Der Auflösung Der Krystallflächen. *Z. Kristallogr. - Cryst. Mater.* **1901,** *34*, 449-530.

37.   de Leeuw, N. H.; Parker, S. C. Surface Structure and Morphology of Calcium Carbonate Polymorphs Calcite, Aragonite, and Vaterite: An Atomistic Approach. *J. Phys. Chem. B* **1998,** *102*, 2914-2922.

38.   Barmparis, G. D.; Lodziana, Z.; Lopez, N.; Remediakis, I. N. Nanoparticle shapes by using Wulff constructions and first-principles calculations. *Beilstein J. Nanotechnol.* **2015,** *6*, 361-368.

39.   Nasilowski, M.; Mahler, B.; Lhuillier, E.; Ithurria, S.; Dubertret, B. Two-Dimensional Colloidal Nanocrystals. *Chem. Rev.* **2016,** *116*, 10934-10982.

40.   Peng, X. Mechanisms for the Shape-Control and Shape-Evolution of Colloidal Semiconductor Nanocrystals. *Adv. Mater.* **2003,** *15*, 459-463.

41.   Peng, Z. A.; Peng, X. Nearly monodisperse and shape-controlled CdSe nanocrystals via alternative routes: nucleation and growth. *J. Am. Chem. Soc.* **2002,** *124*, 3343-3353.

42.   Tan, C.; Cao, X.; Wu, X. J.; He, Q.; Yang, J.; Zhang, X.; Chen, J.; Zhao, W.; Han, S.; Nam, G. H.; Sindoro, M.; Zhang, H. Recent Advances in Ultrathin Two-Dimensional Nanomaterials. *Chem. Rev.* **2017,** *117*, 6225-6331.

43.   Ithurria, S.; Dubertret, B. Quasi 2D colloidal CdSe platelets with thicknesses controlled at the atomic level. *J. Am. Chem. Soc.* **2008,** *130*, 16504-16505.

44.   Son, J. S.; Wen, X. D.; Joo, J.; Chae, J.; Baek, S. I.; Park, K.; Kim, J. H.; An, K.; Yu, J. H.; Kwon, S. G.; Choi, S. H.; Wang, Z.; Kim, Y. W.; Kuk, Y.; Hoffmann, R.; Hyeon, T. Large-scale soft colloidal template synthesis of 1.4 nm thick CdSe nanosheets. *Angew. Chem. Int. Ed.* **2009,** *48*, 6861-6864.

45.   She, C.; Fedin, I.; Dolzhnikov, D. S.; Demortiere, A.; Schaller, R. D.; Pelton, M.; Talapin, D. V. Low-threshold stimulated emission using colloidal quantum wells. *Nano Lett.* **2014,** *14*, 2772-2777.

46.   Chen, Z.; Nadal, B.; Mahler, B.; Aubin, H.; Dubertret, B. Quasi-2D Colloidal Semiconductor Nanoplatelets for Narrow Electroluminescence. *Adv. Funct. Mater.* **2014,** *24*, 295-302.

47.   Wu, M.; Ha, S. T.; Shendre, S.; Durmusoglu, E. G.; Koh, W. K.; Abujetas, D. R.; Sanchez-Gil, J. A.; Paniagua-Dominguez, R.; Demir, H. V.; Kuznetsov, A. I. Room-Temperature Lasing in Colloidal Nanoplatelets via Mie-Resonant Bound States in the Continuum. *Nano Lett.* **2020,** *20*, 6005-6011.

48.   Ithurria, S.; Tessier, M. D.; Mahler, B.; Lobo, R. P.; Dubertret, B.; Efros, A. L. Colloidal nanoplatelets with two-dimensional electronic structure. *Nat. Mater.* **2011,** *10*, 936-941.

49.   Huo, Z.; Tsung, C. K.; Huang, W.; Zhang, X.; Yang, P. Sub-two nanometer single crystal Au nanowires. *Nano Lett.* **2008,** *8*, 2041-2044.

50.   Wang, Y.; Liu, Y. H.; Zhang, Y.; Wang, F.; Kowalski, P. J.; Rohrs, H. W.; Loomis, R. A.; Gross, M. L.; Buhro, W. E. Isolation of the magic-size CdSe nanoclusters [(CdSe)$_{13}$(n-octylamine)$_{13}$] and [(CdSe)$_{13}$(oleylamine)$_{13}$]. *Angew. Chem. Int. Ed.* **2012,** *51*, 6154-6157.

51.   Joo, J.; Son, J. S.; Kwon, S. G.; Yu, J. H.; Hyeon, T. Low-temperature solution-phase synthesis of quantum well structured CdSe nanoribbons. *J. Am. Chem. Soc.* **2006,** *128*, 5632-5633.

52.   Son, J. S.; Park, K.; Kwon, S. G.; Yang, J.; Choi, M. K.; Kim, J.; Yu, J. H.; Joo, J.; Hyeon, T. Dimension-controlled synthesis of CdS nanocrystals: from 0D quantum dots to 2D nanoplates. *Small* **2012,** *8*, 2394-2402.

53.   Son, J. S.; Yu, J. H.; Kwon, S. G.; Lee, J.; Joo, J.; Hyeon, T. Colloidal synthesis of ultrathin two-dimensional semiconductor nanocrystals. *Adv. Mater.* **2011,** *23*, 3214-3219.

54.   Zhang, J.; Sun, Y.; Ye, S.; Song, J.; Qu, J. Heterostructures in Two-Dimensional CdSe Nanoplatelets: Synthesis, Optical Properties, and Applications. *Chem. Mater.* **2020,** *32*, 9490-9507.

55.   Bouet, C.; Mahler, B.; Nadal, B.; Abecassis, B.; Tessier, M. D.; Ithurria, S.; Xu, X.; Dubertret, B. Two-Dimensional Growth of CdSe Nanocrystals, from Nanoplatelets to Nanosheets. *Chem. Mater.* **2013,** *25*, 639-645.

56.   Christodoulou, S.; Climente, J. I.; Planelles, J.; Brescia, R.; Prato, M.; Martin-Garcia, B.; Khan, A. H.; Moreels, I. Chloride-Induced Thickness Control in CdSe Nanoplatelets. *Nano Lett.* **2018,** *18*, 6248-6254.

57.   Ithurria, S.; Bousquet, G.; Dubertret, B. Continuous transition from 3D to 1D confinement observed during the formation of CdSe nanoplatelets. *J. Am. Chem. Soc.* **2011,** *133*, 3070-3077.

58.   Kunneman, L. T.; Tessier, M. D.; Heuclin, H.; Dubertret, B.; Aulin, Y. V.; Grozema, F. C.; Schins, J. M.; Siebbeles, L. D. A. Bimolecular Auger Recombination of Electron–Hole Pairs in Two-Dimensional CdSe and CdSe/CdZnS Core/Shell Nanoplatelets. *J. Phys. Chem. Lett.* **2013,** *4*, 3574-3578.

59.   Zhang, F.; Wang, S.; Wang, L.; Lin, Q.; Shen, H.; Cao, W.; Yang, C.; Wang, H.; Yu, L.; Du, Z.; Xue, J.; Li, L. S. Super color purity green quantum dot light-emitting diodes fabricated by using CdSe/CdS nanoplatelets. *Nanoscale* **2016,** *8*, 12182-12188.

60.   Polovitsyn, A.; Dang, Z.; Movilla, J. L.; Martín-García, B.; Khan, A. H.; Bertrand, G. H. V.; Brescia, R.; Moreels, I. Synthesis of Air-Stable CdSe/ZnS Core–Shell Nanoplatelets with Tunable Emission Wavelength. *Chem. Mater.* **2017,** *29*, 5671-5680.

61.   Reiss, P.; Protiere, M.; Li, L. Core/Shell semiconductor nanocrystals. *Small* **2009,** *5*, 154-168.

62.   Rossinelli, A. A.; Riedinger, A.; Marques-Gallego, P.; Knusel, P. N.; Antolinez, F. V.; Norris, D. J. High-temperature growth of thick-shell CdSe/CdS core/shell nanoplatelets. *Chem. Commun.* **2017,** *53*, 9938-9941.

63.   Rossinelli, A. A.; Rojo, H.; Mule, A. S.; Aellen, M.; Cocina, A.; De Leo, E.; Schäublin, R.; Norris, D. J. Compositional Grading for Efficient and Narrowband Emission in CdSe-Based Core/Shell Nanoplatelets. *Chem. Mater.* **2019,** *31*, 9567-9578.

64.   Ott, F. D.; Riedinger, A.; Ochsenbein, D. R.; Knusel, P. N.; Erwin, S. C.; Mazzotti, M.; Norris, D. J. Ripening of Semiconductor Nanoplatelets. *Nano Lett.* **2017,** *17*, 6870-6877.

65.   Ithurria, S.; Talapin, D. V. Colloidal atomic layer deposition (c-ALD) using self-limiting reactions at nanocrystal surface coupled to phase transfer between polar and nonpolar media. *J. Am. Chem. Soc.* **2012,** *134*, 18585-18590.

66.   Delikanli, S.; Akgul, M. Z.; Murphy, J. R.; Barman, B.; Tsai, Y.; Scrace, T.; Zhang, P.; Bozok, B.; Hernandez-Martinez, P. L.; Christodoulides, J.; Cartwright, A. N.; Petrou, A.; Demir, H. V. Mn^{2+}-Doped CdSe/CdS Core/Multishell Colloidal Quantum Wells Enabling Tunable Carrier-Dopant Exchange Interactions. *ACS nano* **2015,** *9*, 12473-12479.

67.   Shendre, S.; Delikanli, S.; Li, M.; Dede, D.; Pan, Z.; Ha, S. T.; Fu, Y. H.; Hernandez-Martinez, P. L.; Yu, J.; Erdem, O.; Kuznetsov, A. I.; Dang, C.; Sum, T. C.; Demir, H. V. Ultrahigh-efficiency aqueous flat nanocrystals of $CdSe/CdS@Cd_{1-x}Zn_xS$ colloidal core/crown@alloyed-shell quantum wells. *Nanoscale* **2018,** *11*, 301-310.

68.   Sahu, A.; Kang, M. S.; Kompch, A.; Notthoff, C.; Wills, A. W.; Deng, D.; Winterer, M.; Frisbie, C. D.; Norris, D. J. Electronic impurity doping in CdSe nanocrystals. *Nano Lett.* **2012,** *12*, 2587-2594.

69.   Beaulac, R.; Archer, P. I.; Ochsenbein, S. T.; Gamelin, D. R. Mn^{2+}-Doped CdSe Quantum Dots: New Inorganic Materials for Spin-Electronics and Spin-Photonics. *Adv. Funct. Mater.* **2008,** *18*, 3873-3891.

70.   Pradhan, N.; Battaglia, D. M.; Liu, Y.; Peng, X. Efficient, stable, small, and water-soluble doped ZnSe nanocrystal emitters as non-cadmium biomedical labels. *Nano Lett.* **2007,** *7*, 312-317.

71.   Norris, D. J.; Efros, A. L.; Erwin, S. C. Doped nanocrystals. *Science* **2008,** *319*, 1776-1779.

72.   Erwin, S. C.; Zu, L.; Haftel, M. I.; Efros, A. L.; Kennedy, T. A.; Norris, D. J. Doping semiconductor nanocrystals. *Nature* **2005,** *436*, 91-94.

73.   Beaulac, R.; Archer, P. I.; Liu, X.; Lee, S.; Salley, G. M.; Dobrowolska, M.; Furdyna, J. K.; Gamelin, D. R. Spin-polarizable excitonic luminescence in colloidal Mn2+-doped CdSe quantum dots. *Nano Lett.* **2008,** *8*, 1197-1201.

74.   Zhang, Z.; Li, D.; Xie, R.; Yang, W. Insights into the energy levels of semiconductor nanocrystals by a dopant approach. *Angew. Chem. Int. Ed.* **2013,** *52*, 5052-5055.

75.   Knowles, K. E.; Hartstein, K. H.; Kilburn, T. B.; Marchioro, A.; Nelson, H. D.; Whitham, P. J.; Gamelin, D. R. Luminescent Colloidal Semiconductor Nanocrystals Containing Copper: Synthesis, Photophysics, and Applications. *Chem. Rev.* **2016,** *116*, 10820-10851.

76.   Srivastava, B. B.; Jana, S.; Karan, N. S.; Paria, S.; Jana, N. R.; Sarma, D. D.; Pradhan, N. Highly Luminescent Mn-Doped ZnS Nanocrystals: Gram-Scale Synthesis. *J. Phys. Chem. Lett.* **2010,** *1*, 1454-1458.

77.   Kennedy, T. A.; Glaser, E. R.; Klein, P. B.; Bhargava, R. N. Symmetry and electronic structure of the Mn impurity in ZnS nanocrystals. *Phys. Rev. B* **1995,** *52*, 14356-14359.

78.   Jana, S.; Manna, G.; Srivastava, B. B.; Pradhan, N. Tuning the emission colors of semiconductor nanocrystals beyond their bandgap tunability: all in the dope. *Small* **2013,** *9*, 3753-3758.

79.   Dalpian, G. M.; Chelikowsky, J. R. Self-purification in semiconductor nanocrystals. *Phys. Rev. Lett.* **2006,** *96*, 226802.

80. Pu, C.; Ma, J.; Qin, H.; Yan, M.; Fu, T.; Niu, Y.; Yang, X.; Huang, Y.; Zhao, F.; Peng, X. Doped Semiconductor-Nanocrystal Emitters with Optimal Photoluminescence Decay Dynamics in Microsecond to Millisecond Range: Synthesis and Applications. *ACS Cent. Sci.* **2016,** *2*, 32-39.

81. Pradhan, N.; Goorskey, D.; Thessing, J.; Peng, X. An alternative of CdSe nanocrystal emitters: pure and tunable impurity emissions in ZnSe nanocrystals. *J. Am. Chem. Soc.* **2005,** *127*, 17586-17587.

82. Yang, Y.; Chen, O.; Angerhofer, A.; Cao, Y. C. Radial-position-controlled doping in CdS/ZnS core/shell nanocrystals. *J. Am. Chem. Soc.* **2006,** *128*, 12428-12429.

83. Lin, J.; Zhang, Q.; Wang, L.; Liu, X.; Yan, W.; Wu, T.; Bu, X.; Feng, P. Atomically precise doping of monomanganese ion into coreless supertetrahedral chalcogenide nanocluster inducing unusual red shift in Mn^{2+} emission. *J. Am. Chem. Soc.* **2014,** *136*, 4769-4779.

84. Novoselov, K. S.; Geim, A. K.; Morozov, S. V.; Jiang, D.; Zhang, Y.; Dubonos, S. V.; Grigorieva, I. V.; Firsov, A. A. Electric field effect in atomically thin carbon films. *Science* **2004,** *306*, 666-669.

85. Geim, A. K.; Novoselov, K. S. The rise of graphene. *Nat. Mater.* **2007,** *6*, 183-191.

86. Baghani, E.; O'Leary, S. K.; Fedin, I.; Talapin, D. V.; Pelton, M. Auger-Limited Carrier Recombination and Relaxation in CdSe Colloidal Quantum Wells. *J. Phys. Chem. Lett.* **2015,** *6*, 1032-1036.

87. Gerdes, F.; Navio, C.; Juarez, B. H.; Klinke, C. Size, Shape, and Phase Control in Ultrathin CdSe Nanosheets. *Nano Lett.* **2017,** *17*, 4165-4171.

88. Olutas, M.; Guzelturk, B.; Kelestemur, Y.; Yeltik, A.; Delikanli, S.; Demir, H. V. Lateral Size-Dependent Spontaneous and Stimulated Emission Properties in Colloidal CdSe Nanoplatelets. *ACS nano* **2015,** *9*, 5041-5050.

89. Karan, N. S.; Sarkar, S.; Sarma, D. D.; Kundu, P.; Ravishankar, N.; Pradhan, N. Thermally controlled cyclic insertion/ejection of dopant ions and reversible zinc blende/wurtzite phase changes in ZnS nanostructures. *J. Am. Chem. Soc.* **2011,** *133*, 1666-1669.

90.   Bouet, C.; Laufer, D.; Mahler, B.; Nadal, B.; Heuclin, H.; Pedetti, S.; Patriarche, G.; Dubertret, B. Synthesis of Zinc and Lead Chalcogenide Core and Core/Shell Nanoplatelets Using Sequential Cation Exchange Reactions. *Chem. Mater.* **2014,** *26*, 3002-3008.

91.   Buffard, A.; Nadal, B.; Heuclin, H.; Patriarche, G.; Dubertret, B. ZnS anisotropic nanocrystals using a one-pot low temperature synthesis. *New J. Chem.* **2015,** *39*, 90-93.

92.   Li, L.-s.; Hu, J.; Yang, W.; Alivisatos, A. P. Band Gap Variation of Size- and Shape-Controlled Colloidal CdSe Quantum Rods. *Nano Lett.* **2001,** *1*, 349-351.

93.   Zhang, Y.; Liu, W.; Wang, R. From ZnS nanoparticles, nanobelts, to nanotetrapods: the ethylenediamine modulated anisotropic growth of ZnS nanostructures. *Nanoscale* **2012,** *4*, 2394-2399.

94.   Thupakula, U.; Dalui, A.; Debangshi, A.; Bal, J. K.; Kumar, G. S.; Acharya, S. Shape dependent synthesis and field emission induced rectification in single ZnS nanocrystals. *ACS Appl. Mater. Interfaces* **2014,** *6*, 7856-7863.

95.   Baars, J.; Brandt, G. Structural Phase Transitions in ZnS. *J. Phys. Chem. Solids* **1973,** *34*, 905-909.

96.   Dong, M.; Zhang, J.; Yu, J. Effect of effective mass and spontaneous polarization on photocatalytic activity of wurtzite and zinc-blende ZnS. *APL Mater.* **2015,** *3*, 104404.

97.   Chen, Z.-G.; Zou, J.; Liu, G.; Yao, X.; Li, F.; Yuan, X.-L.; Sekiguchi, T.; Lu, G. Q.; Cheng, H.-M. Growth, Cathodoluminescence and Field Emission of ZnS Tetrapod Tree-like Heterostructures. *Adv. Funct. Mater.* **2008,** *18*, 3063-3069.

98.   Joo, J.; Na, H. B.; Yu, T.; Yu, J. H.; Kim, Y. W.; Wu, F.; Zhang, J. Z.; Hyeon, T. Generalized and facile synthesis of semiconducting metal sulfide nanocrystals. *J. Am. Chem. Soc.* **2003,** *125*, 11100-11105.

99.   Qadri, S. B.; Skelton, E. F.; Hsu, D.; Dinsmore, A. D.; Yang, J.; Gray, H. F.; Ratna, B. R. Size-induced transition-temperature reduction in nanoparticles of ZnS. *Phys. Rev. B* **1999,** *60*, 9191-9193.

Bibliography

100.   Zhao, Y.; Zhang, Y.; Zhu, H.; Hadjipanayis, G. C.; Xiao, J. Q. Low-temperature synthesis of hexagonal (Wurtzite) ZnS nanocrystals. *J. Am. Chem. Soc.* **2004,** *126*, 6874-6875.

101.   Fang, X.; Zhai, T.; Gautam, U. K.; Li, L.; Wu, L.; Bando, Y.; Golberg, D. ZnS nanostructures: From synthesis to applications. *Prog. Mater. Sci.* **2011,** *56*, 175-287.

102.   Barrelet, C. J.; Wu, Y.; Bell, D. C.; Lieber, C. M. Synthesis of CdS and ZnS nanowires using single-source molecular precursors. *Journal of the American Chemical Society* **2003,** *125*, 11498-11499.

103.   Cademartiri, L.; Ozin, G. A. Ultrathin Nanowires-A Materials Chemistry Perspective. *Adv. Mater.* **2009,** *21*, 1013-1020.

104.   Fang, H.; Bechtel, H. A.; Plis, E.; Martin, M. C.; Krishna, S.; Yablonovitch, E.; Javey, A. Quantum of optical absorption in two-dimensional semiconductors. *Proc. Natl. Acad. Sci. U. S. A.* **2013,** *110*, 11688-11691.

105.   Pässler, R.; Griebl, E.; Riepl, H.; Lautner, G.; Bauer, S.; Preis, H.; Gebhardt, W.; Buda, B.; As, D. J.; Schikora, D.; Lischka, K.; Papagelis, K.; Ves, S. Temperature dependence of exciton peak energies in ZnS, ZnSe, and ZnTe epitaxial films. *J. Appl. Phys.* **1999,** *86*, 4403-4411.

106.   Cárdenas, J. R.; Bester, G. Atomic effective pseudopotentials for semiconductors. *Phys. Rev. B* **2012,** *86*, 115332.

107.   Karpulevich, A.; Bui, H.; Antonov, D.; Han, P.; Bester, G. Nonspherical atomic effective pseudopotentials for surface passivation. *Phys. Rev. B* **2016,** *94*, 205417.

108.   Zirkelbach, F.; Prodhomme, P. Y.; Han, P.; Cherian, R.; Bester, G. Large-scale atomic effective pseudopotential program including an efficient spin-orbit coupling treatment in real space. *Phys. Rev. B* **2015,** *91*, 075119.

109.   Smith, A. M.; Mohs, A. M.; Nie, S. Tuning the optical and electronic properties of colloidal nanocrystals by lattice strain. *Nat. Nanotechnol.* **2009,** *4*, 56-63.

110.   Ong, H. C.; Chang, R. P. H. Optical constants of wurtzite ZnS thin films determined by spectroscopic ellipsometry. *Appl. Phys. Lett.* **2001,** *79*, 3612-3614.

Bibliography

111.   Yan, J.; Fang, X.; Zhang, L.; Bando, Y.; Gautam, U. K.; Dierre, B.; Sekiguchi, T.; Golberg, D. Structure and cathodoluminescence of individual ZnS/ZnO biaxial nanobelt heterostructures. *Nano Lett.* **2008,** *8*, 2794-2799.

112.   Li, J.; Wang Comparison between Quantum Confinement Effects of Quantum Wires and Dots. *Chem. Mater.* **2004,** *16*, 4012-4015.

113.   Evans, D. F.; Wennerström, H. The Colloidal Domain: Where Physics, Chemistry, Biology, And Technology Meet. *Wiley-VCH* **1999**.

114.   Messer, B.; Song, J. H.; Huang, M.; Wu, Y.; Kim, F.; Yang, P. Surfactant-Induced Mesoscopic Assemblies of Inorganic Molecular Chains. *Adv. Mater.* **2000,** *12*, 1526-1528.

115.   Liu, Y. H.; Wang, F.; Wang, Y.; Gibbons, P. C.; Buhro, W. E. Lamellar assembly of cadmium selenide nanoclusters into quantum belts. *J. Am. Chem. Soc.* **2011,** *133*, 17005-17013.

116.   Deng, Z.; Yan, H.; Liu, Y. Controlled colloidal growth of ultrathin single-crystal ZnS nanowires with a magic-size diameter. *Angew. Chem. Int. Ed.* **2010,** *49*, 8695-8698.

117.   Tran, T. K.; Park, W.; Tong, W.; Kyi, M. M.; Wagner, B. K.; Summers, C. J. Photoluminescence properties of ZnS epilayers. *J. Appl. Phys.* **1997,** *81*, 2803-2809.

118.   Baskoutas, S.; Zeng, Z.; Garoufalis, C. S.; Bester, G. Morphology control of exciton fine structure in polar and nonpolar zinc sulfide nanorods. *Sci. Rep.* **2017,** *7*, 9366.

119.   Zhang, Y.; Xu, H.; Wang, Q. Ultrathin single crystal ZnS nanowires. *Chem. Commun.* **2010,** *46*, 8941-8943.

120.   Wageh, S.; Ling, Z. S.; Xu-Rong, X. Growth and optical properties of colloidal ZnS nanoparticles. *J. Cryst. Growth* **2003,** *255*, 332-337.

121.   Peng, Z. A.; Peng, X. Formation of high-quality CdTe, CdSe, and CdS nanocrystals using CdO as precursor. *J. Am. Chem. Soc.* **2001,** *123*, 183-184.

122.   Wang, J.; Zhang, Y.; Wang, L.-W. Systematic approach for simultaneously correcting the band-gap and $p-d$ separation errors of common cation III-V or II-VI binaries in density functional theory calculations within a local density approximation. *Phys. Rev. B* **2015,** *92*, 045211.

123.   Franceschetti, A.; Fu, H.; Wang, L. W.; Zunger, A. Many-body pseudopotential theory of excitons in InP and CdSe quantum dots. *Phys. Rev. B* **1999,** *60*, 1819-1829.

124.   Chen, R.; Li, D.; Liu, B.; Peng, Z.; Gurzadyan, G. G.; Xiong, Q.; Sun, H. Optical and excitonic properties of crystalline ZnS nanowires: toward efficient ultraviolet emission at room temperature. *Nano Lett.* **2010,** *10*, 4956-4961.

125.   Bhargava, R. N.; Gallagher, D.; Hong, X.; Nurmikko, A. Optical properties of manganese-doped nanocrystals of ZnS. *Phys. Rev. Lett.* **1994,** *72*, 416-419.

126.   Begum, R.; Chattopadhyay, A. Redox-Tuned Three-Color Emission in Double (Mn and Cu) Doped Zinc Sulfide Quantum Dots. *J. Phys. Chem. Lett.* **2014,** *5*, 126-130.

127.   Pradhan, N.; Sarma, D. D. Advances in Light-Emitting Doped Semiconductor Nanocrystals. *J. Phys. Chem. Lett.* **2011,** *2*, 2818-2826.

128.   Deng, Z.; Tong, L.; Flores, M.; Lin, S.; Cheng, J. X.; Yan, H.; Liu, Y. High-quality manganese-doped zinc sulfide quantum rods with tunable dual-color and multiphoton emissions. *J. Am. Chem. Soc.* **2011,** *133*, 5389-5396.

129.   Duan, C. J.; Delsing, A. C. A.; Hintzen, H. T. Photoluminescence Properties of Novel Red-Emitting Mn^{2+}-Activated MZnOS (M = Ca, Ba) Phosphors. *Chem. Mater.* **2009,** *21*, 1010-1016.

130.   Ma, C.; Navrotsky, A. Thermodynamics of the CoO–ZnO System at Bulk and Nanoscale. *Chem. Mater.* **2012,** *24*, 2311-2315.

131.   Dai, L.; Lesyuk, R.; Karpulevich, A.; Torche, A.; Bester, G.; Klinke, C. From Wurtzite Nanoplatelets to Zinc Blende Nanorods: Simultaneous Control of Shape and Phase in Ultrathin ZnS Nanocrystals. *J. Phys. Chem. Lett.* **2019,** *10*, 3828-3835.

132.   Pradhan, N.; Das Adhikari, S.; Nag, A.; Sarma, D. D. Luminescence, Plasmonic, and Magnetic Properties of Doped Semiconductor Nanocrystals. *Angew. Chem. Int. Ed.* **2017,** *56*, 7038-7054.

133.   Yuan, X.; Ji, S.; De Siena, M. C.; Fei, L.; Zhao, Z.; Wang, Y.; Li, H.; Zhao, J.; Gamelin, D. R. Photoluminescence Temperature Dependence, Dynamics, and Quantum Efficiencies in

Mn^{2+}-Doped $CsPbCl_3$ Perovskite Nanocrystals with Varied Dopant Concentration. *Chem. Mater.* **2017,** *29*, 8003-8011.

134.   Li, Z.-J.; Hofman, E.; Davis, A. H.; Khammang, A.; Wright, J. T.; Dzikovski, B.; Meulenberg, R. W.; Zheng, W. Complete Dopant Substitution by Spinodal Decomposition in Mn-Doped Two-Dimensional $CsPbCl_3$ Nanoplatelets. *Chem. Mater.* **2018,** *30*, 6400-6409.

135.   Kumbhakar, P.; Biswas, S.; Pandey, P.; Tiwary, C. S.; Kumbhakar, P. Tailoring of structural and photoluminescence emissions by Mn and Cu co-doping in 2D nanostructures of ZnS for the visualization of latent fingerprints and generation of white light. *Nanoscale* **2019,** *11*, 2017-2026.

136.   Yang, X.; Pu, C.; Qin, H.; Liu, S.; Xu, Z.; Peng, X. Temperature- and Mn^{2+} Concentration-Dependent Emission Properties of Mn^{2+}-Doped ZnSe Nanocrystals. *J. Am. Chem. Soc.* **2019,** *141*, 2288-2298.

137.   Chen, H. Y.; Maiti, S.; Son, D. H. Doping location-dependent energy transfer dynamics in Mn-doped CdS/ZnS nanocrystals. *ACS nano* **2012,** *6*, 583-591.

138.   Mahamuni, S.; Lad, A. D.; Patole, S. Photoluminescence Properties of Manganese-Doped Zinc Selenide Quantum Dots. *J. Phys. Chem. C* **2008,** *112*, 2271-2277.

139.   Nag, A.; Sapra, S.; Nagamani, C.; Sharma, A.; Pradhan, N.; Bhat, S. V.; Sarma, D. D. A Study of Mn^{2+} Doping in CdS Nanocrystals. *Chem. Mater.* **2007,** *19*, 3252-3259.

140.   Hofman, E.; Robinson, R. J.; Li, Z. J.; Dzikovski, B.; Zheng, W. Controlled Dopant Migration in CdS/ZnS Core/Shell Quantum Dots. *J. Am. Chem. Soc.* **2017,** *139*, 8878-8885.

141.   Beermann, P. A. G.; McGarvey, B. R.; Skadtchenko, B. O.; Muralidharan, S.; Sung, R. C. W. Cationic Substitution Sites in Mn^{2+}-doped ZnS Nanoparticles. *J. Nanopart. Res.* **2006,** *8*, 235-241.

142.   Singh, A.; Geaney, H.; Laffir, F.; Ryan, K. M. Colloidal synthesis of wurtzite Cu_2ZnSnS_4 nanorods and their perpendicular assembly. *J. Am. Chem. Soc.* **2012,** *134*, 2910-2913.

143.   Selvaraj, J.; Mahesh, A.; Asokan, V.; Baskaralingam, V.; Dhayalan, A.; Paramasivam, T. Phosphine-Free, Highly Emissive, Water-Soluble Mn:ZnSe/ZnS Core–Shell Nanorods:

Bibliography

Synthesis, Characterization, and in Vitro Bioimaging of HEK293 and HeLa Cells. *ACS Appl. Nano Mater.* **2017,** *1*, 371-383.

144.   Biesinger, M. C.; Payne, B. P.; Grosvenor, A. P.; Lau, L. W. M.; Gerson, A. R.; Smart, R. S. C. Resolving surface chemical states in XPS analysis of first row transition metals, oxides and hydroxides: Cr, Mn, Fe, Co and Ni. *Appl. Surf. Sci.* **2011,** *257*, 2717-2730.

145.   Ma, Y.; Ma, Y.; Kim, G. T.; Diemant, T.; Behm, R. J.; Geiger, D.; Kaiser, U.; Varzi, A.; Passerini, S. Superior Lithium Storage Capacity of α-MnS Nanoparticles Embedded in S-Doped Carbonaceous Mesoporous Frameworks. *Adv. Energy Mater.* **2019,** *9*, 1902077.

146.   Dillip, G. R.; Banerjee, A. N.; Anitha, V. C.; Deva Prasad Raju, B.; Joo, S. W.; Min, B. K. Oxygen Vacancy-Induced Structural, Optical, and Enhanced Supercapacitive Performance of Zinc Oxide Anchored Graphitic Carbon Nanofiber Hybrid Electrodes. *ACS Appl. Mater. Interfaces* **2016,** *8*, 5025-5039.

147.   Galle, T.; Kazes, M.; Hübner, R.; Lox, J.; Samadi Khoshkhoo, M.; Sonntag, L.; Tietze, R.; Sayevich, V.; Oron, D.; Koitzsch, A.; Lesnyak, V.; Eychmüller, A. Colloidal Mercury-Doped CdSe Nanoplatelets with Dual Fluorescence. *Chem. Mater.* **2019,** *31*, 5065-5074.

148.   Lakowicz, J. R. Principles of Fluorescence Spectroscopy. *Kluwer: New York* **1999**.

149.   Ferguson, J.; J. Guggenheim, H.; Tanabe, Y. The Effects of Exchange Interactions in the Spectra of Octahedral Manganese. II. Compounds. *J. Phys. Soc. Jpn.* **1966,** *21*, 692-704.

150.   Yu, P. Y.; Cardona, M. Fundamentals of semiconductors. *Springer: New York* **1996**.

151.   Hoa, T. T. Q.; The, N. D.; McVitie, S.; Nam, N. H.; Vu, L. V.; Canh, T. D.; Long, N. N. Optical properties of Mn-doped ZnS semiconductor nanoclusters synthesized by a hydrothermal process. *Opt. Mater.* **2011,** *33*, 308-314.

152.   Zhang, W.; Li, Y.; Zhang, H.; Zhou, X.; Zhong, X. Facile synthesis of highly luminescent Mn-doped ZnS nanocrystals. *Inorg. Chem.* **2011,** *50*, 10432-10438.

153.   Dolai, S.; Nimmala, P. R.; Mandal, M.; Muhoberac, B. B.; Dria, K.; Dass, A.; Sardar, R. Isolation of Bright Blue Light-Emitting CdSe Nanocrystals with 6.5 kDa Core in Gram Scale:

High Photoluminescence Efficiency Controlled by Surface Ligand Chemistry. *Chem. Mater.* **2014,** *26*, 1278-1285.

154. Rosson, T. E.; Claiborne, S. M.; McBride, J. R.; Stratton, B. S.; Rosenthal, S. J. Bright White Light Emission from Ultrasmall Cadmium Selenide Nanocrystals. *J. Am. Chem. Soc.* **2012,** *134*, 8006-8009.

155. Grandhi, G. K.; M, A.; Viswanatha, R. Understanding the Role of Surface Capping Ligands in Passivating the Quantum Dots Using Copper Dopants as Internal Sensor. *J. Phys. Chem. C* **2016,** *120*, 19785-19795.

156. Munro, A. M.; Ginger, D. S. Photoluminescence quenching of single CdSe nanocrystals by ligand adsorption. *Nano Lett.* **2008,** *8*, 2585-2590.

157. de Mello Donega, C. Synthesis and properties of colloidal heteronanocrystals. *Chem. Soc. Rev.* **2011,** *40*, 1512-1546.

158. Xie, R.; Kolb, U.; Li, J.; Basche, T.; Mews, A. Synthesis and characterization of highly luminescent CdSe-core CdS/Zn$_{0.5}$Cd$_{0.5}$S/ZnS multishell nanocrystals. *J. Am. Chem. Soc.* **2005,** *127*, 7480-7488.

159. Hadar, I.; Philbin, J. P.; Panfil, Y. E.; Neyshtadt, S.; Lieberman, I.; Eshet, H.; Lazar, S.; Rabani, E.; Banin, U. Semiconductor Seeded Nanorods with Graded Composition Exhibiting High Quantum-Yield, High Polarization, and Minimal Blinking. *Nano Lett.* **2017,** *17*, 2524-2531.

160. Ji, B.; Panfil, Y. E.; Waiskopf, N.; Remennik, S.; Popov, I.; Banin, U. Strain-controlled shell morphology on quantum rods. *Nat. Commun.* **2019,** *10*, 2.

161. Kwon, B. H.; Lee, K. G.; Park, T. J.; Kim, H.; Lee, T. J.; Lee, S. J.; Jeon, D. Y. Continuous in situ synthesis of ZnSe/ZnS core/shell quantum dots in a microfluidic reaction system and its application for light-emitting diodes. *Small* **2012,** *8*, 3257-3262.

162. Fang, Z.; Li, Y.; Zhang, H.; Zhong, X.; Zhu, L. Facile Synthesis of Highly Luminescent UV-Blue-Emitting ZnSe/ZnS Core/Shell Nanocrystals in Aqueous Media. *J. Phys. Chem. C* **2009,** *113*, 14145-14150.

163. Dong, B.; Cao, L.; Su, G.; Liu, W. Facile synthesis of highly luminescent UV-blue emitting ZnSe/ZnS core/shell quantum dots by a two-step method. *Chem. Commun.* **2010,** *46*, 7331-7333.

164. Ji, B.; Koley, S.; Slobodkin, I.; Remennik, S.; Banin, U. ZnSe/ZnS Core/Shell Quantum Dots with Superior Optical Properties through Thermodynamic Shell Growth. *Nano Lett.* **2020,** *20*, 2387-2395.

165. Alivisatos, A. P. Perspectives on the Physical Chemistry of Semiconductor Nanocrystals. *J. Phys. Chem.* **1996,** *100*, 13226-13239.

166. Roduner, E. Size matters: why nanomaterials are different. *Chem. Soc. Rev.* **2006,** *35*, 583-592.

167. Norris, D. J.; Yao, N.; Charnock, F. T.; Kennedy, T. A. High-Quality Manganese-Doped ZnSe Nanocrystals. *Nano Lett.* **2001,** *1*, 3-7.

168. Chen, W.; Karton, A.; Hussian, T.; Javaid, S.; Wang, F.; Pang, Y.; Jia, G. Spontaneous shape and phase control of colloidal ZnSe nanocrystals by tailoring Se precursor reactivity. *CrystEngComm* **2019,** *21*, 2955-2961.

169. Bielewicz, T.; Ramin Moayed, M. M.; Lebedeva, V.; Strelow, C.; Rieckmann, A.; Klinke, C. From Dots to Stripes to Sheets: Shape Control of Lead Sulfide Nanostructures. *Chem. Mater.* **2015,** *27*, 8248-8254.

170. Hassinen, A.; Moreels, I.; De Nolf, K.; Smet, P. F.; Martins, J. C.; Hens, Z. Short-chain alcohols strip X-type ligands and quench the luminescence of PbSe and CdSe quantum dots, acetonitrile does not. *J. Am. Chem. Soc.* **2012,** *134*, 20705-20712.

171. Wijaya, H.; Darwan, D.; Lim, K. R. G.; Wang, T.; Khoo, K. H.; Tan, Z.-K. Large-Stokes-Shifted Infrared-Emitting InAs–In(Zn)P–ZnSe–ZnS Giant-Shell Quantum Dots by One-Pot Continuous-Injection Synthesis. *Chem. Mater.* **2019,** *31*, 2019-2026.

172. Liu, Y. H.; Wayman, V. L.; Gibbons, P. C.; Loomis, R. A.; Buhro, W. E. Origin of high photoluminescence efficiencies in CdSe quantum belts. *Nano Lett.* **2010,** *10*, 352-357.

173.   Park, H.; Chung, H.; Kim, W. Synthesis of ultrathin wurtzite ZnSe nanosheets. *Mater. Lett.* **2013,** *99*, 172-175.

174.   Liu, Y.; Zhang, J.; Han, B.; Wang, X.; Wang, Z.; Xue, C.; Bian, G.; Hu, D.; Zhou, R.; Li, D. S.; Wang, Z.; Ouyang, Z.; Li, M.; Wu, T. New Insights into Mn-Mn Coupling Interaction-Directed Photoluminescence Quenching Mechanism in Mn^{2+}-Doped Semiconductors. *J. Am. Chem. Soc.* **2020,** *142*, 6649-6660.

175.   Bradshaw, L. R.; May, J. W.; Dempsey, J. L.; Li, X.; Gamelin, D. R. Ferromagnetic excited-state Mn^{2+} dimers in $Zn_{1-x}Mn_xSe$ quantum dots observed by time-resolved magnetophotoluminescence. *Phys. Rev. B* **2014,** *89*.

176.   Mahler, B.; Nadal, B.; Bouet, C.; Patriarche, G.; Dubertret, B. Core/shell colloidal semiconductor nanoplatelets. *J. Am. Chem. Soc.* **2012,** *134*, 18591-18598.

177.   Tessier, M. D.; Mahler, B.; Nadal, B.; Heuclin, H.; Pedetti, S.; Dubertret, B. Spectroscopy of colloidal semiconductor core/shell nanoplatelets with high quantum yield. *Nano Lett.* **2013,** *13*, 3321-3328.

178.   Cunningham, P. D.; Coropceanu, I.; Mulloy, K.; Cho, W.; Talapin, D. V. Quantized Reaction Pathways for Solution Synthesis of Colloidal ZnSe Nanostructures: A Connection between Clusters, Nanowires, and Two-Dimensional Nanoplatelets. *ACS nano* **2020,** *14*, 3847-3857.

179.   Peng, X.; Schlamp, M. C.; Kadavanich, A. V.; Alivisatos, A. P. Epitaxial Growth of Highly Luminescent CdSe/CdS Core/Shell Nanocrystals with Photostability and Electronic Accessibility. *J. Am. Chem. Soc.* **1997,** *119*, 7019-7029.

180.   Li, Z. J.; Hofman, E.; Blaker, A.; Davis, A. H.; Dzikovski, B.; Ma, D. K.; Zheng, W. Interface Engineering of Mn-Doped ZnSe-Based Core/Shell Nanowires for Tunable Host-Dopant Coupling. *ACS nano* **2017,** *11*, 12591-12600.

181.   Diroll, B. T.; Cho, W.; Coropceanu, I.; Harvey, S. M.; Brumberg, A.; Holtgrewe, N.; Crooker, S. A.; Wasielewski, M. R.; Prakapenka, V. B.; Talapin, D. V.; Schaller, R. D. Semiconductor Nanoplatelet Excimers. *Nano Lett.* **2018,** *18*, 6948-6953.

182.   Tessier, M. D.; Biadala, L.; Bouet, C.; Ithurria, S.; Abecassis, B.; Dubertret, B. Phonon line emission revealed by self-assembly of colloidal nanoplatelets. *ACS nano* **2013,** *7*, 3332-3340.

Appendix A. Declaration of Contributions

It is challenging for one individual to perform scientific research work alone since the work usually requires interdisciplinary knowledge. Here, people who contributed to the dissertation by collecting and/or analyzing data, or providing technical assistance are listed.

Mr. Andreas Kornowski, *Mr. Stefan Werner*, *Ms. Daniela Weinert* and *Dr. Eugen Klein* (Institute of Physical Chemistry, University of Hamburg) conducted TEM measurements.

Ms. Almut Barck, *Mr. Stefan Werner*, and *Dr. Eugen Klein* (Institute of Physical Chemistry, University of Hamburg) conducted XRD measurements.

Dr. Christian Strelow (Institute of Physical Chemistry, University of Hamburg) provided assistance with TRPL measurements and data analysis.

Dr. Abderrezak Torche, *Dr. Anastasia Karpulevich*, and *Prof. Dr. Gabriel Bester* (Institute of Physical Chemistry, University of Hamburg) performed *ab initio* based calculations using atomic effective pseudopotentials.

Dr. Rostyslav Lesyuk performed Monte-Carlo calculations.

Dr. Dirk Eifler and *Ms. Iris Benkenstein* (Department of Chemistry, University of Hamburg) conducted ICP-OES measurements.

Dr. Jabor Rabeah and *Dr. Thanh Huyen Vuong* (Leibniz Institute for Catalysis) provided assistance with EPR measurements and data analysis.

Dr. James McGettrick (Materials Research Centre, Swansea University) provided assistance with XPS measurements and data analysis.

Appendix

Appendix B. List of Hazardous Substances

Table B-1. Hazard statements of the chemicals used in the presented dissertation.

Chemical	Pictogram Symbol	Hazard Statement	Precautionary Statement
Zinc (II) chloride		H302, H314, H410	P260, P280, P301 + P312 + P330, P303 + P361 + P353, P304 + P340 + P310, P305 + P351 + P338
Sulfur powder		H315	P264, P280, P302 + P352, P332 + P313, P362 + P364
Manganese (II) acetate		H373, H412	P260, P273, P314, P501
Selenium powder		H301 + H331, H373, H413	P260, P264, P273, P301 + P310, P304 + P340 + P311, P314
Octylamine		H226, H301 + H311, H314, H332, H335, H410	P210, P273, P280, P303 + P361 + P353, P304 + P340 + P310, P305 + P351 + P338
Oleylamine		H302, H304, H314, H335, H373, H410	P273, P280, P301 + P330 + P331, P303 + P361 + P353, P304 + P340 + P310, P305 + P351 + P338
Trioctylphosphine		H314	P280, P301 + P330 + P331, P303 + P361 + P353, P305 + P351 + P338
Ammonium sulfide		H226, H314, H400	P210, P233, P273, P280, P303 + P361 + P353, P305 + P351 + P338
Methanol		H225, H301 + H311 + H331, H370	P210, P233, P280, P301 + P310, P303 + P361 + P353, P304 + P340 + P311

Toluene		H225, H304, H315, H336, H361d, H373, H412	P201, P210, P273, P301 + P310, P303 + P361 + P353, P331
Isopropanol		H225, H319, H336	P210, P233, P240, P241, P242, P305 + P351 + P338
Hexane		H225, H304, H315, H336, H361f, H373, H411	P201, P210, P273, P301 + P310, P303 + P361 + P353, P331
Acetone		H225, H319, H336	P210, P233, P240, P241, P242, P305 + P351 + P338
Chloroform-d		H302,H315, H319, H331, H336, H351, H361d, H372	P201, P301 + P312, P302 + P352, P304 + P340 + P311, P305 + P351 + P338, P308 + P313
Tetramethylsilane		H224	P210
Formamide		H351, H360D, H373	P201,P202, P260, P280, P308 + P313, P405
N-methylformamide		H312, H360D	P201, P280, P302 + P352 + P312, P308 + P313
Nitric acid		H272, H290, H314, H331	P210, P220, P280, P303 + P361 + P353, P304 + P340 + P310, P305 + P351 + P338

Appendix

Table B-2. Phrases of GHS hazard statements according to Regulation (EC) No. 1272/2008.

H200	Unstable, explosive.
H201	Explosive, risk of mass explosion.
H202	Explosive; great danger from splinters and explosives.
H203	Explosive; Danger from fire, air pressure or splinters, and explosives.
H204	Danger from fire or splinters and explosives
H205	Risk of mass explosion in case of fire.
H220	Extremely flammable gas.
H221	Flammable gas.
H222	Extremely flammable aerosol.
H223	Flammable aerosol.
H224	Extremely flammable liquid and vapor.
H225	Highly flammable liquid and vapor.
H226	Flammable liquid and vapor.
H228	Flammable solid.
H229	Pressurized container: may burst if heated.
H230	May react explosively even in the absence of air.
H231	May react explosively even in the absence of air at increased pressure and/or temperature.
H240	Heating can cause an explosion.
H241	Heating can cause fire or explosion.
H242	Heating can cause fire.
H250	Self-ignites in contact with air.
H251	Self-heating, can heat itself; can catch fire.
H252	Self-heating in large quantities; can catch fire.
H260	Contact with water produces flammable gases which can ignite spontaneously.
H261	Contact with water releases flammable gases.
H270	May cause or intensify fire; Oxidizing agent.
H271	May cause fire or explosion; strong oxidizing agent.
H272	May intensify fire; Oxidizing agent.
H280	Contains gas under pressure; can explode if heated.
H281	Contains frozen gas; can cause cold burns or injuries.
H290	Can be corrosive to metals.
H300	Fatal if swallowed.
H301	Toxic if swallowed.
H302	Harmful if swallowed.
H304	Can be fatal if swallowed and enters airways.
H310	Danger to life in contact with skin.

H311	Toxic in contact with the skin.
H312	Harmful to skin contact.
H314	Causes serious irritation of the skin and serious eye damage.
H315	Causes skin irritation.
H317	May cause an allergic skin reaction.
H318	Causes serious eye damage. (not applicable if also H314)
H319	Causes serious eye irritation.
H330	Danger to life if inhaled.
H331	Toxic if inhaled.
H332	Harmful if inhaled.
H334	May cause allergy or asthma symptoms or breathing difficulties if inhaled.
H335	May cause respiratory irritation.
H336	May cause drowsiness and dizziness.
H340	May cause genetic defects (state route of exposure if it is conclusively proven that no other routes of exposure cause the hazard).
H341	Suspected of causing genetic defects (state route of exposure if it is conclusively proven that no other routes of exposure cause the hazard).
H350	May cause cancer (state route of exposure if it is conclusively proven that no other routes of exposure cause the hazard).
H351	Suspected of causing cancer (state route of exposure if it is conclusively proven that no other routes of exposure cause the hazard).
H360	May impair fertility or damage the unborn child (if known, state specific effect) (state route of exposure if it is conclusively proven that no other routes of exposure cause the hazard).
H361	Suspected of damaging fertility or the unborn child (state specific effect if known) (state route of exposure if it is conclusively proven that no other routes of exposure cause the hazard).
H362	May cause harm to babies through breast milk.
H370	Causes damage to organs (or state all organs affected, if known) (state route of exposure if it is conclusively proven that no other routes of exposure cause the hazard).
H371	May cause damage to organs (or name all organs affected, if known) (state route of exposure if it is conclusively proven that no other routes of exposure cause the hazard).
H372	Causes damage to organs (state all organs affected) through prolonged or repeated exposure (state route of exposure if it is conclusively proven that no other routes of exposure cause the hazard).
H373	May cause damage to organs (state all organs affected) through prolonged or repeated exposure (state route of exposure if it is conclusively proven that no other routes of exposure cause this hazard).
H300 + H310	Danger to life if swallowed or in contact with skin.

H300 + H330	Danger to life if swallowed or inhaled.
H310 + H330	Danger to life in case of skin contact or inhalation.
H300 + H310 + H330	Danger to life if swallowed, in contact with skin or if inhaled.
H301 + H311	Toxic if swallowed or in contact with skin.
H301 + H331	Toxic if swallowed or inhaled.
H311 + H331	Toxic if in contact with skin or if inhaled.
H301 + H311 + H331	Toxic if swallowed, in contact with skin or if inhaled.
H302 + H312	Harmful if swallowed or in contact with skin.
H302 + H332	Harmful if swallowed or inhaled.
H312 + H332	Harmful in contact with skin or if inhaled.
H302 + H312+ H332	Harmful if swallowed, in contact with skin or if inhaled.
H400	Very toxic to aquatic organisms. (not applicable if also H410)
H410	Very toxic to aquatic life with long lasting effects.
H411	Toxic to aquatic life with long lasting effects.
H412	Harmful to aquatic organisms, with long-term effect.
H413	May be harmful to aquatic organisms with long-term effects.
H420	Harms public health and the environment by depleting ozone in the external atmosphere.
H350i	May cause cancer if inhaled.
H360F	May impair fertility.
H360D	May harm the unborn child.
H361f	Suspected of damaging fertility.
H361d	Suspected of damaging the unborn child.
H360FD	May impair fertility. May harm the unborn child.
H361fd	Suspected of damaging fertility. Suspected of damaging the unborn child.
H360Fd	May impair fertility. Suspected of damaging the unborn child.
H360Df	May harm the unborn child. Suspected of damaging fertility.
EUH001	Explosive when dry.
EUH014	Reacts violently with water.
EUH018	Can form explosive / flammable vapor / air mixtures when used.
EUH019	Can form explosive peroxides.
EUH029	Develops toxic gases on contact with water.
EUH031	Develops toxic gases on contact with acids.
EUH032	Develops upon contact with acid very poisonous gases.
EUH044	Risk of explosion when heated under inclusion.
EUH066	Repeated contact can lead to rough or cracked skin.
EUH070	Toxic in contact with the eyes.
EUH071	Corrosive to the respiratory tract.
EUH201	Contains lead. Do not use for painting objects

EUH201A	that could be chewed or sucked by children. Danger! Contains lead.
EUH202	Cyanoacrylate. Danger. Bonds skin and eyelids in seconds. Keep out of the reach of children.
EUH203	Contains chromium (VI). Can cause allergic reactions.
EUH204	Contains isocyanates. Can cause allergic reactions.
EUH205	Contains compounds containing epoxy. Can cause allergic reactions.
EUH206	Danger! Do not use together with other products as dangerous gases (chlorine) can be released.
EUH207	Danger! Contains cadmium. Hazardous fumes are generated during use. Follow the manufacturer's instructions. Comply with safety instructions.
EUH208	Contains (name of the sensitizing substance). Can cause allergic reactions. (EUH08 can be omitted if EUH204 or EUH 205 is required.)
EUH209	Can become highly flammable in use.
EUH209A	Can become flammable in use.
EUH210	Safety data sheet available on request.
EUH401	To avoid risks to people and the environment, follow the instructions for use.

Appendix

Table B-3. Phrases of GHS Precautionary statements according to Regulation (EC) No. 1272/2008.

P101	If medical advice is needed, have container or label ready.
P102	Keep out of the reach of children.
P103	Read label before use.
P201	Obtain special instructions before use.
P202	Read and understand all safety advice before use.
P210	Keep away from heat, hot surfaces, sparks, open flames and other ignition sources. Do not smoke.
P211	Do not spray on an open flame or other ignition source.
P220	Keep away from clothing and other combustible materials.
P222	Avoid contact with air.
P223	Do not allow any contact with water.
P230	Keep wet with ....
P231	Handle and store contents under inert gas /…
P232	Protect from moisture.
P233	Keep container tightly closed.
P234	Store only in the original packaging.
P235	Keep cool.
P240	Earth the container and the system to be filled.
P241	Use explosion-proof [electrical / ventilation / lighting /…] devices.
P242	Use low-spark tools
P243	Take measures against electrostatic discharges.
P244	Keep valves and accessories free of oil and grease.
P250	Do not grind / bump / rub /….
P251	Do not pierce or burn, even after use.
P260	Do not breathe dust / smoke / gas / mist / vapor / aerosol.
P261	Avoid inhalation of dust / smoke / gas / mist / vapor / aerosol.
P262	Do not get in eyes, on skin, or on clothing.
P263	Avoid contact during pregnancy and breastfeeding.
P264	Wash thoroughly after handling.
P270	Do not eat, drink or smoke when using.
P271	Use only outdoors or in a well-ventilated area.
P272	Do not wear contaminated work clothing outside of the workplace.
P273	Avoid release to the environment.
P280	Wear protective gloves / protective clothing / eye protection / face protection.
P282	Wear protective gloves with cold insulation / face shield / eye protection.

Appendix

P283	Wear flame retardant or flame retardant clothing.
P284	[In case of insufficient ventilation] wear respiratory protection.
P231 + P232	Handle and store contents under inert gas /…. Protect from moisture.
P301	IF SWALLOWED:
P302	IF ON SKIN:
P303	IF ON SKIN (or hair):
P304	IF INHALED:
P305	IF IN CONTACT WITH THE EYES:
P306	IN CASE OF CONTACT WITH CLOTHING:
P308	IF exposed or concerned:
P310	Call a POISON CENTER / doctor / ... immediately.
P311	Call a POISON CENTER / doctor /….
P312	Call a POISON CENTER / doctor /… if you feel unwell.
P313	Get medical advice / assistance.
P314	Get medical advice / assistance if you feel unwell.
P315	Get medical advice / assistance immediately.
P320	Special treatment is urgently required (see ... on this label).
P321	Special treatment (see ... on this label).
P330	Rinse out mouth.
P331	DO NOT induce vomiting.
P332	In case of skin irritation:
P333	If skin irritation or rash occurs:
P334	Soak in cold water [or put on a wet bandage].
P335	Brush off loose particles from the skin.
P336	Thaw icy areas with lukewarm water. Do not rub the affected area.
P337	If eye irritation persists:
P338	Remove any existing contact lenses if possible. Continue rinsing.
P340	Move the affected person into fresh air and make sure they can breathe freely.
P342	If there are symptoms of the respiratory tract:
P351	Rinse gently with water for a few minutes.
P352	Wash with plenty of water /….
P353	Wash skin [or shower] with water.
P360	Wash contaminated clothing and skin immediately with plenty of water and then take off clothing.
P361	Take off immediately all contaminated clothing.
P362	Take off contaminated clothing.
P363	Wash contaminated clothing before reuse.
P364	And wash before wearing again.
P370	In case of fire:

P371	In the event of a major fire and large quantities:
P372	Risk of explosion.
P373	DO NOT fight fire if fire reaches explosive substances / mixtures / or products.
P375	Fight fire remotely due to the risk of explosion.
P376	Stop leak if without risk.
P377	Leaking gas fire: Do not extinguish until leak can be stopped safely.
P378	... use to delete.
P380	Clear the environment.
P381	In the event of a leak, remove all sources of ignition.
P390	Absorb leaked quantities to avoid material damage.
P391	Catch spilled quantities.
P301 + P310	IF SWALLOWED: Immediately call a POISON CENTER / doctor /….
P301 + P312	IF SWALLOWED: Call a POISON CENTER / doctor /… if you feel unwell.
P301 + P330 + P331	IF SWALLOWED: rinse mouth. DO NOT induce vomiting.
P302 + P334	IF ON SKIN: Immerse in cold water or wrap in wet bandages.
P302 + P335 + P334	IF ON SKIN: Brush off loose particles from skin. Soak in cold water [or put on a wet bandage].
P302 + P352	IF ON SKIN: Wash with plenty of water /….
P303 + P361 + P353	IF ON SKIN (or hair): Take off immediately all contaminated clothing. Wash skin [or shower] with water.
P304 + P340	IF INHALED: Remove the person to fresh air and ensure that they can breathe freely.
P305 + P351 + P338	IF IN EYES: Rinse cautiously with water for several minutes. Remove any existing contact lenses if possible. Continue rinsing.
P306 + P360	IF ON CLOTHING: Wash contaminated clothing and skin immediately with plenty of water and then take off clothing.
P308 + P311	IF exposed or concerned: Call a POISON CENTER / doctor /….
P308 + P313	IF exposed or concerned: Get medical advice / attention.
P332 + P313	If skin irritation occurs: Get medical advice, get medical attention.
P333 + P313	If skin irritation or rash occurs: Get medical advice / attention.
P336 + P315	Thaw icy areas with lukewarm water. Do not rub the affected area. Get medical advice / assistance immediately.
P337 + P313	If eye irritation persists: Get medical advice / assistance.
P342 + P311	If you experience symptoms of the respiratory tract: Call a POISON CENTER / doctor /….
P361 + P364	Immediately take off all contaminated clothing and wash it before reuse.
P362 + P364	Take off contaminated clothing and wash it before reuse.
P370 + P376	In case of fire: Stop leak if without risk.

P370 + P378	In case of fire: Use ... to extinguish.
P370 + P372 + P380 + P373	In case of fire: risk of explosion. Clear the environment. DO NOT fight fire if fire reaches explosives.
P370 + P380 + P375	In case of fire: evacuate the area. Fight fire from a distance due to the risk of explosion.
P370 + P380 + P375 [+ P378]	In case of fire: evacuate the area. Fight fire remotely due to the risk of explosion. [... use to extinguish.] (Note: Specify in [...] if water is not suitable as an extinguishing agent)
P371 + P380 + P375	In the event of a major fire and large quantities: Evacuate the area. Fight fire remotely due to the risk of explosion.
P401	Store in accordance with….
P402	Store in a dry place.
P403	Keep in a well-ventilated place.
P404	Store in a closed container.
P405	Store locked up.
P406	Store in a corrosion-resistant / ... container with a corrosion-resistant inner liner.
P407	Leave air gap between stacks or pallets.
P410	Protect from direct sunlight.
P411	Keep at temperatures not exceeding… ° C /… ° F.
P412	Do not expose to temperatures exceeding 50 ° C / 122 ° F.
P413	Store bulk goods in quantities of more than… kg /… lbs at temperatures not exceeding… ° C /… ° F.
P420	Store separately.
P402 + P404	Store in a dry place. Store in a closed container.
P403 + P233	Keep in a well-ventilated place. Keep container tightly closed.
P403 + P235	Keep in a well-ventilated place. Keep cool.
P410 + P403	Protect from direct sunlight. Keep in a well-ventilated place.
P410 + P412	Protect from direct sunlight. Do not expose to temperatures exceeding 50 ° C / 122 ° F.
P501	Dispose of contents / container to.
P502	Contact the manufacturer or supplier for information on reuse or recycling.

Publications

1. From Wurtzite Nanoplatelets to Zinc Blende Nanorods: Simultaneous Control of Shape and Phase in Ultrathin ZnS Nanocrystals
Liwei Dai, Rostyslav Lesyuk, Anastasia Karpulevich, Abderrezak Torche, Gabriel Bester, and Christian Klinke*. *J. Phys. Chem. Lett.* **2019**, *10*, 3828−3835.

2. Colloidal Manganese-Doped ZnS Nanoplatelets and Their Optical Properties
Liwei Dai, Christian Strelow, Tobias Kipp, Alf Mews*, Iris Benkenstein, Dirk Eifler, Thanh Huyen Vuong, Jabor Rabeah, James McGettrick, Rostyslav Lesyuk, and Christian Klinke*. *Chem. Mater.* **2021**, *33*, 1, 275–284.

3. Coupling and Photoluminescence Kinetics in Mn^{2+}-doped ZnS Nanoplatelets
Liwei Dai, Abderrezak Torche, Thanh Huyen Vuong, Christian Strelow, Tobias Kipp, Gabriel Bester, Alf Mews, Christian Klinke, Rostyslav Lesyuk*. In progress.

4. Synthesis of Colloidal Mn^{2+}-doped ZnSe/ZnS Core/Shell Nanoplatelets for Tunable Photoluminescence. In progress.

Declaration: This dissertation essentially composes of the supplementary scientific work which has been published with first authorship by the author of this dissertation, Liwei Dai in the journals: Journal of Physical Chemistry Letters and Chemistry of Materials.

Conference Contributions

1. **PIER PhD Seminar 2019**

   April 22, 2019 in Hamburg, Germany

   Colloidal Synthesis and Characterization of Quasi-Two-Dimensional ZnS Nanoplatelets (oral)

2. **Visit to Denmark**

   September 2−5, 2019 in Aabenraa, Denmark

   Synthesis and Applications of Colloidal Two-Dimensional Metal Chalcogenides (oral)

3. **Nanoscience with Nanocrystals 9 (NaNaX 9)**

   September 16−20, 2019 in Hamburg, Germany

   Shape/Phase Control in Ultrathin ZnS Nanocrystals (poster)

4. **NanoPlus 2020**

   April 30, 2020 online

Declaration

According to § 7 (4) of the doctoral degree regulations from the Faculty of Mathematics, Informatics and Natural Sciences (MIN) of the University of Hamburg:

I hereby declare on oath, that I have written the present dissertation on my own and have not used other than the acknowledged resources and aids. The submitted written version corresponds to the version that is shown on the electronic storage medium. I here declare that I have not previously applied or pursued for a doctorate (Ph.D. study).

Liwei Dai

Date: 27/09/2021   Signature: Liwei Dai